

# Crystalline Order in Compound Semiconductors in Nanoscale Structures and Thin Films

Présentée le 22 juin 2021

Faculté des sciences et techniques de l'ingénieur  
Laboratoire des matériaux semiconducteurs  
Programme doctoral en science et génie des matériaux

pour l'obtention du grade de Docteur ès Sciences

par

**Mahdi ZAMANI**

Acceptée sur proposition du jury

Prof. P. Hoffmann, président du jury  
Prof. A. Fontcuberta i Morral, directrice de thèse  
Dr N. Gogneau, rapporteuse  
Prof. J. Puigdollers Gonzalez, rapporteur  
Dr F.-J. Haug, rapporteur

**Dedicated to the victims of the Islamic Republic of Iran since 1979**



# Acknowledgement

I've been thinking about writing this section, the last part of my thesis to be written, for a few days now and have not been able to yet come up with something that "feels right". Nothing seems to do the people involved justice, so, I decided to just let go and write my thoughts in their pure, unprocessed form.

Working in LMSC for more than 5 years (for my Ph.D thesis and the internship I did before that) has shaped my personality in a profound way. I can see clear signs of personal development because of my work in LMSC. This was only possible because of the continuous support, trust and mentorship of Prof. Anna Fontcuberta i Morral. I honestly did not expect this level of care from my supervisor and cannot thank her enough for the great experience I had in her group. In addition to her scientific excellence, I was always surprised by the level of care she had for the personal well-being of her students. Furthermore, she would always provide great feedback that helped me understand my shortcoming. Simply put, she helped me grow not only as a scientist, but also as a person.

My life in LMSC started in October 2015 under the co-supervision of Gozde. In hindsight, I couldn't have been luckier: she has amazing field knowledge and hands on experience with the everything I needed. I was surprised and honored for the level of trust she put in me during my internship and am so glad to have her as a close friend after these years. She is an exceptional scientist and an amazing human being and am sure that she will be an great professor at Wayne State University.

When I arrived at LMSC, there was an older generation of Ph.D students including Luca Francaviglia, Heidi Potts, Jelena Vukajlovic-Plestina, Martin Friedl, Francesca Amaduzzi, Elenora Frau and Dmitry Mikulik working there, who all helped make my experience exceptionally pleasant. I really appreciate the effort Luca put to incorporate me to the atmosphere and the culture of the group and make my early weeks less awkward. In addition, he was a continuous source of education on different spectroscopy methods and trained me on cathodoluminescence. Heidi and Jelena were those who, despite not being my official supervisors, taught me a lot about working with MBE, which initially looked like an intimidating monster to me. In addition, they were kind enough to listen to my countless questions and have discussions about crystal growth. Martin is outright one of the most hard-working people I've ever known and it was a privilege sharing a desk with him for 4 years. At time, I would be surprised by the number of different projects he was running, some of which had great communal benefits for everyone in the group. He would be willing to help anyone in need, and I personally benefited a lot from his knowledge during my years at LMSC. Elenora, Francesca and Dimitry, while not working with me directly, all helped establish the very friendly experience I had.

Then came the newer generation of colleagues gradually. This includes Lea Ghisalberty, Edoardo Markov, Wonjong Kim, Lucas Güniat, Andreana Danill, Simon Escobar Steinvall, Elias Stutz, Rajrupa Paul, Pablo Romero Gomez, Nicolas Tappy, Anna Kúkol'ová, Didem Dede, Akshay Balgarkashi, Andrea Giunto, Nicholas Morgan and Mirjana Dimitrievska. I remember the special group I, Lea and Edoardo had as we were all supervised by Gozde and all the cooking/ drinking activities we had together. Wonjong and Lucas both were amazing colleagues and friends to work with. On top of their amazing collaborative spirit and willingness to help, they were just great to be around, and hanging out with them would be an uplifting experience. Simon, Elias and Rajrupa all provided major help for my thesis, and I would not have been able to finish my project without their help and. In particular, Simon was the person who, beside Jean-Baptiste, trained me on one of the MBE machines I used during my PhD. Nicolas Tappy (often called Nico and not to be mixed with Nicholas Morgan) is one of the smartest persons I've ever met and I was often surprised and amazed by his deep knowledge of physics. I



remember how the ideas I got from a casual conversation with him led to the solution of one of the hardest things I have worked on during my Ph.D. In addition, he and his pet might be the reason for my increased interest in dogs now. Anna, Didem and Nicholas Morgan (often called Nick and not to be mixed with Nicolas Tappy) were great people to be around with their positivity and humor. It was nice to share office with Nico, who, like myself, was very much interested in politics and made me have my share of political discussion at work. Andrea and Akshay, who I could always count on for some serious and deep scientific discussion, also proved to be amazing and caring colleagues. Andreana and Pablo were also sources of great humor. Finally, Mirja, who joined us as scientist towards the end of my Ph.D, was also extremely knowledgeable and kind, and we had extremely fruitful interaction during the relatively short overlap we had at LMSC.

I cannot talk about my LMSC years without thanking Monika Salas Tesar, Laura Beth Bischoff-Dukes and Jean-Baptiste Leran. Monika and Laura provided reliable support as secretaries of the lab. Jean-Baptiste played an extremely important role in my Ph.D thesis as he was the person responsible for the operations of the two MBE machines I used. Essentially, it would have been impossible for me and other LMSC students in the recent years to finish their thesis without his help.

Looking back at these last few years, the various social activities we did together were essential part of my LMSC experience. Between the parties Martin would have at his place, board game/ video game/ CS matches, the hikes or birthday celebrations we had together, I could not have asked for a better group of colleagues.

A very attractive aspect of my Ph.D thesis has been its collaborative nature, which was not limited to my colleagues at LMSC. I was privileged to work with amazing external scientist for various aspects of my work. These include Giulio Imbalzano, Sebastien Bienvenue and Prof. Michele Ceriotti from EPFL COSMO, Dr Duncan T.L Alexander from EPFL LSME/ CIME, Prof Jordi Arbiol from ICN2, Prof. Quentin M. Ramasse from SuperSTEM facility, Dr Reza. R. Zamani from EPFL CIME, Dr Djamshid Damry and Prof. Jessica Boland from The University of Manchester. In particular, I need to thank Giulio, who is responsible for the simulations that were essential to my research. We certainly did not expect the scope of our collaboration to get so big at the beginning, but I'm proud that our work and numerous meeting paid off at the end. In addition, I need to specially mention Dr Duncan Alexander, who, like Giulio, was the subject to my many questions and meeting requests. Furthermore, if not for the technical support of EPFL staff, at CIME and CMi, my daily experimental operations might have not been possible.

Finishing I would need to thank my jury members, Dr Franz-Josef Haug, Dr Gogneau Noelle, Prof. Puigdollers Gonzalez Joaquin and Prof. Patrik Hoffmann, for their effort and feedback, which helped improve the quality of this thesis a lot.

Finally, I would have not been able to do any of this if not for my parents and family. I cannot thank my parents enough for their support and sacrifices during my life and am simply proud of them. My siblings, Morteza, Mahboubah and Majid, too, have been a constant source of pride and joy in my life. Mahdi Zamani, Chavannes-près-Renens, 12 May 2021

## Abstract

Semiconductors materials and devices are essential building blocks for many of the technologies deeply embedded in modern life. Improving the performance of semiconductor devices requires a deeper understanding of the fundamental mechanisms controlling the crystalline structure of the semiconductor materials. This thesis focuses on two compound semiconductor systems in the form of  $Zn_3P_2$  thin films and  $GaAs$  nanowires and tries to establish methods for minimizing the defects in these structures by the careful control of order at the atomic scale.

In the first part of this work, we have focused on  $Zn_3P_2$  thin films. The combination of suitable material properties and the abundancy of its constituting elements makes this platform a promising candidate for large-scale and scalable photovoltaic applications. Despite this,  $Zn_3P_2$  is not adopted by the solar industry due to the many technical challenges in the growth of this material. In this work, by careful control of the state of the interface between the thin films and the substrates, we have provided a method for the growth of thick and monocrystalline  $Zn_3P_2$  thin films with superior quality. This is crucial for the realization of any successful photovoltaic cell based on this material. Although molecular beam epitaxy is used in this study, the process provided is generalizable and could also be exploited for the other growth methods. A host of different characterization techniques, including electron microscopy and spectroscopy, Raman spectroscopy, photoluminescence spectroscopy and x-ray diffraction are used to assess the different aspects of the thin films. It is observed that monocrystalline films have better optical properties compared to polycrystalline thin films, making them more suitable for photovoltaic applications.

In the second part of the thesis, we have focused on improving the crystalline quality of  $GaAs$  nanowires. Similar to other III-V semiconductors,  $GaAs$  hosts an internal electrical dipole known as polarity. Arsenide and phosphide nanowires often grow along  $(111)B$  direction, which implies the termination of  $(111)$  bilayer by group V elements. However, this configuration is often defective and results in polytypism. On the other hand,  $(111)A$  growth, which refers to group III termination, results in a crystalline structure that is largely free of defects. However, growth in this polarity is rarely reported. In this work, we try to understand the reason for this elusiveness and the superior crystalline quality associated with A-polar growth. To do that, we have established a new framework that explicitly focuses on the atomic structure and order of liquid-solid interface in nanowires grown by vapor-liquid-solid method. The atomic structure of this interface has been ignored up to now in the literature due to the technical challenges for investigating such fragile atomic order. Here, we employ a combination of experimental observations via electron microscopy and spectroscopy and machine-learning based molecular dynamics simulations that were developed by external collaborators. The results of this study provide a unique insight into the fundamental aspects of nanowire growth.

Key words: compound semiconductors, photovoltaic cells, molecular beam epitaxy, thin films, nanowires, growth polarity, liquid- solid interface, liquid ordering

## Table of Contents

<b>1: Introduction.....</b>	<b>1</b>
1.1 Motivation .....	1
1.2 <b>Zn3P2</b> Thin Films.....	1
1.2.1 Review of Earth-Abundant Semiconductors .....	1
1.2.2 <b>Zn3P2</b> .....	5
1.3 GaAs Nanowires.....	10
1.3.1 Motivation for studying the growth of GaAs Nanowires.....	10
1.3.2 Properties of GaAs Nanowires.....	11
1.3.3 Methods for the Growth of Semiconductor Nanowires .....	13
1.4 Thesis Outline.....	15
<b>2: Methods .....</b>	<b>17</b>
2.1 Molecular Beam Epitaxy for Growth of <b>Zn3P2</b> .....	17
2.1.1 Structure and Working Principles .....	17
2.2 Characterization Techniques .....	22
2.2.1 Electron Microscopy and Electron Spectroscopy .....	22
2.2.2 Focused Ion Beam (FIB).....	31
2.2.3 Raman Spectroscopy .....	33
2.2.4 XRD .....	36
<b>3: Results &amp; Discussion.....</b>	<b>38</b>
3.1 Growth optimization of <b>Zn3P2</b> thin films on <b>InP 001</b> substrate .....	38
3.2 Liquid ordering at the interface of crystalline <b>GaAs</b> and liquid <b>Ga</b> .....	51
<b>Conclusion and Outlook .....</b>	<b>61</b>
<b>Appendix A: Supporting information .....</b>	<b>65</b>
<b>Appendix B: Unpublished Experimental Results.....</b>	<b>83</b>
<b>Publication List .....</b>	<b>85</b>
<b>Bibliography .....</b>	<b>87</b>
<b>Curriculum Vitae .....</b>	<b>101</b>

# List of Figures

Figure 1-1. (a) Relative abundancy of different elements compared to <i>Si</i> in earth's crust. (b) Annual electricity production potential for 23 inorganic semiconductors.	3
Figure 1-2. (a): the phase diagram of <i>Zn – P</i> system. (b): The unit cell of <i>Zn<sub>3</sub>P<sub>2</sub></i> , showing the position of <i>Zn</i> and <i>P</i> atoms in addition to the vacant sites..	7
Figure 1-3: Bright field transmission electron micrographs of pseudomorphic <i>Zn<sub>3</sub>P<sub>2</sub></i> layers.	9
Figure 1-4. Van der Pauw resistivity, hole carrier concentration, and hole mobility as a function of <i>Zn<sub>3</sub>P<sub>2</sub></i> epilayer thickness..	10
Figure 1-5. Stacking and unit cells of zinc blende and wurtzite <i>GaAs</i> Unit cells.	12
Figure 1-6. Polytypism and defects in <i>GaAs</i> NWs.	13
Figure 1-7. Growth of <i>GaAs</i> NWs on a <i>GaAs</i> substrate..	14
Figure 2-1. Veeco GENxplore and its components.	18
Figure 2-2. a schematic view of the Veeco GENxplore MBE growth chamber showing the cells, cryopanel, RHEED gun and screen, BFM and QCM.	19
Figure 2-3. A schematic view of how RHEED patterns are formed.	20
Figure 2-4. Different surface configurations and their corresponding reciprocal space and RHEED patterns. These images are taken from reference (155).	20
Figure 2-5. An schematic view of DCA P600 dual chamber system.	22
Figure 2-6. Different physical electron-matter interaction mechanisms used in electron microscopy and spectroscopy.	23

Figure 2-7. A view of electron scattering by a single atom (carbon)..	24
Figure 2-8: schematic view of different electron microscopy configurations.	27
Figure 2-9. Comparison of bright field and dark field electron microscopy imaging	28
Figure 2-10. Different types of aberrations in lenses.	29
Figure 2-11. The trend for minimum resolving power of microscopes in Å for different years since mid-18 century.	30
Figure 2-12. Focus ion beam process for making a TEM lamella.	33
Figure 2-13. The comparison of Raman spectra for amorphous and polycrystalline Zn <sub>3</sub> P <sub>2</sub> thin films measured with identical parameters.	35
Figure 2-14. Schematic view of basic structure of a Raman setup.	35
Figure 2-15. Schematic view of GIXRD and Gonio XRD scans.	36
Figure 2-16. The comparison of the XRD pattern of a polycrystalline and a monocrystalline thin film.	37
Figure B 1. The PL spectra of three samples with different stoichiometries measured at 12K with the 488 laser and the laser power of 9 mW.	83
Figure B 2. The change in the intensity of Raman peaks for three monocrystalline thin films with different stoichiometries.	84

## List of Tables

Table 1-1. Abundance, extraction and potential for power production for some critical thin film PV elements compared to Si. ....2

Table 2-1: the demonstration of relativistic effects on the speed and the mass of electrons.....31

Table B 1 : the degassing time and composition of the three samples studied by PL.....83





# 1: Introduction

## 1.1 Motivation

Semiconductor technologies have been an essential pillar of human life in the last few decades. Telecommunication, internet, personal computers, mobile phones, internet-of-things and e-commerce are a few aspects of modern life enabled by semiconductor industry. In addition, transformative technologies that are expected to play a vital role in the upcoming years such as artificial intelligence, 5G and photovoltaics (PV) use semiconductors as their foundation. The continuous improvement of the performance of semiconductor devices is, therefore, a goal for governments, private companies and researchers alike.

A determining factor in the performance of semiconductor devices is the quality of materials (1,2). Dedicated techniques have been developed to study the effects of defects on the functional properties of semiconductors (3) and control/ elimination of defects is one of the fundamental requirements for optoelectronic applications (4–6). While silicon wafers are now essentially defect free due to the invention and development of energy-intensive processes such as Czochralski and float zone (7,8), manufacturing defect-free compound semiconductors has proven to be generally more challenging and costly. Elimination of defects was one of the main steps that resulted in development of gallium nitride (GaN) blue light-emitting diodes, which ultimately was rewarded by Physics Nobel Prize in 2014 (9,10). Owing to the dissimilar nature of their constituting elements, compound semiconductors are inherently prone to having defects. In addition, compound semiconductors are often epitaxially grown on substrates made of other materials to create the functionality in the form of quantum wells, dots and or junctions. Defects can be originated from this substrate and propagated to the semiconductors (11–13). This thesis tries to tackle the scientific questions of limiting structural and electronically active defects in two compound semiconductor systems, zinc phosphide ( $Zn_3P_2$ ) thin films and gallium arsenide ( $GaAs$ ) nanowires. These two material systems have been proposed as potential platforms for next-generation PV. This thesis focuses on fundamental aspects of epitaxy that should enable the utilization of these materials in the future for these applications.

## 1.2 $Zn_3P_2$ Thin Films

### 1.2.1 Review of Earth-Abundant Semiconductors

Large-scale deployment of PV energy is widely considered as one of the key solutions to fight reduce climate change as they offer a path to reduce dependency on fossil fuels (14). Si-based solar cells, which dominate the global market as of now (15), have relatively high energy payback times (EPBT) due to the very high energy demand for production of silicon wafers (16).

The main category of rival technologies to bulk silicon-based PV modules are thin film technologies. Thin film based solar cells are made of direct band gap semi-conductor materials. This essentially means that the absorbing layer of the modules can be much thinner than the silicon-based counterparts. The most widespread thin-film technologies are *CdTe* and Copper Indium Gallium Selenide (*CIGS*) cells. Despite the promise of thin-film technologies for lower EPBT and electricity price, they have shown a limited market penetration. For *CdTe* technology, the presence of *Cd* has not been welcomed due to its toxicity<sup>1</sup> For both of these technologies, too, there is a serious limitation for scaling up due to the scarcity of the elements used. In, Se, Ga and Te are all relatively scarce elements. Figure 1-1 (a) demonstrates the number of atoms of different elements per 10<sup>6</sup> atoms of Si in earth crust. In 2012, the total production of silicon had been 7.8 million tons, while the gallium production has been just 380 tons (17). Unlike some other aspects of PV power generation, employing scarce materials will not benefit from economies of scale. Table 1-1, taken from (17) further highlights the resource scarcity for current thin film PV technologies. In addition to limited resources, it is worth mentioning that 52% of indium production is carried out in China (18), imposing major risk on the international supply stability of this element. Furthermore, one must consider that 80% of the produced indium is used for flat panel displays (19), and the demand for these screens is increasing with no sight of reduction in the foreseeing future.

Table 1-1. Abundance, extraction and potential for power production for some critical thin film PV elements compared to Si. This table is taken from (17) with permission © MIT.

	Si	Te	Ga	In	Se
Abundance [fraction]	0.28	$1.0 \times 10^{-9}$	$1.9 \times 10^{-5}$	$2.5 \times 10^{-7}$	$5.0 \times 10^{-8}$
Culminative production (1900-2012)[10 <sup>6</sup> tons]	160	0.010	0.0026	0.010	0.091
Culminative amount in PV by 2050 for 100% PV operation [10 <sup>6</sup> tons]	51	0.79	0.11	0.19	0.51
Ration of 2050 PV culminative production to culminative 1900-2012 production	0.32	76	43	18	5.6

<sup>1</sup> It is to be noted that using *Cd* in electrical and electronic equipment is banned in the European Union. However, photovoltaic cells are exempted from this rule (183).

These shortcomings of thin film PV technologies have prompted the scientific community to investigate the possibility of adopting new category of semiconductors, denominated as earth abundant semiconductors. As the name implies, these semiconductors are composed of elements that are not scarce, and thus they are more appropriate for scaling up. Copper based  $I_2 - II - IV - VI_4$  quaternary kesterite compounds, including  $Cu_2ZnSnS_4$  (CZTS) and  $Cu_2ZnSnSe_4$  (CZTSe) have gained interest in research community as a potential alternative for CIGS and CdTe technologies. The region of phase stability for CZTS(Se) is narrower than CIGS, making the growth of good quality absorber phase even more challenging (20). These compounds provide tunable bandgap of 1.0-1.5eV, with optical absorptions coefficients higher than  $10^4 \text{ cm}^{-1}$  (21,22). CZTS is a p-type semiconductor. Shockley-Queisser limit for CZTS(Se) is around 32.2% (23). The efficiency of CZTS devices has increased from 0.66% in 1997 to current record value of 13.8% on small- area cells (24). Still, the improvement of performance of CZTS(Se) PV systems cells have been very slow post- 2010 (25) and the efficiency have been stagnant. This stems from some inherent challenges that CZTS(Se) exhibits. For instance, the main defect in this material is  $Cu_{Zn}$ , which has a very negative formation energy and forms spontaneously (26). The very close atomic radii of Zn and Cu at 142 pm and 145 pm, respectively, are speculated as the reason for this low defect formation energy (27). It is unlikely that these defects will be ever eliminated completely from CZTS(Se) as these radii values are inherent properties of constituting elements in CZTS(Se) system.

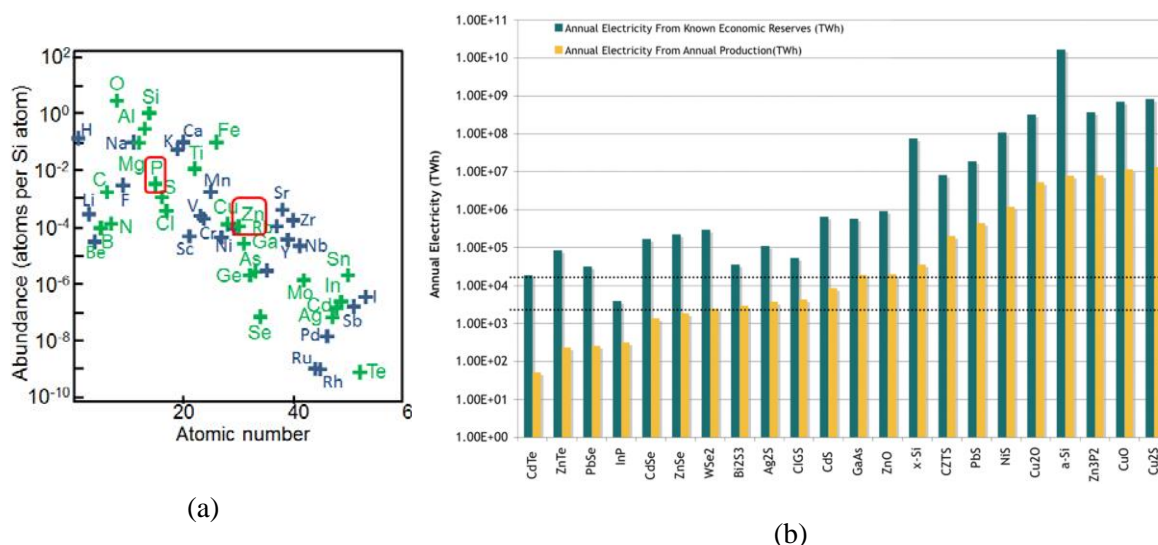


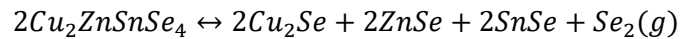
Figure 1-1. (a) Relative abundancy of different elements compared to *Si* in earth's crust. (b) Annual electricity production potential for 23 inorganic semiconductors. The data for known economic reserves and annual production are taken from the U.S. Geological Survey studies (28). Total U.S. and worldwide annual electricity consumption are labeled on the figure for comparison by the dotted horizontal lines. Figure 1-1(b) and its caption are adjusted from reference (29) with permission © ACS.

It has been suggested that formation of band-edge tail states is a fundamental performance bottleneck for hydrazine processed CZTS(Se) cells. This effect is shown to be twice as severe as high-performing CIGS devices (24). Deep defect energy acceptor  $Cu_{Zn}$  and donor  $Zn_{Cu}$  together with high density of interface defects are also identified as contributing factors to limited efficiency of CZTS cells (30).

The growth of high-quality CZTSe thin has proven challenging. For instance, the range of Se pressures in which CZTSe is stable is many order of magnitude lower than the range for  $CuInSe_2$

due to the relative weakness of Sn – S(Se) bonds (31). This lower stability range is thus also an inherent feature of *CZTSe*, and makes the growth of good quality *CZTS(Se)* films to be extremely difficult task with vacuum based methods. This is exacerbated by the difference in the reactivity of *Cu*, *Zn* and *Sn* towards chalcogens. In addition, lower thermal stability of Sn – S(Se) bonds can lead to reaction with *Mo* that is often used as back contact for these types of cells. Indeed, the stable thermodynamic products in *Cu – Zn – Sn – Mo – S* system are  $Cu_2S + ZnS + SnS + MoS_2$  rather than *CZTS + Mo* (32,33).

The weakness of Sn – S(Se) bonds can be traced back in the oxidation states of *Sn*. In *CZTS(Se)*, *Sn* is in oxidation state of +IV, which can be easily converted to +II oxidation state. This reduction in oxidation state results in the disruption of kesterite structure through this reaction:



Apart from thermodynamic stability issue for *CZTS(Se)*, growth of pure, defect-free films of this material is difficult due to the very different nature of *Cu*, *Zn* and *Sn*, as they will have different reactivity towards chalcogens (34).

The aforementioned difficulties in growth of high-quality *CZTS(Se)* have made researchers interested to other earth-abundant semiconductors. In search for new semiconductors for photovoltaic applications, the important parameters to consider for absorber are bandgap value and type, absorption coefficient above the bandgap, net acceptor doping density, minority carrier life time, conductivity and mobility (33). In the next few paragraphs, we try to review some of these alternative materials.

Pyrite,  $FeS_2$  has been proposed and studied as a cheap alternative for current thin film photovoltaic materials. A study in 2009 found that, neglecting the technical challenges of making working photovoltaic devices and considering the theoretical limits, pyrite is the most attractive earth-abundant semiconductor for solar cell applications given its abundance and extremely low price (29). It has the direct bandgap value of 0.95 eV and absorption coefficient values higher than  $5 \times 10^5 \text{ cm}^{-1}$  (35). The promising nature of this material has however not materialized in high efficiencies. One of the reasons is the high rate of carrier recombination at the surfaces and interfaces. This has been elucidated by photoelectron studies that have shown that the surface Fermi level is 100 meV from valance band edge, indicating a strong surface band bending due to a high density of surface states. Passivation attempts have so far not been conclusive (35). Thin films of pyrite are reported to be p-type, show conductance of  $1 \Omega^{-1} \text{ cm}^{-1}$ , carrier concentrations of between  $10^{18} \text{ cm}^{-3}$  and  $10^{23} \text{ cm}^{-3}$  and low mobility values of  $< 2 \text{ cm}^2 \text{ V}^{-1} \text{ s}^{-1}$ . The doping density is found to be too high for using in  $p - n^+$  junctions. In addition, surface states cause a reduction in the bandgap at the interface. This results in the low open circuit voltage values obtained so far (33,36). The record efficiency of pyrite cells, achieved in 1991 is 5.52%, (37). There has been a stagnation in progress towards reliable photovoltaic systems based on pyrites. Other reasons are that many phases of iron sulfide exist, which makes it hard to have phase pure pyrite. Among these phases, for example, there are orthorhombic marcasite  $FeS_2$  and hexagonal troilite  $FeS$ , which, while being common phases, both exhibit much narrower bandgaps. This means that even trace amounts of these phases will adversely affect the performance of pyrite solar cells (20,38).

Other heavily studied earth abundant semiconductor is chalcocite,  $Cu_2S$ . This material exhibits direct bandgap value of 1.16 eV. For some years there was a controversy on the bandgap type of the material (39). Today it is accepted that it is indirect (40). A device based on this material has demonstrated

the record efficiency of 10.1% in 1981 (39). For this device, the acceptor density of  $\sim 10^{19}$  caused the space charge region to be extremely narrow. In addition, the absorption coefficient reached value  $5 \times 10^4 \text{ cm}^{-1}$  at wavelengths around 650 nm, causing a major current loss due to the fact that the absorbing layer is only 300 nm thick (39).

The interest in this material had declined since mid-1980s, due to the inability to increase the efficiency and long-term degradation of absorber layer. *Cu* atoms out-diffuse into *CdS* at the junction and to from the interface, forming  $\text{Cu}_2\text{O}$ , and hence converting chalcocite,  $\text{Cu}_2\text{S}$  to djurleite with the formula of  $\text{Cu}_{1.96}\text{S}$  (41). This process causes a reduction in minority carrier diffusion length, increases the bandgap and reduces the absorption coefficient (42). There has been a new flux of research papers on this material, but the stability problems are still to be addressed (33). For a short review of some other proposed materials such as *SnS*,  $\text{Cu}_2\text{SnS}_3$ ,  $\text{CuSbS}_2$  and  $\text{Cu}_3\text{BiS}_3$ , one can refer to (33).

One common challenge with many earth abundant semiconductors is the complexity of the phase diagrams, which make the synthesis of the desired material a difficult task. For instance,  $\text{Cu}_2\text{SnS}_3$  is just one of the 18 ternary phases observed for Cu – Sn – S system (43). Another issue is the phase stability and phase transformations. As stated earlier, this is a major obstacle for  $\text{Cu}_2\text{S}$ ,  $\text{FeS}_2$  and *CZTS* systems. Elements showing high oxidation state are also prone to reduction in oxidation number, hence changing the composition of the active layer and degrading the properties. The weakest bonds in a compound are often the ones attributed to cation exhibiting the highest oxidation state (31). This means that a reasonable candidate for earth abundant photovoltaic material should have these two conditions: a) cations with low number of oxidation states, so that the cation does not have many options for switching its oxidation state. b) cation that employs stable, low oxidation state.

### 1.2.2 $\text{Zn}_3\text{P}_2$

In addition to these factors, a potential candidate material for next generation thin film solar cells based on earth abundant semiconductors should exhibit adequate opto-electrical properties, such as direct bandgap close to optimal values of Shockley-Queisser limit, good carrier mobility, absorption coefficient and minority diffusion length (44).

Considering all the factors regarding the abundance and material costs, phase diagram complexity, phase stability and requirement for low oxidation number and opto-electrical properties,  $\alpha\text{Zn}_3\text{P}_2$  appears to be an interesting candidate. In terms of opto-electronic properties,  $\text{Zn}_3\text{P}_2$  demonstrates high absorption, of more than  $10^4 \text{ cm}^{-1}$  in the visible range of the electromagnetic spectrum (45,46) and reported direct bandgap close to the optimal value of the Shockley-Queisser limit (47,48). It is reported to have carrier diffusion length in the range of 5 – 10  $\mu\text{m}$  (49) and passive grain boundaries (50), which in turn could improve the performance of PV devices based on this material. Figure 1-1(b) illustrates the potential electricity production of this material compared to some other semiconductors. Due to the combination of low cost and extreme abundance, it was observed to have the second highest potential only after pyrite for large-scale photovoltaic application in the aforementioned reference (29). In addition, zinc-phosphorous system exhibits a fairly simple phase diagram (48,51,52), as depicted in Figure 1-2 (a).  $\text{Zn}_3\text{P}_2$  stoichiometry demonstrates two forms,  $\alpha\text{Zn}_3\text{P}_2$  and  $\beta\text{Zn}_3\text{P}_2$ , with  $\alpha\text{Zn}_3\text{P}_2$  being the desired phase for photovoltaic application due to its optoelectronic properties, as described later. This phase is stable over large parameter windows. As seen in Figure 1-2 (a) there is a second stoichiometry,  $\text{ZnP}_2$ , which also exhibits two phases. The

properties of these phases are not extensively studied. In contrary to  $\alpha\text{ZnP}_2$  and  $\alpha\text{Zn}_3\text{P}_2$ , both  $\beta\text{Zn}_3\text{P}_2$  and  $\beta\text{ZnP}_2$  are stable at high temperatures only. From now on, unless otherwise stated, what we mean by  $\text{Zn}_3\text{P}_2$  is  $\alpha - \text{Zn}_3\text{P}_2$ .

Historically, the first study of  $\text{Zn}_3\text{P}_2$  was performed by X-ray diffraction (XRD) in 1935 to investigate the synthesis and crystallography of this material. However, this material was abandoned until late 1970s, when researchers in the Institute of Energy Conversion at university of Delaware (53–62) started to investigate this semiconductor as a potential PV material. A group led by Suda in Japan explored different deposition techniques for this material, including RF sputtering, MOCVD, MBE, plasma assisted vapor phase deposition in late 1980s-early 1990s with varying material properties (63–67). Optoelectronic behavior of  $\text{Zn}_3\text{P}_2$  was studied during the same period of time in Wroclaw University of Science and Technology (68). A team lead by Harry Atwater at Caltech in late 2000s and early 2010 was one of the few major groups working on this material (47,50,69–73). This group has managed to make working photovoltaic cell with the efficiency of 4.5% in 2010, which still does not match the efficiency of 6% achieved by the group in university of Delaware in early 1980s (54).

Despite these promises,  $\text{Zn}_3\text{P}_2$  has not yet been adopted as a mainstream PV material due to the challenges in its growth and doping as the highest performing device from this material has the efficiency of 5.96%, and was demonstrated in 1981 employing a Schottky barrier (54). It is proven to be difficult to fabricate zinc-phosphide homo-junctions (20). Heterojunctions using  $\text{Zn}_3\text{P}_2$  have not exceeded the efficiency range of 2% (53,54,74). One major limitation for growth of  $\text{Zn}_3\text{P}_2$  is the lack of substrates that can be used for epitaxial growth of this material.  $\text{Zn}_3\text{P}_2$  has the space group of  $P4_2/nmc$  ( $D_{4h}^{15}$ ) (75) with a tetragonal unit cell consisting of 16 P and 24 Zn atoms and unit cell parameters  $a = b = 8.0889 \text{ \AA}$  and  $c = 11.4069 \text{ \AA}$  (76). For comparison, GaAs has a cubic unit cell with  $a = b = c = 5.6533 \text{ \AA}$ . Each unit cell has five and four planes of P and Zn atoms, respectively as demonstrated in Figure 1-2 (b). Another important feature of the  $\text{Zn}_3\text{P}_2$  is the presence of a total of 8 vacant sites in Zn planes per unit cell, which have important consequences for the intrinsic doping of this material as discussed in the following paragraphs. The large lattice parameters limit the flexibility for substrate selection. Early studies on this material used a variety of substrates including mica and steel (77,78). However, these substrates were later abandoned due to the poor epitaxy for thin films grown on these substrates. GaAs(100) and ZnSe(100) substrates have been used for epitaxial growth of thin films of  $\text{Zn}_3\text{P}_2$  as the lattice mismatch is 1.3% and 1% between the anion sub-lattices of these substrates and  $\text{Zn}_3\text{P}_2(100)$  (50,65,66). Still, the thickness of single crystal, epitaxial  $\text{Zn}_3\text{P}_2$  was limited to 150 nm, as strain relaxation, a large increase in resistivity and a consequent reduction in the hole concentration was seen for thicknesses above 150 nm (50).

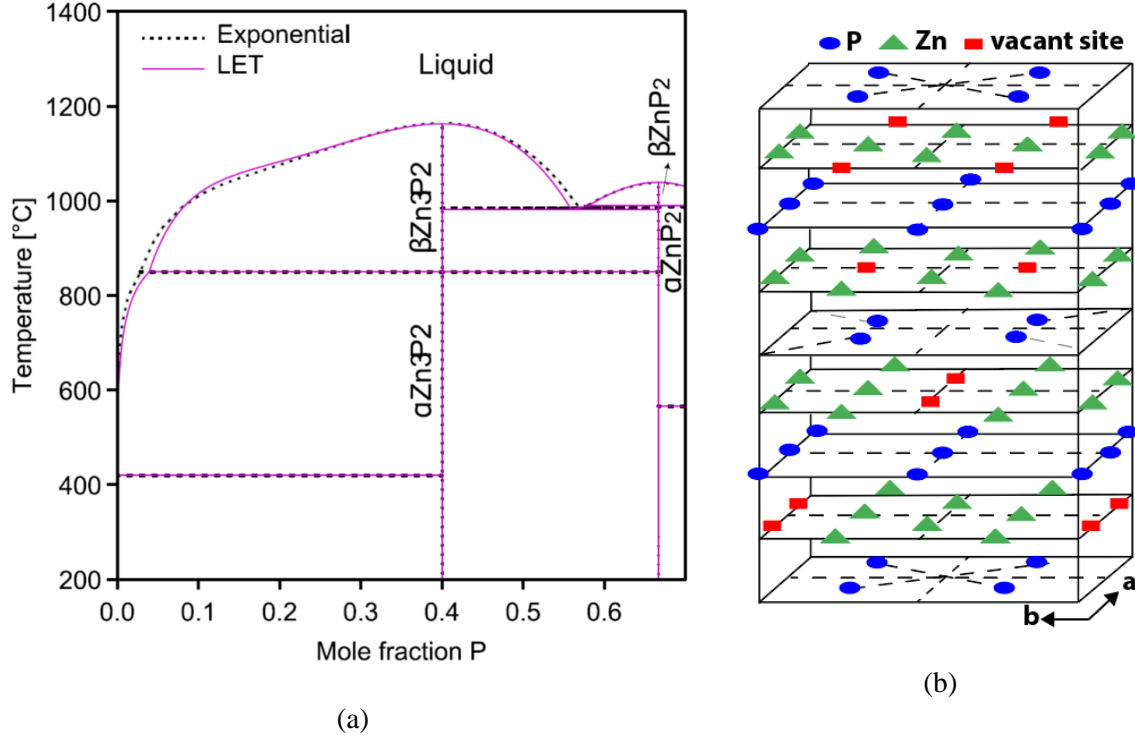


Figure 1-2. (a): the phase diagram of  $Zn - P$  system, taken from (48) with permission © elsevier (b): The unit cell of  $Zn_3P_2$ , showing the position of  $Zn$  and  $P$  atoms in addition to the vacant sites. This figure is adopted from (79) with some modifications with permission © APS.

Thermal expansion coefficient of  $Zn_3P_2$  is  $12.4 \times 10^{-6} K^{-1}$  at room temperature. For comparison, this coefficient is below  $6 \times 10^{-6}$  and  $3 \times 10^{-6}$  at the same temperature for GaAs and Si, respectively (80,81). This large difference in thermal expansion coefficient makes post-growth cracks very common for thin films of  $Zn_3P_2$  grown at high temperatures (50,65), further affecting the opto-electronic properties of the films. Hence, a low temperature technique for growth is needed if  $Zn_3P_2$  is to be grown for PV applications.

Another fundamental issue with  $Zn_3P_2$  is doping. As mentioned before,  $Zn_3P_2$  unit cell hosts 8 vacant sites per 40 atoms of its unit cell. These abundant empty sites in Zn planes are energetically favorable positions for incorporation of P interstitials, making  $Zn_3P_2$  intrinsically p-doped (55,82). The electrical properties of zinc phosphide depend on growth method as different growth methods result in different concentrations of P interstitials. Based on these observations, systematic control of P interstitials would be the first step for controlled doping of zinc phosphide. However, this would not be possible without controlling the defect density in the  $Zn_3P_2$  crystals as the presence of grain boundaries can affect the movement of interstitial atoms within the lattice. The beforementioned problems with growth of high-quality  $Zn_3P_2$  films should be addressed in order to properly tune the doping properties of this material.

Extrinsic p-doping of zinc phosphide is reported using Ag (83). The results of this study show that, while the low concentration incorporation of silver at  $Ag:Zn_3P_2 < 5 \times 10^{-3}$  does not affect the growth morphology of  $Zn_3P_2$ , higher Ag fluxes will result in the roughening of the surface and appearance of few twins, suggesting the initiation of Ag-alloying or maybe phase separation.

N-doping of this material has been even more challenging than p-doping. Similar to  $ZnSe$  (84), self-compensating intrinsic p-doping is observed to prevent from effective n-doping. The record efficiency of 6% was achieved for a device having Mg Schottky contacts to  $Zn_3P_2$  (54). In (69), it was reported that  $Mg$  impurities compensate the intrinsic p-type doping of the  $Zn_3P_2$  films. Early studies claim Mg diffusion into  $Zn_3P_2$  results in n-doped zinc phosphide (85,86). These results, however, were rejected as it was shown that the n-doping is done by formation of compounds like  $Mg_3P_2$  (65). The controversy around the nature of the Mg doping in  $Zn_3P_2$  is still not settled. N-type zinc phosphide grown by separate-source molecular beam epitaxy (MBE) was demonstrated in ref. (65). One should note the extremely high incorporation of excess  $Zn$  into the doped film at 17% (83). Cation replacement of  $Zn$  by  $Al$  had been used to compensate the intrinsic p-doping observed, but the concentration of  $Al$  that could be incorporated into the films without disruption of crystal structure had not been high enough to go to n-dope region. Anion replacement of  $P$  by  $S$  was also studied as a possible n-doping mechanism, but the incorporation of  $S$  at low fluxes resulted in reduction of the lattice constant, while high fluxes result in strain relaxation, which is likely to be due to the onset of phase separation (83). In addition, the highly volatile nature of  $S$  makes it impractical to be used in ultra-high vacuum systems MBE.

In principle, since  $Be$  belongs to the same group as  $Mg$ , it should have similar electronic effects on the crystal of  $Zn_3P_2$  if the  $Mg$  really acts as dopant and does not form new phase within the structure. However, the well documented extreme toxicity of  $Be$  (87) limits its ability to be used as a dopant for large-scale production of  $Zn_3P_2$  thin films.

The bandgap of  $Zn_3P_2$  has been studied using a host of different techniques such as photoluminescence spectroscopy (PL) and reflectivity and absorption measurements (47,88,89). While there had been contradicting measurements on the values of direct and indirect bandgap emissions of  $Zn_3P_2$ , the literature is now settled on indirect bandgap in 1.3 – 1.4 eV range, and direct bandgap of 1.5 eV (90), which is consistent with density-functional theory (DFT) calculations (91). It is to be noted that the optical behavior of  $Zn_3P_2$  is highly affected by defect-caused pair transitions. In (87), different optical behaviors were observed for four different  $Zn_3P_2$  samples grown with chemical transport method and the defect-related transitions were speculated as the origin for these differences. Indeed, enhanced recombination is linked to the presence of defects in  $Zn_3P_2$  (55,92). Furthermore, the localized electrostatic or bandgap fluctuations induced by defects is also found to indirectly affect the defect-mediated optical behavior of this material (92–94). Different reported energy levels for acceptor-like defects in  $Zn_3P_2$  are listed in (90), demonstrating the discrepancies between the observed optical behaviors of this material by different groups. In addition, the optical emission of  $Zn_3P_2$  nanowires (NWs) have been shown to be highly dependent on their stoichiometry (95). The different growth techniques and parameters used in the literature will result in different stoichiometries and defect concentration in  $Zn_3P_2$ , which can explain the difference in the optical behavior of the samples.

$Zn_3P_2$  has shown exceptionally high absorption coefficient  $> 10^5 cm^{-1}$  at room temperature (96), which is even higher than the absorption coefficient of high-quality  $GaAs$  (96). Indeed, a recent study revealed that NWs made from  $Zn_3P_2$  outperforms zinc blende (ZB) and wurtzite (WZ)  $GaAs$  and WZ  $GaP$  (45). However, it is to be noted that similar to other properties, there is a high variation in the reported measurements of absorption coefficients for  $Zn_3P_2$  (45,46,97,98), which is likely due to the difference in defect concentration.



Polycrystalline  $Zn_3P_2$  exhibit high carrier diffusion length in 5 – 10  $\mu m$  range. Early studies measured the hole mobility of  $Zn_3P_2$  to be around  $10\text{ cm}^2\text{V}^{-1}\text{s}^{-1}$  (90). In (45), it was observed that the hole mobility increases as a function of thickness up to 150 nm with the maximum hole mobility around  $45\text{ cm}^2\text{V}^{-1}\text{s}^{-1}$ . For film with higher thicknesses, partial relaxation and cracking upon cooling caused the mobility to reduce to  $< 20\text{ cm}^2\text{V}^{-1}\text{s}^{-1}$ , which is compatible with the previous observations on polycrystalline  $Zn_3P_2$  thin films (60). It is to be noted that this mobility value is still one order of magnitude higher than the maximum observed mobility in  $FeS_2$ . To observe the formation of dislocation and cracking as a consequence of increased thickness, one can refer to Figure 1-3 (a), which shows a low-magnification cross-sectional TEM image of a  $Zn_3P_2$  thin film with the thickness of 50 nm grown on  $GaAs$  substrate. No crack or threading dislocation is seen, which is opposite of observation for  $Zn_3P_2$  thin film with the thickness of 150 nm shown in Figure 1-3 (b). The red arrow in this figure indicates the initiation of a threading dislocation, formed as a consequence of strain relaxation.

The effects of the increased thickness and the resulting strain relaxation on the electrical properties of the films are shown in Figure 1-4. In Figure 1-4 (a), (b) and (c), the vertical axes show resistivity, hole density and hole mobility, respectively, while the horizontal axes denote the thickness. In addition, hollow and filled circles are used to indicate partially relaxed and strained films. Initially, the resistivity curve shows a decreasing trend with respect to the thickness, which is then reversed around the thickness of 150 nm. At this thickness, the films are relaxed and the resistivity starts to increase. Hole density and mobility, on the other hand, initially have increasing trends with respect to the thickness, which are then reversed due to the strain relaxation for thicknesses around 150 nm. The increase in the mobility as a function of thickness can be attributed to the relative reduction of surface carrier scattering effects. One could assume that preventing from crack formation would make the increase in the mobility as a function of thickness to continue in monocrystalline thin films. This in turn would result in higher values of carrier diffusion length, further improving the potential of this material for opto-electronic applications. Modeling in (60) has estimated the hole mobility of high-quality, single crystalline  $Zn_3P_2$  to be around  $1000\text{ V}^{-1}\text{cm}^2\text{s}^{-1}$ .

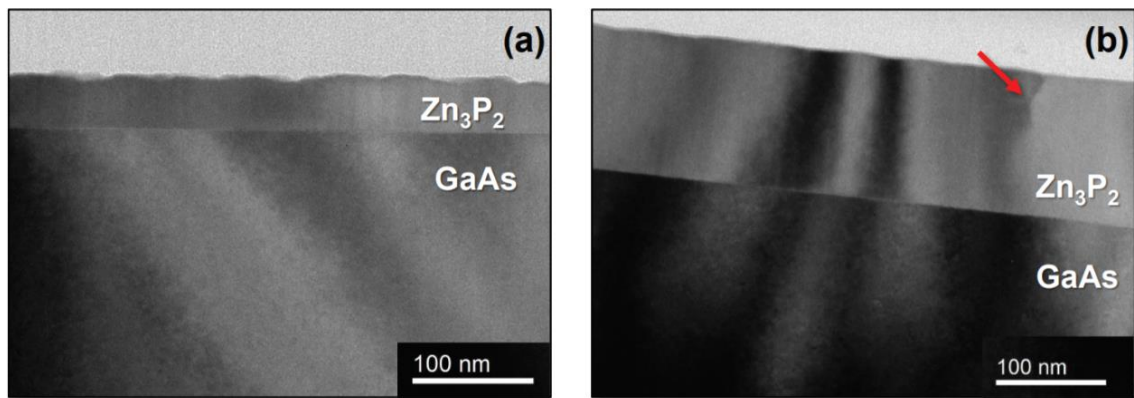


Figure 1-3: Bright field transmission electron micrographs of pseudomorphic  $Zn_3P_2$  layers with thicknesses of (a) 50 nm and (b) 150 nm. The red arrow in (b) indicates the initiation of a threading dislocation due to the onset of strain relaxation. These figures and their caption are taken from (83) with permission from Dr. Jeffrey Paul Bosco.

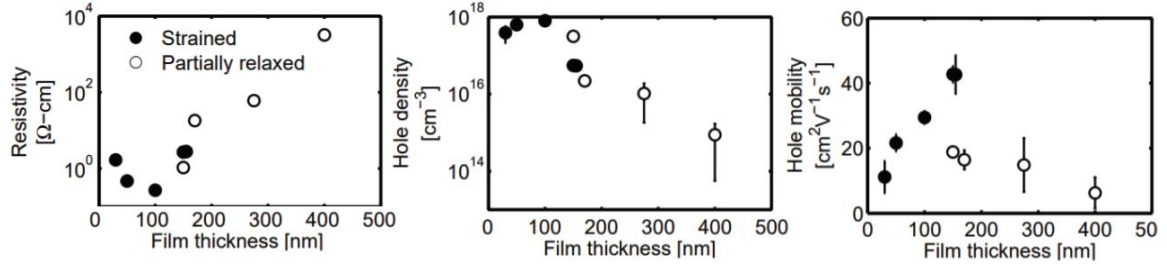


Figure 1-4: Hall Resistivity, hole carrier concentration, and hole mobility measured in van der Pauw configuration as a function of  $Zn_3P_2$  epilayer thickness. The filled and open circles represent the data collected on strained and partially relaxed films, respectively. These figures and the captions are adopted from (83) with permission from Dr. Jeffrey Paul Bosco.

Based on this short review of the properties and challenges of  $Zn_3P_2$ , eliminating defects and making thick monocrystalline thin films of this material have been one of the main goals of this thesis. This will improve the optical properties, carrier mobility and diffusion length. In addition, it paves the way for controlling/ suppression of intrinsic p-doping, which in turn could render controlled n-doping of this material possible. Due to the limitations discussed before, the growth technique should employ a relatively low growth temperature to prevent from cracking and offer a high degree of control over growth parameters. Given these considerations, separate- source MBE is chosen as the growth method as the flexibility it offers is not matched by any other technique. After achieving high-quality, thick monocrystalline thin films, a variety of characterization techniques are used to shed light on the difference in the properties of monocrystalline and polycrystalline  $Zn_3P_2$  thin films.

## 1.3 GaAs Nanowires

### 1.3.1 Motivation for studying the growth of GaAs Nanowires

GaAs is the second highly studied and used semiconductor after Si. At room temperature, it has high electron and hole mobilities of  $8500 \text{ V}^{-1}\text{cm}^2\text{s}^{-1}$  and  $400 \text{ V}^{-1}\text{cm}^2\text{s}^{-1}$ , respectively, absorption coefficient of  $10^4 \text{ cm}^{-1}$  and direct bandgap of 1.42 eV (99), which is very close to the optimal bandgap value for Shockley-Queisser limit. Indeed, at 27.6 %, *GaAs* holds the record for the highest efficiency single-junction solar cell (100). Due to the combination of its properties, it is used in space applications (99), high-performance concentrated PV (101), radio frequency (RF) emitters (102), lasers (103), light emitting diodes (LEDs) (104) and other areas.

Despite its superior material properties, record efficiency and the enthusiastic effort of the research community, it has failed to compete with Si photovoltaics on a commercial level. Among the reasons for this lack of success is the high price of GaAs compared to Si (105–107), stemming partly from the lack of production scale that Si enjoys and partly from the relative scarcity of Ga compared to Si. Indeed, from Figure 1-1 (a), one can observe that constituting elements of *GaAs* are 4 orders of magnitude less common than Si in the earth's crust. *GaAs* itself is too expensive to be used as the substrate for homoepitaxy on an industrial scale needed for widespread PV use. In addition, the growth of *GaAs* thin films on dissimilar substrates is not easy due to the lattice mismatch, which will

result in formation of detrimental defects. Polarity mismatch between *GaAs* and the substrate can cause the formation of antiphase boundaries and further adds to the challenges of *GaAs* heteroepitaxy (108). Adopting NW geometry has been proposed as a way to tackle these issues at the same time. NW cross sectional dimensions are smaller or comparable to the radiant light wavelength, causing interference and guiding effects to dictate the optical behavior of the NWs (109,110). In the case of low-absorbing materials such as indirect bandgap semiconductors, the wavelength effects play the dominant role (111). On the other hand, highly absorbing materials such as direct III-V semiconductors exhibit resonances that enhance the absorption by many factors. (109) One can consider this effect as if NWs act as a built-in concentrator of the incident light. This increases the absorption and efficiency of solar cells made of NWs. A solar cell composed of single *GaAs* NW has shown the potential to go beyond Shockley–Queisser limit, due to having absorption cross-section that is many times higher than its actual cross-section and effective light concentration around 12 (109). This means that for absorbing the same amount of light, much less material is needed, which could address issues related to the high price of *GaAs*. Furthermore, due to their low footprint to sidewalls area ratio, NWs can effectively relax the strain they have from lattice mismatch with the substrate at their sidewalls, which adds flexibility in terms of the substrate used as support for the solar cell (112–115). Understanding the fundamentals of *GaAs* NW growth will bring new understanding on the synthesis of high quality *GaAs* and therefore contribute to its implementation in PV and/or other applications.

### 1.3.2 Properties of *GaAs* Nanowires

Similar to other non-nitride III-V semiconductors, bulk *GaAs* exhibits a cubic ZB phase, which implies an ABCABC atomic stacking in the (111) direction. The ZB unit cell and its stacking are illustrated in Figure 1-5 (a) and Figure 1-5 (b), respectively. However, at nanoscale, *GaAs* can assume hexagonal WZ structure with ABAB atomic stacking. This is the bulk phase for nitride-based III-V semiconductors such as *GaN*. Figure 1-5 (c) and Figure 1-5 (d) show *GaAs* WZ unit cell and its atomic stacking.

Increased surface energy contribution to the overall energy balance of the system, which is inherent to nanoscale structures, is one of the reasons for the formation of WZ phase in III-V nanowires (116). The formation of a rotational twin along the  $\langle 111 \rangle$  growth direction in ZB causes a local change in the atomic stacking and can be considered equivalent to a WZ half-monolayer (117,118). Successive formation of this type of twinning in ZB can cause a full transition to WZ so the propensity of NWs for having WZ inclusions makes them prone to be highly defective, as commonly observed in the literature (119–122).

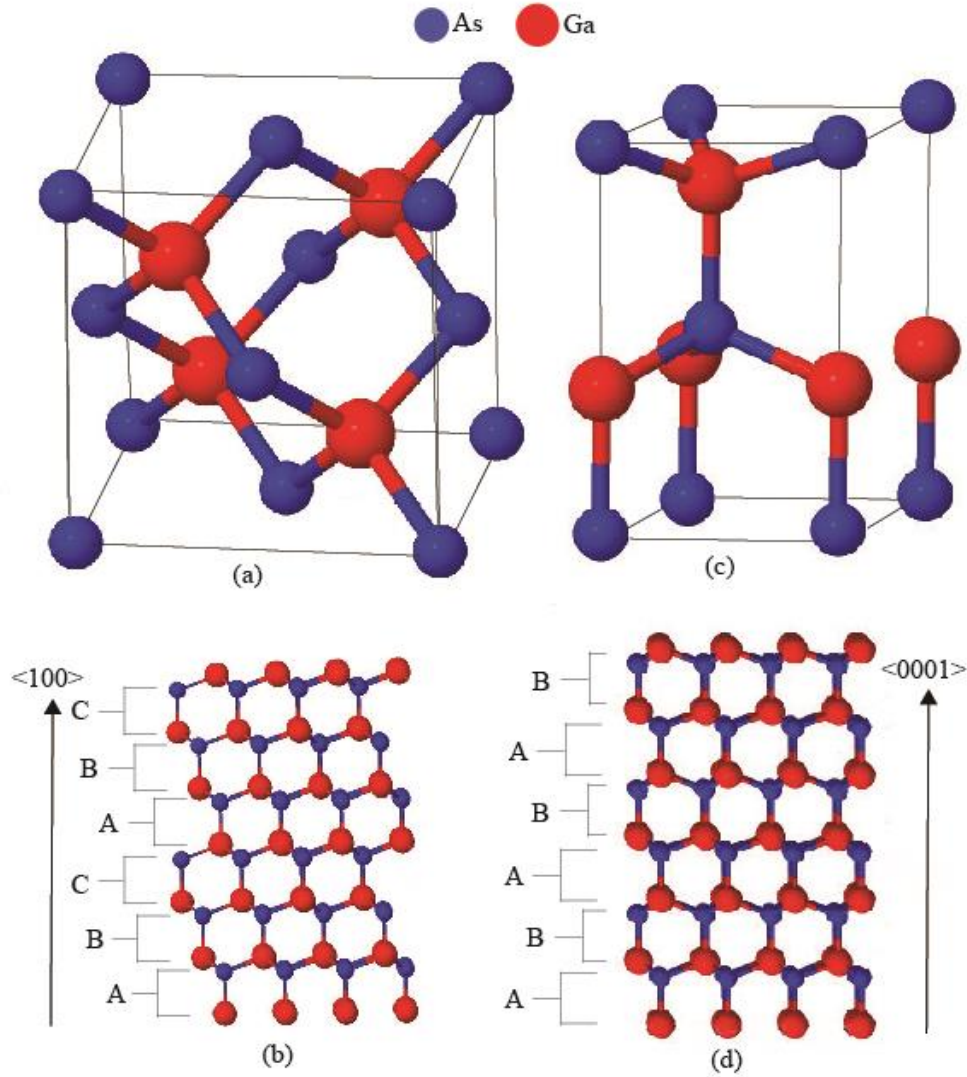


Figure 1-5. (a) ABCABC stacking of ZB GaAs. (b): Cubic ZB unit cell of *GaAs*. (c) ABAB stacking of WZ GaAs. (d) Hexagonal unit cell of WZ *GaAs*. These images are made by Rhodius software (123).

Another important feature of *GaAs* that has major implications for the growth and properties of *GaAs* NWs is polarity, which refers to the inherent electrical dipole due to the ionisity of Ga – As bonds, translated to an inherent electrical field in certain crystal directions <sup>[104,105]</sup>. For kinetic reasons, NWs tend to grow in (111) direction. In arsenide and phosphide-based NWs, the (111) growth direction is commonly terminated by group V elements (120,126,127). This configuration is called B-polar growth and is in contrast to the rare cases of A-polar growth in which the (111) direction is terminated with group III elements. These two polarities have striking differences in terms of NW morphology, crystalline quality and opto-electronic properties. For instance, while the before-mentioned occurrence of high defect concentration and WZ inclusion in III-V NWs is very common in B-polar growth, they have not been observed for A-polar NWs <sup>[106,108]</sup>. This high crystalline quality of A-polar NWs makes them more desirable. However, their growth has been very rare and challenging due to the thermodynamic reasons.

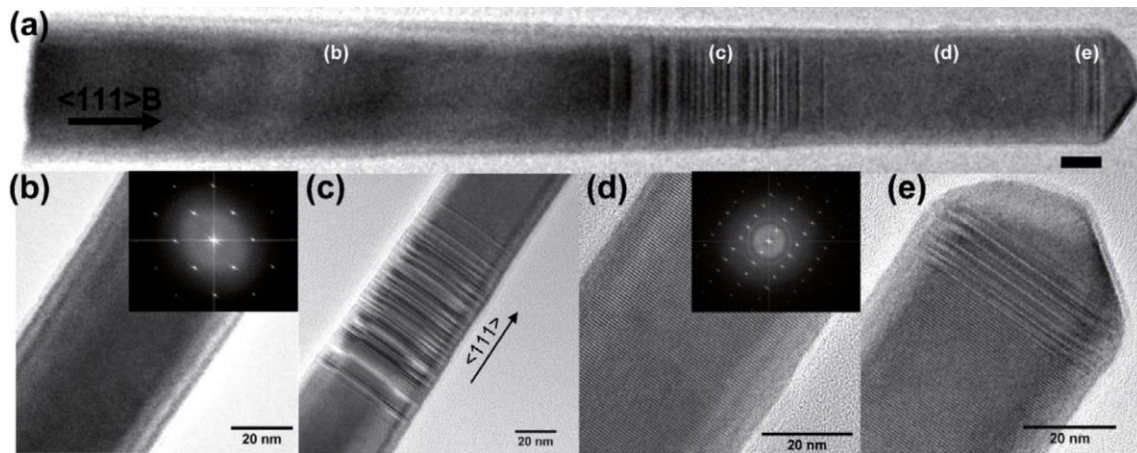


Figure 1-6. Polytypism and defects in *GaAs* NWs. (a) Low magnification TEM image of a *GaAs* NW. The bottom of the NW demonstrates a ZB structure with very low defect density. The middle section has mixed phase and hosts a high density of defects, before a pure WZ structure towards the tip. The tip has ZB phase tip with many stacking faults below. Higher magnification images of different regions are shown respectively (b), (c), (d), (e). These images and the caption are adopted from (129) with permission © IOP.

Similar to *InAs(Sb)*, *GaAs* NWs grown along  $\langle 111 \rangle$  directions adopt a hexagonal cross section to minimize their overall surface energies (130,131). Elemental segregation has been observed at the corners of this hexagonal cross section in core-shell *GaAs* – *AlGaAs* NW structures (132). Different crystallographic planes have different levels of elemental segregation due to the discrepancy in their surface energies. Differential elemental concentration of *Al* causes the formation of quantum dots (QDs)(132,133) due to the band alignment between *GaAs*, *AlGaAs* and *AlGaAs* QDs.

In core-shell QDs, The optical properties of QDs depends on the composition and the thickness of the shell (134). In addition, the crystalline quality of the core NW directly affects the emission of the QDs embedded in the shell as defects in core can propagate to the shell, causing centers for radiative recombination and reducing the emission quality through peak broadening. Elimination of defects in the core NW can improve the optical behavior of these systems. Indeed, A-polar core-shell *GaAs/AlGaAs* NWs, which, as discussed before, have a phase-pure and defect-free ZB structure are shown to have superior QD emission compared to their B-polar counter-parts in terms of intensity and peak width (117). Understanding the mechanism of A-polar growth therefore can be beneficial for improving the optical behavior of *GaAs* NWs.

### 1.3.3 Methods for the Growth of Semiconductor Nanowires

Growth rate anisotropy is a requirement for achieving the one-dimensional geometry of the NWs. While some solution-based methods have been used to achieve this purpose (107), most of the research is focused on vapor-based epitaxy of NWs. The most common method to achieve growth anisotropy in vapor-based growth of NWs is using a catalytic nanoscale particle that gathers gaseous precursors from the growth chamber and incorporates them into the NW structure upon supersaturation (135). Growth mechanisms are divided into vapor-solid-solid (VSS) and vapor-liquid-solid (VLS) modes based on the phase of this catalyst particle. While VSS growth can offer sharper interfaces, it offers lower growth rate compared to VLS (136). The mechanism of VLS growth was identified in a seminal paper by Wagner and Ellis (137) in 1964 on a Si – Au system. Normally, the initial position of the droplet is defined by the mask layer on the substrate as the droplets are gathered in the holes that are present in the mask. Figure 1-7 demonstrates the VLS growth of *GaAs* NWs on *GaAs* substrate covered with a *SiO<sub>2</sub>* mask. In addition to these two methods,



vapor-solid (VS) is an important mechanism that is heavily used in NW growth. As the name implies, there is no catalytic particle involved in this process and the gaseous particles are directly incorporated into the solid structure. VS growth is based on the difference in the growth rates of the different facets of a crystal (136). The growth of shells in core-shell structures is done employing VS mechanism.

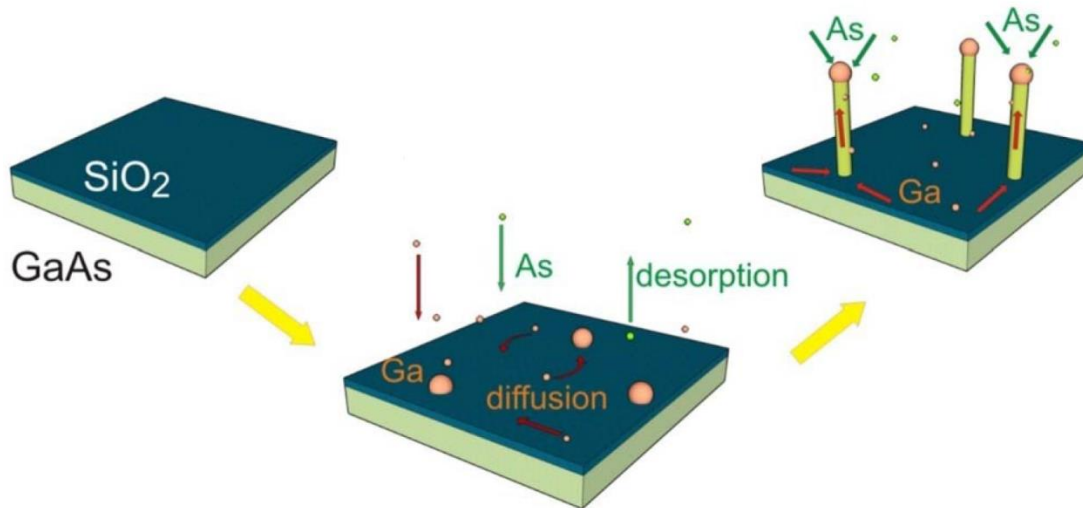


Figure 1-7. Growth of *GaAs* NWs on a *GaAs* substrate. The *SiO<sub>2</sub>* mask determines the initial position of the droplet and thus, the NWs. This image is taken from (138).

The choice of the catalyst particle in VLS growth has significant consequences for the properties of the NW. For instance, while VLS growth of *GaAs* is easier with Au catalyst, the incorporation of gold into the NW structure has significant negative effects on the opto-electronic properties of the NW due to the formation of deep levels in *GaAs* (138). Furthermore, gold is generally avoided in *Si*-based semiconductor industry due to the destructive effects it has on the performance of *Si* devices (139). Using native Ga as the catalyst droplet has been proposed as a way to solve these issues (138). Due to its importance, we have focused on this growth method for *GaAs* NWs in this thesis.

Models describing the VLS growth of NWs have been mostly focused on the macroscopic properties of the catalyst droplet and the phases involved in the process. Thermodynamic considerations about the nucleation enthalpy and the surface energies of the interfaces were first employed to justify the growth of WZ phase in III-V semiconductor NWs(116). The contact angle of the droplet is increasingly linked to various aspects of NW growth such as polytypism. It is observed that ZB grows at higher contact angles than WZ (116,140,141) and lower contact angles are linked to an increased probability of defect formation(126). The shape and configuration of the droplet at the early stages of growth has a fundamental effect on the growth quality and direction of NWs (142). In (126), tuning the contact angle and droplet volume was used to switch the growth direction in self-catalyzed *InAs* NWs. Furthermore, contact angle engineering was employed to switch the polarity of gold-catalyzed *GaAs* NWs, while the In (126). Noticeably, in-situ studies have established a link between contact angle and the ratio of As and Ga fluxes, known as *V/III* ratio (141): increasing the *V/III* ratio reduces the contact angle, which in turn makes the formation of WZ and defects more likely.

All the observations and modeling up to this point have, however, neglected the atomistic and discrete structure of the interface between the droplet and the underlying NW crystal. Indeed, up to now, the boundary between the droplet and the NW is considered as binary, sharp interface. This is in contrast with the observation in other systems in which a gradual transition from crystalline interface to amorphous liquid is reported (143–150). The periodic potential imposed by the crystalline lattice of the solid makes the adjacent atoms in the liquid phase to adjust a semi-structured configuration with properties that are different from those of atoms in the bulk of the droplet. This fact, however, has been neglected up to now in the modeling of VLS process. The general difficulty in probing such ordering of liquid at the interface could be considered as a reason for this omission: the ordering extends just for a few nanometers and is very delicate. Consequently, most characterization techniques do not have the spatial resolution for probing this ordering. High resolution transmission electron microscopy (HRTEM) is employed to investigate the ordering of liquid *Al* in contact with  $Al_2O_3$  (143,145,147,150). However, the contrast variation in HRTEM images is hard to interpret as it is affected by thickness/ focus parameters and delocalization effects (151). In addition, HRTEM cannot distinguish different polarities of the structure and thus cannot be used to investigate the difference in the liquid ordering between A and B polar *GaAs*. In addition, chemical analysis of the interface using core-loss electron energy loss spectroscopy (EELS) and EDS is not possible as the high electron dose employed in these techniques will destroy the interface and the fragile structure of the ordered liquid.

In this thesis, we have studied the reasons for the fundamental different growth mechanisms of A and B-polar *GaAs* NWs through focusing on the liquid ordering at interface between the NWs and the catalyst droplet in self-catalyzed *GaAs* NWs. A combination of high-end electron microscopy and machine-learning based molecular dynamics (MD) simulations developed by external collaborators are employed to shed light on the difference between the growth of different NW polarities.

## 1.4 Thesis Outline

Chapter 1, **Introduction**, offers the motivations and the relevant literature review.

Chapter 2, **Methods**, will discuss the different techniques employed during this thesis. We first start by the description of the MBE machines used to grow the thin films and the NWs studied. The different characterization techniques that have been utilized to study the properties of  $Zn_3P_2$  thin films and *GaAs* NWs are then discussed. These include scanning electron microscopy (SEM), S/TEM and its variants, core loss EELS, principal component analysis (PCA), focused ion beam (FIB), Raman spectroscopy, photoluminescence (PL) spectroscopy, XRD, terahertz (THz) spectroscopy and conductive atomic force microscopy (C-AFM). Finally, a short section on the MD simulations and the machine learning techniques developed to conduct them by our collaborators is offered.

Chapter 3, **Results and Discussion**, divided into two sections, is composed of the peer-reviewed papers published providing our findings on  $Zn_3P_2$  thin films and *GaAs* NWs.

Chapter 4, **Conclusion and Outlook**, offers a short summary of the tasks achieved and the open questions relevant to this work.





## 2: Methods

This chapter reviews the main methods employed in this thesis. We start by describing the molecular beam epitaxy, MBE, which is the method used for the growth of  $Zn_3P_2$  thin films and the GaAs nanowires. Next, the methods used for characterization and investigation of the samples are discussed. These include electron microscopy and spectroscopy methods such as scanning electron microscopy (SEM), transmission electron microscopy (TEM), scanning transmission electron microscopy (STEM), energy-dispersive X-ray spectroscopy (EDX) and electron energy loss spectroscopy (EELS), focused ion beam (FIB), Raman spectroscopy and x-ray diffraction (XRD).

### 2.1 Molecular Beam Epitaxy for Growth of $Zn_3P_2$

#### 2.1.1 Structure and Working Principles

MBE is an ultra-high vacuum (UHV) method used mainly for studying the growth mechanism of semiconductors. Despite its high maintenance and operational costs, it is one of the main platforms of choice for understanding the fundamental aspects of crystal growth. The unique features of MBE include very high levels of control over growth parameters, extreme material purity and low contamination levels and the possibility of in-situ characterization.

The MBE used in this project for the growth of  $Zn_3P_2$  is a Veeco GENxplot system, shown in Figure 2-1. Different parts of this system are labeled to facilitate the description. The MBE machine used to grow the GaAs nanowires is extremely similar. In order to maintain the high purity levels and the ultra-high vacuum (UHV), this machine is divided into three main interconnected parts: load lock (a), preparation module (b) and growth chamber (c). The operations of the MBE are directed by the control unit (d). Load lock is used to load the samples and is the only place where the MBE is regularly opened from and exposed to air. In order to protect the UHV status and prevent from contaminations, it is separated from the rest of the machine through the gate valve (f). Upon loading the samples, the load lock turbo pump (e), which is backed up by a rough pump (not shown here) is started to lower the pressure and the first degassing stage is initiated by turning the load lock lamps on. The temperature is elevated to a set point (150°C in this case) and is maintained for  $\sim 2$ h. When the load lock pressure is low enough, the samples are transferred to the parking station (g). The transfer arm (h) is used to move the samples to the preparation module (b), where the temperature is again raised to further degas the samples. For the  $Zn_3P_2$  samples grown on  $InP(001)$  substrate, the degassing temperature is 300°C and the samples are kept at this temperature for two hours. An ion pump (not shown here) traps the contaminants released during the degassing and keeps the pressure low. The preparation module and parking spots are separated from the growth chamber through gate valve (i). Once the pressure in the preparation module is less than  $5 \times 10^{-9}$  mbar, the sample is transferred to the growth chamber (c) using the transfer arm (h). This chamber is kept at extremely low pressures by the cryopanel, a Ti sublimation and an ion pump (j). Heater (k) is lowered on the manipulator to control the growth temperature by radiative heating. This chamber is equipped with residual gas analyzer (RGA), shown by (m), for monitoring the pressure levels of different species inside the growth chamber and a quartz crystal monitor (QCM) for monitoring the growth rate. This is done by measuring the change in the vibrational frequency of the quartz crystal due to the added mass caused by the deposition (152). The

material sources, called cells, are located below the growth chamber at  $45^\circ$  with respect to the vertical axis of the growth chamber. Component (n) shows the zinc cell.

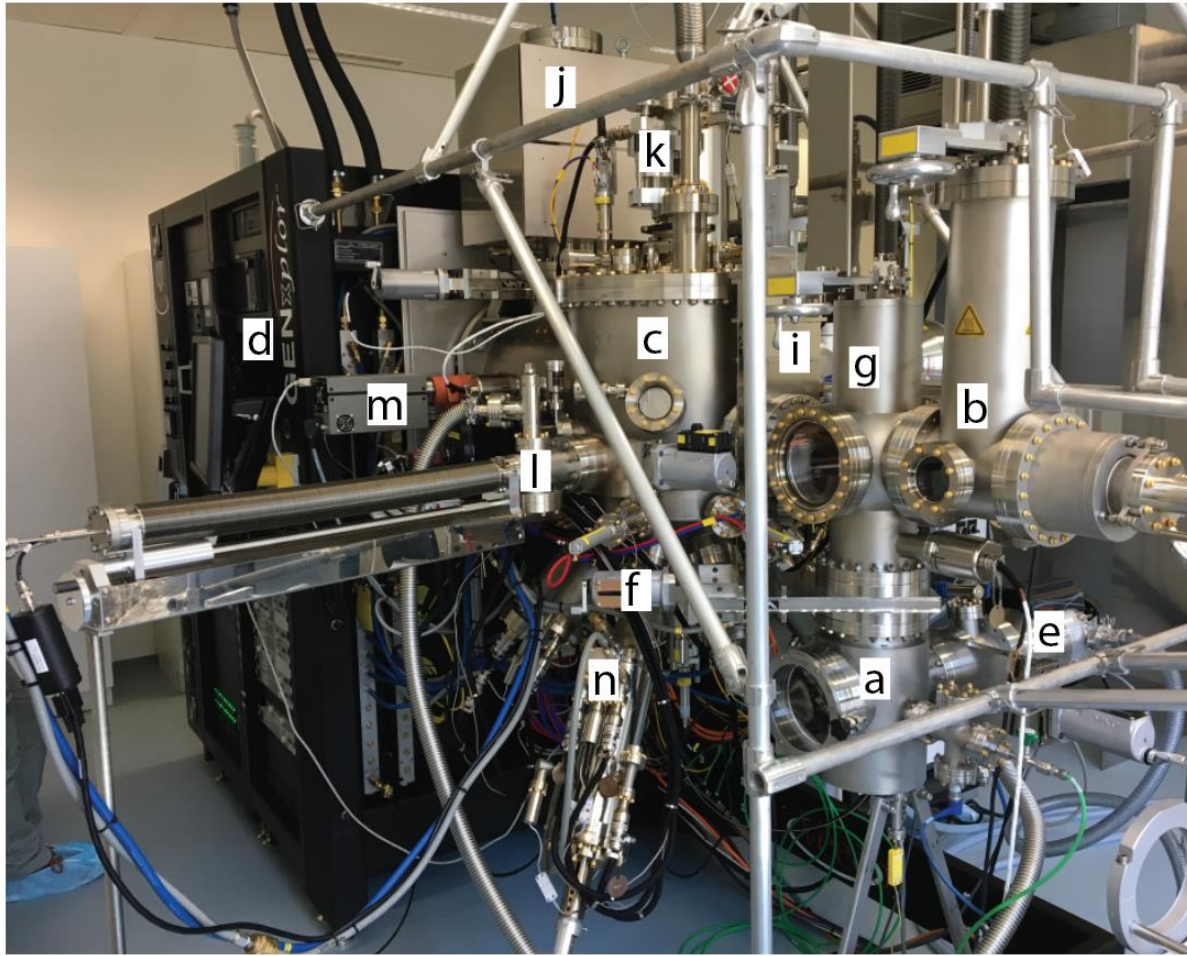


Figure 2-1. Veeco GENxplore and its components. (a): load lock. (b): preparation module. (c): growth module. (d): control unit. (e): turbo pump of the load lock. (f) the gate valve separating the load lock and preparation module. (g) the parking station for the sample. (h) the arm used to transfer the samples between the preparation and the growth chamber. (i) the gate valve separating the growth module from preparation module. (j): the  $Ti$  sublimation and iron pumps for the growth module. (k) the heater used to control the growth temperature, (l): QCM. (m): RGA.

A schematic view of the growth chamber is offered in Figure 2-2 (a). Cryopanel cooled by liquid nitrogen help keep the pressure low by trapping gas molecules. The chamber hosts a beam flux monitor (BFM), which is a pressure sensor used to calibrate the fluxes.

The effusion and cracker cells are used to generate the  $Zn$  and  $P_2$  fluxes, respectively. In our case,  $GaP$  is used as the precursor for  $P$  flux. Upon heating up,  $P_2$  is released before reaching the cracker. Increasing the cracker temperature will break the remaining of the  $P_4$  molecules into  $P_2$ , which is safe in contrast to the highly reactive  $P_4$ . In order to further increase the precision in the control of the fluxes, both of these cells are equipped with valves. Instead of changing the cell temperatures to adjust the fluxes, the cells are kept at constant temperatures and instead the degree of which the valves are open

is changed. This adds further stability and in addition is faster since changing the cell temperatures needs to be done gradually while controlling the valves is instant. For a review of MBE cell types, one can refer to (153).

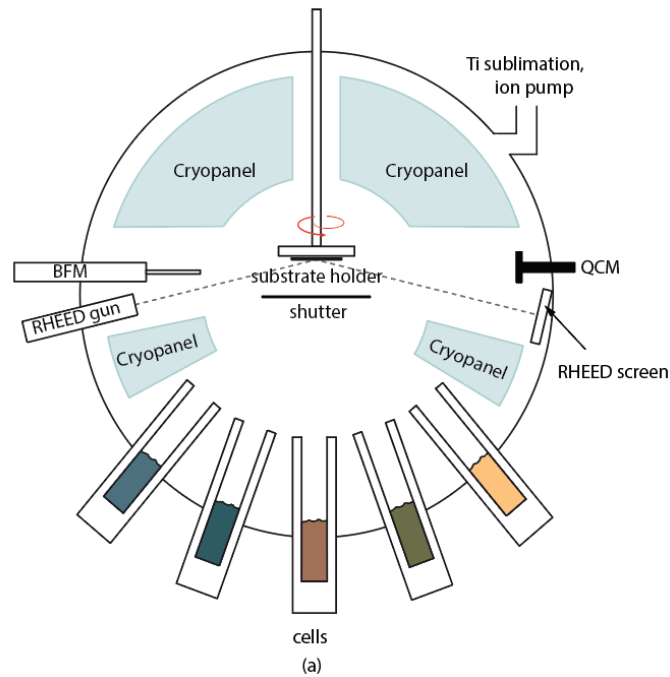


Figure 2-2. a schematic view of the growth chamber showing the cells, cryopanel, RHEED gun and screen, BFM and QCM. A shutter can be inserted between the substrate and the cells to block the atomic fluxes from reaching the substrate if needed. The sample is rotated to ensure annular homogeneity of growth fluxes. The chamber is kept at low pressures by Ti sublimation and ion pump.

An important capability of MBE systems is the use reflective high energy electron diffraction (RHEED), which can be used to have an in-situ assessment of the growth quality and rate. Electrons with high kinetic energies between 10 KeV and 50 KeV are radiated on the sample with very low grazing (otherwise known as glancing) angles between  $1^\circ$  and  $5^\circ$ . This very low angle makes this technique very sensitive to the surface as the penetration depth is very low. In addition, it makes RHEED benefit from the very large scattering cross sections at low angles (154). Electrons are diffracted upon the interaction with the sample and then shed on the RHEED screen used for visualization of the diffraction patterns. RHEED is not compatible with other growth techniques as ultra-high vacuum levels are required to have unperturbed electron beams. Based on the shape of these diffraction patterns and the oscillations in their intensities, one can obtain various information about the growth such as the crystal structure/orientation, surface flatness, grain size, epitaxial relation between the sample and the substrate, growth style in thin films and more (155). To understand the principles of RHEED, one should consider the concept of Ewald sphere, which is defined as a sphere in reciprocal space centered around the electron source with radius  $= |\vec{k}|$ , where  $\vec{k}$  is the wave vector of the electron beam. Assuming elastic scattering, diffraction patterns can be assumed as the intersection of this sphere and the reciprocal space of the lattice, projected on the screen (155). Figure 2-3 offers a visual representation of the reconstruction of the diffraction patterns.

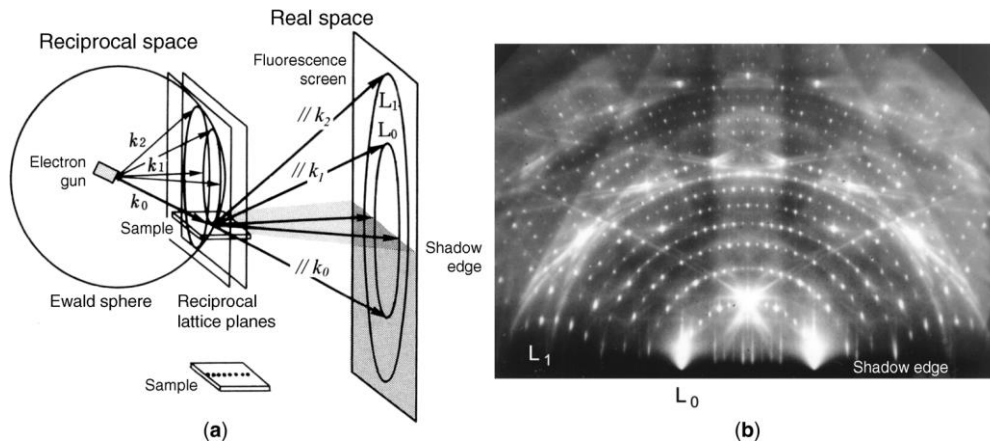


Figure 2-3. (a) Direct space and reciprocal space of RHEED. (b) pattern taken from a Si(1 1 1)( $7 \times 7$ ) reconstructed surface. The electron beam was 15 keV in energy with  $[11\bar{2}]$  incidence in azimuth direction and about  $3^\circ$  in glancing angle  $\theta_g$  to attain a surface-wave resonance condition. These images and their captions are taken from reference (155) with permission © Wiley.

Different surface configurations have different reciprocal spaces. This results in unique realization of diffraction patterns for each such configuration. For instance, a flat monocrystalline surface would have parallel lines with infinitely small thickness as its reciprocal space pattern. On the other hand, a flat surface featuring small domains has reciprocal space patterns with lines that have finite thicknesses. This make the RHEED pattern to change from the spots in the case of flat, monocrystalline surface to streaks in the case of flat surface with small domains. Some different surface configurations with their reciprocal space and RHEED patters are listed in Figure 2-4.

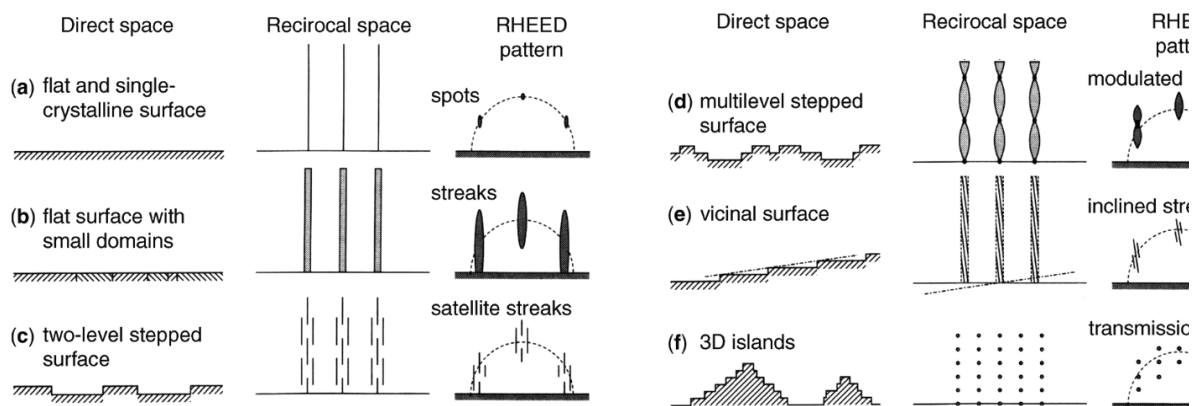


Figure 2-4. Different surface configurations and their corresponding reciprocal space and RHEED patterns. These images are taken from reference (155) with permission © Wiley.

In addition to understand the atomic configuration of the surface by looking at the diffraction patterns, the variations in the intensities of the dots in these patterns can also be used to monitor the growth rate. For a fully formed 2D surface with perfect lattice, the diffraction intensity is maximized. Addition of any atoms to the surface constituting a top incomplete monolayer will reduce the intensity of the dots in the diffraction pattern. At half of a monolayer the intensity is minimized. Adding new atoms from this point will increase the intensities again until a new layer is fully completed, in which case the

intensities are maximized again. Measuring the time between peaks can reveal the growth rate with high precision.

Using  $P$  for growth poses unique safety challenges that need to be adequately addressed. White phosphorous  $P_4$  can be deposited on the interior of MBE. This material is extremely flammable and is used for making military munitions (156), which are often banned by international treaties due to its very high burning temperature (157). In addition, it can turn into phosphine,  $PH_3$  after contacting with water and moisture, which is highly toxic and flammable (158). To mitigate these risks upon opening of the system, a  $GaP$  cell was used, which mainly produces  $P_2$  instead of  $P_4$ . In addition, a phosphorous recovery process was used to recover all phosphorous in the chamber before any opening of the chamber for maintenance. During the phosphorous recovery process, the main MBE chamber is heated up by covering it with a thermal tent and a dedicated cryopanel cooled down by liquid nitrogen is connected to the main chamber. The increased temperature causes the phosphorus to migrate to the cold point and stick to the walls of the external cryopanel. At the end of the process this is carefully removed and neutralized. This process involves the full immersion of the cryopanel in a large container filled with water.  $H_2O_2$  is added to convert the  $P_4$  to  $P_2O_5$ , which is then converted to a soluble phosphate solution by  $Al(OH)_3$ . The concentration of both  $H_2O_2$  and  $Al(OH)_3$  for this process is 30%. In addition, de-ionized water is used for squirting the dislodged phosphorous chunks which are brought to the water surface by bubbles. This neutralization process is carefully planned and conducted under a chemical fume hood that removes the released gases.

Now, we provide a short description of the MBE system P600 dual chamber from DCA Instruments used to grow  $GaAs$  NWs<sup>2</sup>. An schematic view of this system can be offered in Figure 2-5. The basic principles of this machine are shared with the system described for the growth of  $Zn_3P_2$  thin films. However, there are a few differences that are highlighted here. First, as suggested by its name, this machine is equipped with two separately operated growth chambers, which share the “central distribution chamber” (CDC). CDC hosts a robotic arm that handles all the transfer operations. This arm can be programmed and controlled remotely. In addition, this MBE system employs a hydrogen cleaning module, mainly used to clean the substrate surface before the growth of 2D  $GaAs$  thin films. In contrast to the Veeco GENxplot system, the parking and degassing stations are not directly connected as they are placed on different sides of the CDC. Growth chambers 1 and 2, load lock, parking station, degassing station and the hydrogen cleaning module are all separated from the CDC by UHV gate valves. The DCA system uses effusion cells for gallium, indium and aluminum, while cracker cells are implemented for arsenic and antimony. Each growth chamber is equipped with two cryopumps produced by CTI Cryogenics, in addition to two cryopanel cooled by liquid nitrogen.

---

<sup>2</sup> This system is also used for the growth of other III-V structures, such as  $InAs$  NWs,  $InAs/GaAs$  nano membranes and  $GaAs$  thin films.



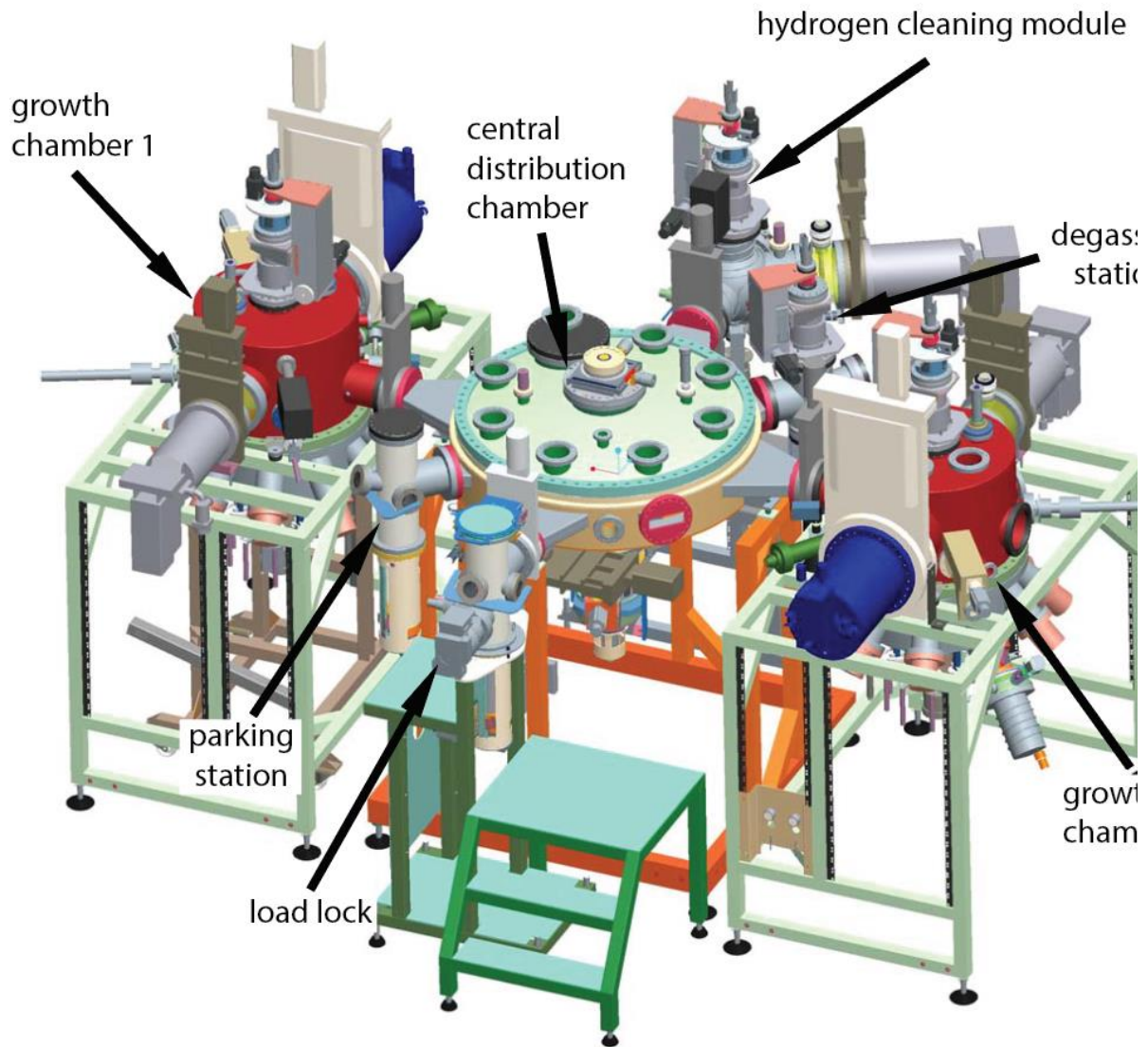


Figure 2-5. A schematic view of DCA P600 dual chamber system. The main parts of the machine including the load lock, parking station, growth chamber, degassing station, hydrogen cleaning module, central distribution chamber and the two growth chambers are highlighted.

## 2.2 Characterization Techniques

### 2.2.1 Electron Microscopy and Electron Spectroscopy

Electron microscopy and electron spectroscopy are some of the most used characterization techniques in materials science and engineering. These techniques include scanning electron microscopy (SEM), (scanning) transmission electron microscopy (S-TEM), energy dispersive X-ray spectroscopy (EDX), electron energy loss spectroscopy (EELS), cathodoluminescence (CL) and more. Collectively, these techniques offer fast morphological characterization (by SEM), crystalline quality characterization (TEM/ STEM), compositional characterization (core-loss STEM EELS, STEM EDX, SEM EDX) and

study of the functional properties (CL, low-loss EELS) with high to very high magnifications and resolutions.

An advantage of electron microscopy techniques is that the wavelength of the electrons can be readily changed by the acceleration applied to them. Furthermore, electrons normally have lower wavelengths than light. According to Rayleigh criteria, the diffraction-limited resolution is inversely proportional to the wavelength, so lowering the wavelength will result in images with higher resolutions (159). For comparison, modern electron microscopy offers wavelengths in the order of a few picometers as opposed to the wavelength of several hundreds of nanometers in visible light. At extremely low wavelengths, however, the resolution is limited by electron beam instability and lens aberrations (160).

There are different mechanisms for electron-matter interaction<sup>3</sup>, which are schematically shown in Figure 2-6, enabling various types of electron microscopy and spectroscopy. These interactions can be split into two main categories of elastic and inelastic scattering. In elastic scattering, the momentum magnitude (and thus the kinetic energy) of the electrons are conserved but the direction of wave vectors changes. This type of scattering occurs due to the Coulomb interaction of electrons and the atomic nuclei (161). The nuclei contain a high density of electric charge, causing the area in its vicinity to have strong electric field. The electrons passing that are close enough to the nuclei are greatly affected by this electric field and undergo deflection with a large angle. This is called Rutherford scattering and is shown in Figure 2-7(a). The Rutherford scattering angle depends on the charge of the nuclei and is used in High-angle annular dark-field (HAADF) imaging. If the deflection angle is more than 90°, the electrons are said to be backscattered. In these cases, these electrons can exit the sample from the same surface they entered. Backscattered electrons are captured and used in SEM to gain information about the nuclei and phase differences.

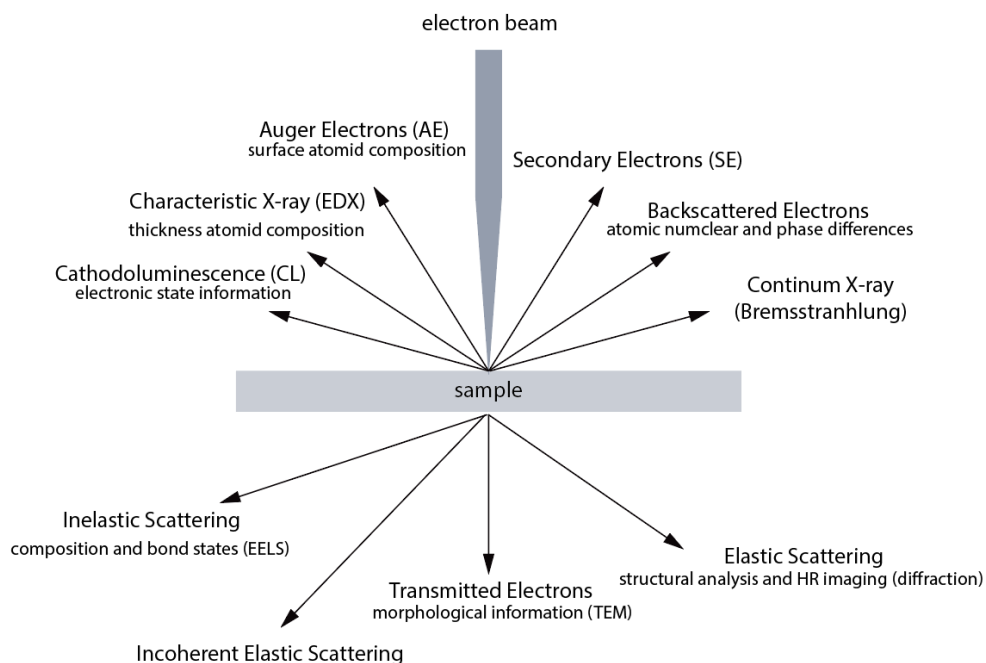


Figure 2-6. Different physical electron-matter interaction mechanisms used in electron microscopy and spectroscopy.

<sup>3</sup> The descriptions in this section are mostly adopted from reference (161).

Most of the electrons traveling through the sample, however, pass further away from the nuclei. As the electric field is inversely proportional to the square of distance from the nuclei, they experience weaker forces and thus are scattered at low angles. In domains with irregular arrangement of atoms, such as amorphous solids and gases, each nucleus scatters the incoming electrons independently. However, in a crystalline solid, the interference between the periodic electric potentials of the nuclei and the incoming electron waves make the continuous scattering distributions to collapse into discrete points whose angles depend on the atomic spacings. In this case, the elastic scattering is called (Bragg) diffraction and is widely used in transmission electron microscopy to study the crystalline structure of the solids.

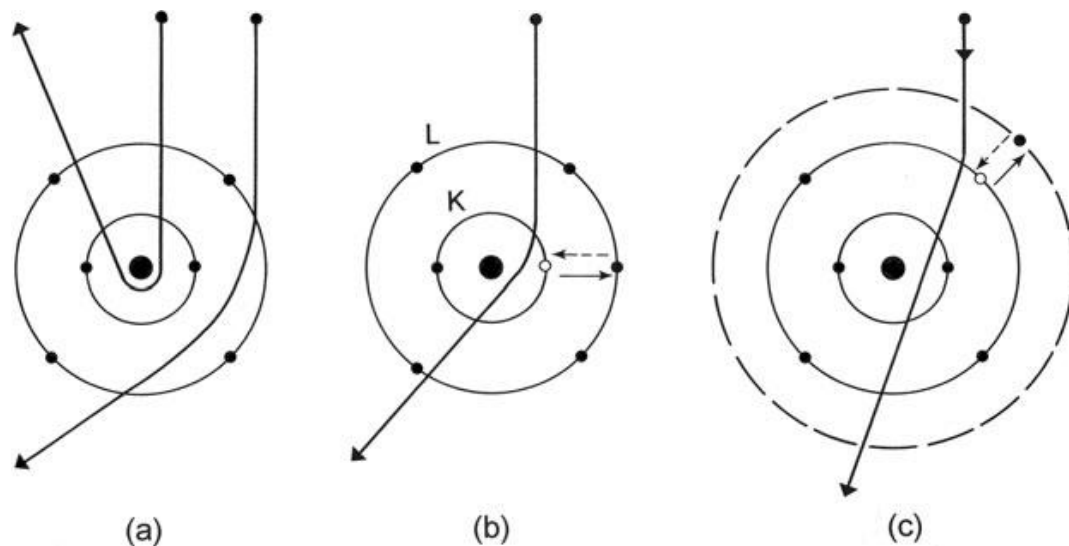


Figure 2-7. A view of electron scattering by a single atom (carbon). (a) Elastic scattering is caused by Coulomb attraction by the nucleus. Inelastic scattering results from Coulomb repulsion by (b) inner-, or (c) outer-shell electrons, which are excited to a higher energy state. The reverse transitions (de-excitation) are shown by *broken arrows*. These figures and their caption are taken from (161) with permission © Springer.

The Coulomb interaction of the electron beam and the atomic nuclei could also be inelastic. This happens when the deceleration of passing electrons by the nuclei causes X-ray emission which can have any energy less than the incident beam energy. The spectrum for this type of emission thus appear continuous and the process itself is called continuous x-ray, otherwise known as Bremsstrahlung emission (162).

Inelastic scattering is due to the Coulomb interaction between the passing electrons and the electronic cloud surrounding each nucleus. The interaction of fast-passing electrons with the inner-shell electrons in the solid is shown in Figure 2-7(b). The ground state of these inner-shell electrons in hundreds to thousands of electron volts below the Fermi level of the solid. Due to the existence of unoccupied electronic states above the Fermi levels, upward transition of the inner-shell electrons is possible given that the absorbed energy is similar or more than their binding energies. In this process, the passing electrons lose the same amount of energy, thus being scattered with small angles. This interaction leaves



the target atoms in an instable, excited state. De-excitation, then, can quickly happen, resulting in the downward transition of the outer-shell electrons with release of energy in the form of x-rays or another electron. The latter process is called Auger emission. Since the differences between energy levels are specific to each material, x-rays captured from this process are called characteristics x-rays and are used to perform chemical analysis of the samples in edx spectroscopy. It is to be noted, however, that for a meaningful chemical analysis, the continuous background caused by Bremsstrahlung emission should be removed from the edx spectrum. Figure 2-7(c) helps visualize emission process of characteristics x-rays.

In addition to this process, if the excited state has an energy higher than the vacuum level of the solid and the excited electron possesses high-enough energy, it can escape the solid and be emitted as secondary electron. This process happens at very low angles between 1 and 2 mrad for the energy of the incident electron beam in the range of 100 KeV. As a result of this process, CL radiation in visible range, energy dissipation in form of heat or ionization damage can occur.

Instead of the single-electron excitation described before, a collective inelastic scattering can occur between the outer-shell electrons and many solid nuclei. This results in oscillation of the valence electron densities is called plasmon resonance. The energy of this excitation is in the range of 5-30 eV for most solids. Low loss spectroscopy tries to record this energy and use it to characterize the electronic and band states of the sample. The plasmons quickly decay, releasing their energy in the form of heat or by creation of secondary electrons<sup>4</sup>.

For plasmon scattering, the mean free path of inelastic scattering is usually between 50 and 150 nm. If the sample thickness is more than this mean free path, plural scattering will have a pronounced effect on the overall processes, distorting the shape of the energy-loss spectrum. This results in thickness-dependency of the spectrum, which is not desirable for material characterization. However, the plural scattering peaks can be removed by established deconvolution algorithms.

Now, we focus on the structure of electron microscopes, which is schematically demonstrated in Figure 2-8. An important requirement for electron microscopy is implementation of high vacuum. This is to ensure that the electron beam is not scattered or lost some of its energy in the atmosphere of the microscope chamber before reaching the sample. Each microscope consists of four main parts: electron gun, condenser, objective and detectors (163,164), with various apertures and lenses being used to construct the condenser and objective sections. Electron gun, otherwise called cathode, is responsible for generation of a bright, stable and intense electron beam with the shape as close as possible to a point and a low energy dispersion. After emission from the gun, an electric field parallel to the optical axis of the beam acts on the electrons to accelerate them to their final kinetic energy,  $E$ . This field is generated through application of a potential difference between the cathode and an anode, which is a circular metallic plate with a hole in its center. It is to be noted that the anode absorbs around 99% of the electrons produced by the gun (165).

The condenser part is the illumination system of the microscope and is used to guide and focus the electron beam. In modern electron microscopy, the condenser starts with magnetic lenses C1 and C2 acting on the passing electrons by Lorentz force. These two lenses can collectively make beam crossover and

---

<sup>4</sup> Beside this bulk effect, surface plasmons can be created. These effects are, however, only pronounced for very thin samples or small particles.

focus the beam on the sample. For an electron with the velocity of  $\vec{v}$  passing from a magnetic field  $\vec{B}$ , the force applied to the electron is:

$$\vec{F} = -e(\vec{v} \times \vec{B})$$

where  $\times$  is outer product and  $-e$  is the charge of the electron. The force applied to the electron will therefore be perpendicular to both its velocity and the direction of the magnetic field of the lenses. Consequently,  $\vec{F}$  has no component in the direction of travel of electron beam and thus the magnitude of velocity parallel to the optical axis of the lens stays constant.

Beams exiting C2 go through condenser aperture. In general, apertures are metallic objects with holes in them that block the passing of electron beam except for through the hole. This gives an opportunity to control the beam size illuminated on or passed from the sample, convergence angle and the depth of focus and select specific diffraction points. In addition, the electrons further away from the center of the beam are more likely to suffer from spherical aberrations, a process that causes electrons passing from the periphery of the lenses unable to focus on the same point as the electrons passing from the center of the lens (165,166). Using apertures, therefore, will reduce the spherical aberrations and increase the resolution.

Scan coils are then employed to properly align the electron beam with respect to the optical axis of the microscope. The role of these coils in SEM and STEM is to scan the surface of the sample with concentrated, pointy beam, while in TEM they make the electron beam they produce parallel beams on the area of interest.

The combined effect of C1, C2 and scanning coils can make the electron beams non-circular, which introduces aberration and lowers the resolution. Condenser stigmators are used to correct for this effect before the entrance to the objective section.

The objective section of the microscope is used to form the image. In general, objective lenses are the strongest lenses in the microscope. In SEMs, the samples are placed after the objective lens, while in TEM and STEM, they are placed within the objective system itself. This is called immersion configuration and uses magnetic lenses to effectively form the images. The pre and post- sample components of the objective system are used to achieve different goals in TEM and STEM. In TEM, the pre-sample section, called upper objective lens, is used to ensure that the beams illuminated on the sample are parallel, while in STEM it is used to make a pointy probe beam on the sample. The post-sample parts in TEM, called lower objective lens, forms a crossover at its back focal plane. This is the lens that is used to magnify the image. In stem, the post-sample part of objective system is called transfer lens, as shown in Figure 2-8 and is employed for image alignment with the detectors. In both TEM and STEM configurations, objective stigmators are used to correct for aberrations introduced in the objective system.

In SEM and TEM, object apertures are also used. The objective aperture diameter in TEM determines the scattering angle of the electrons leaving the sample, which in turn dictates the number of diffracted beams used to form the image (167). Lower objective apertures can reduce image delocalization, but result in lower image intensities and contrasts. After the objective aperture, there are intermediate and projection lenses in TEM, which help construct the image on the detector itself.

An important function of the objective aperture in TEM/ STEM is to change between the bright field (BF) and dark field (DF) modes. Different parts of the specimen have different affinity for absorbing or scattering the electrons based on factors such as composition, thickness and crystalline orientation with

respect to the electron beam. In BF imaging, the non-diffracted beam, often called direct beam, is transmitted from the specimen is used to form the image. Therefore, the parts that are less absorbent and diffracting appear the brightest. In DF imaging, on the other hand, the diffracted beams are chosen to form the image, and the direct beam is blocked, making the most diffracting parts of the specimen to be the brightest. This makes DF images very sensitive to the presence of defects in the structure. Figure 2-9 (a) and (b) provide an schematic view of the switching mechanism between the BF and DF imaging, while example BF and DF images for identical area of interest on a tissue paper under are provided in Figure 2-9 (c) and (d), respectively.

Finally, detectors are used to capture the images or record the spectrum. Different detectors are used to address the different electron-matter interaction mechanisms shown in Figure 2-6. These detectors are based on either charge-couple devices (CCDs) or complementary metal-oxide-semiconductor (CMOS) (168). Both these technologies use photo diodes to convert photos to electrons. In a CCD, the charge is transferred between neighboring pixels and the read-out happens after. Binning is used to minimize the read-out noise. In CMOS, on the other hand, the charge is immediately converted to voltage. This allows for high frame recording and low electronic noise.

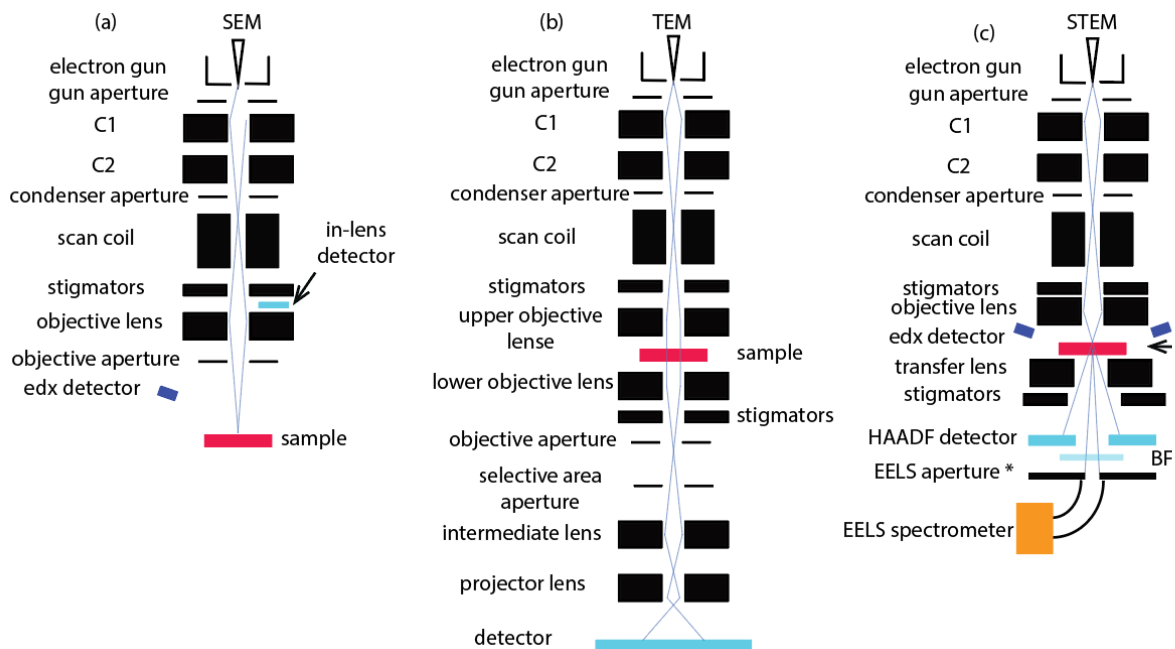


Figure 2-8: schematic view of different electron microscopy configurations. (a): SEM, (b): TEM, (c): STEM

In TEM, the detector is placed on the optical axis of the microscope at the end of the column. In STEM, however, some adjustment to this configuration is needed. The BF detector is indeed located on the optical axis of STEM, but using it will block the entrance to EELS spectrometer. In practice, the BF detector is removable. While acquiring the EELS spectra, concurrent image recording can happen using HAADF detectors. EDX detectors are placed above the sample with a sharp angle in both STEM and SEM configurations.

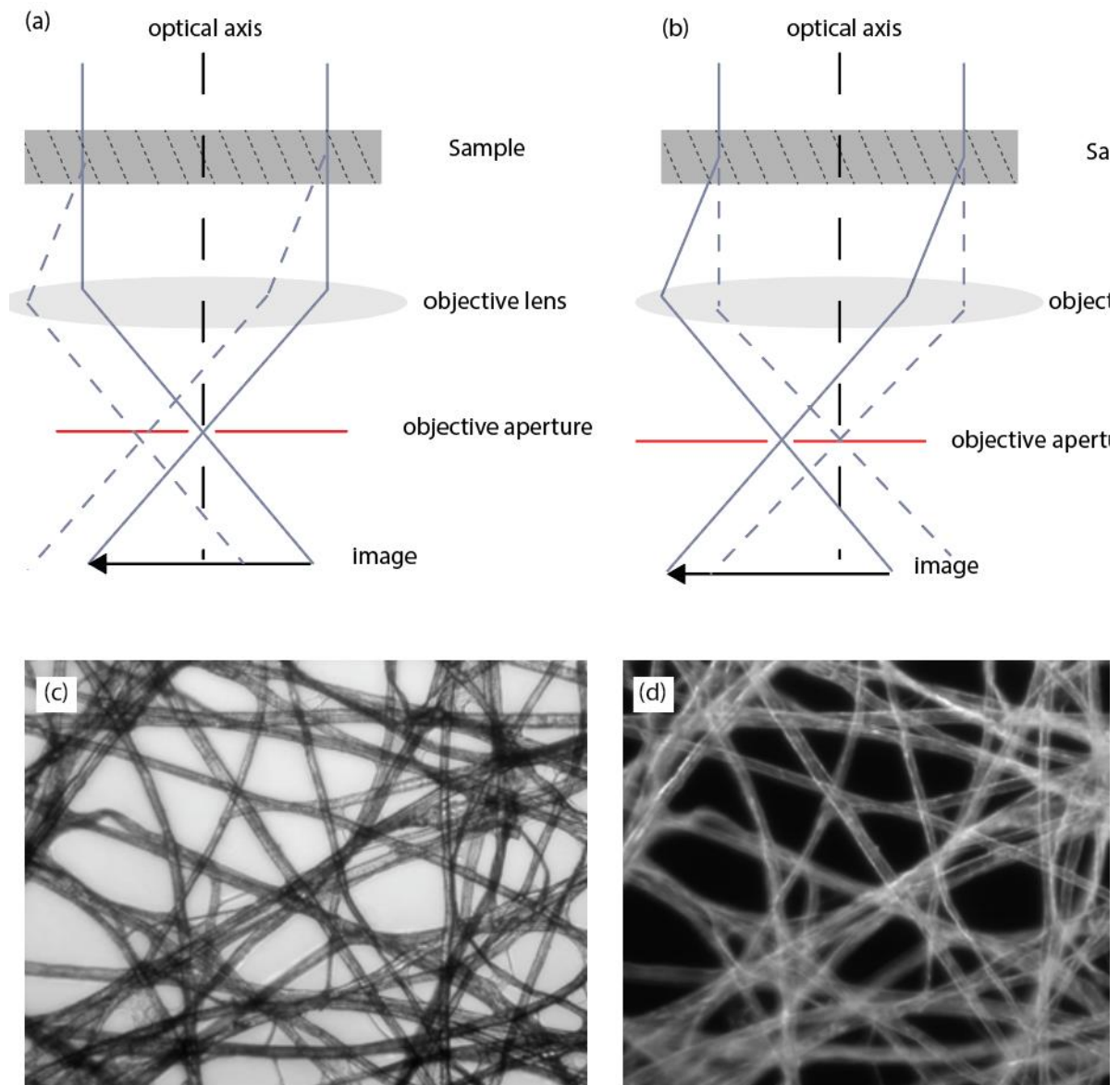


Figure 2-9. (a) BF image formation mechanism, in which the electron beams transmitted from the sample without scattering are passed through the objective lens and are used for image formation. These beams meet on the optical axis of the microscope (b): DF image formation mechanism, in which the diffracted electron beams from the sample are passed through the objective lens and used for image formation BF. These beams meet off the optical axis of the microscope. (c) and (d): BF and DF images of a tissue paper under TEM. Image author: Zephyris (Richard Wheeler, Wikipedia), used under Creative Commons Attribution-Share Alike 4.0 International license.

The inclusion of multiple lenses in the structure of electron microscopes introduces aberrations, which limit the image resolution. Indeed, the resolution of electron microscopes is far from the values diffraction-limited predictions according to Bragg's law due to these aberrations (169). This is caused by the imperfections in the performance of the lenses in the microscope dispersions in electron source. An ideal lens will focus all the beams parallel to its optical axis of a single point, as shown in Figure 2-10 (a). The main two types of aberrations in electron microscope are chromatic aberration and spherical aberration. Chromatic aberration, demonstrated in Figure 2-10 (b), refers to the failure of the

lens to focus the electrons with different energies <sup>5</sup> on the same point on the optical axis (170). Spherical aberration, on the other hand, refers to the situation in which the focal length of the beams passing from the lens depends on their distance from its optical axis (171), as shown in Figure 2-10 (c). In the absence of chromatic aberration, the point resolution of a lens is proportional to  $C_s^{0.25} \lambda^{0.75}$ , in which  $C_s$  and  $\lambda$  are the coefficient of spherical aberration and the wavelength, respectively. Therefore, for a constant wavelength, reducing the spherical aberration will result in an improvement in the point resolution.

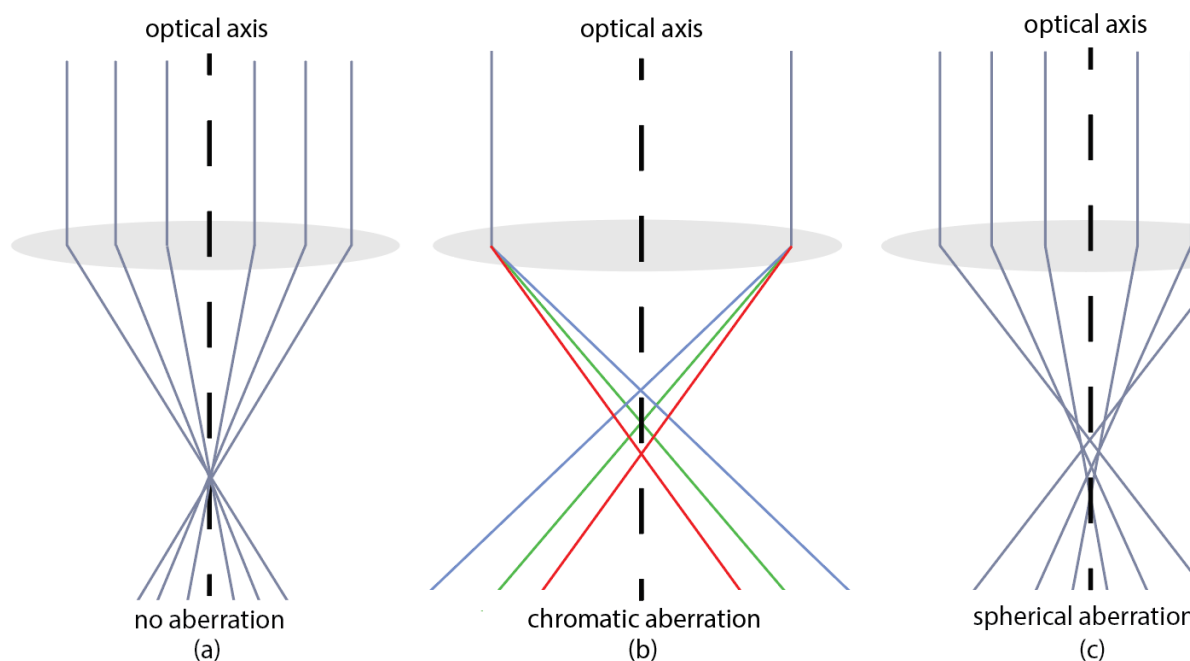


Figure 2-10. (a) : an ideal lens with no aberration. All the rays passing from the lens parallel to its optical axis are focused on the same spot. (b): the effect of chromatic aberration on the performance of a lens. Rays with different energies are focused on different points. (c): the effect of spherical aberrations on rays exiting lenses. The focal length is a function of the distance of the ray from the optical axis of the microscope.

For the lenses designed with rotational symmetry, positive and spherical aberrations are unavoidable (172). However, the use of non-round, multi-pole lenses that do not have rotational symmetry, first proposed in 1947 (173), generates negative  $C_s$  coefficient. These negative values of  $C_s$  can be used to cancel out the positive  $C_s$  of round lenses. The special sets of lenses that are dedicated to reduce the aberrations are called correctors. The TEM and STEM use different positions for implementation of correctors: in TEM, the correctors are placed after lower objective lens and are called image correctors. In STEM, however, the correctors are implemented before the objective lens and are called prob collectors. It is to be note that the introduction of aberration correction in electron microscopy has resulted in a pronounced leap in the performance and resolution of electron microscopes, as demonstrated by the trend in Figure 2-11. Here, the advent of aberration corrected electron microscopy in post 2000s, marked in red, shows a significant jump in the resolution over the previous electron microscopy technologies marked in green.

<sup>5</sup> Despite all the effort put, slight variation of the energy of electrons is present in the electron microscope. This is because most of the time, the beam as generated by the gun is not monochromated. Furthermore, energy loss might happen due to the interaction of the electrons with the sample and the microscope components.

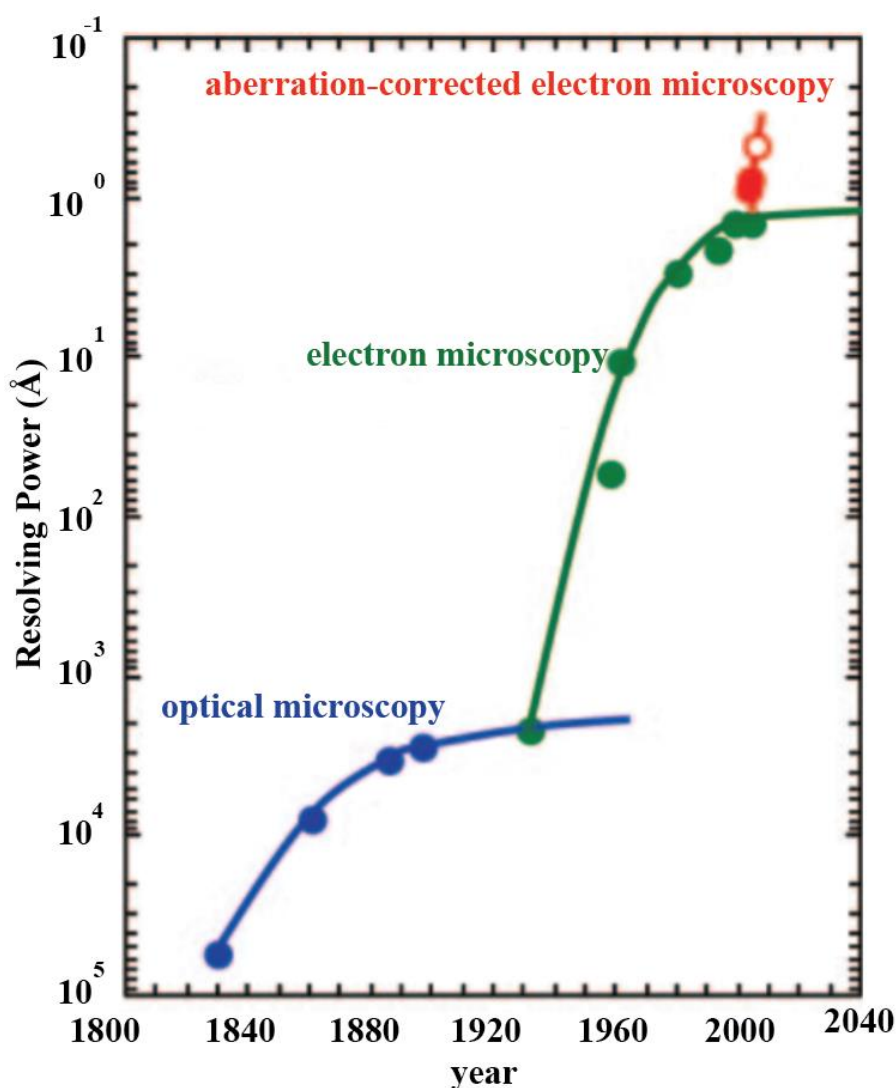


Figure 2-11. The trend for minimum resolving power of microscopes in Å for different years since mid-18 century. The introduction of electron microscopy in the first half of 20 century, shown in green, has been the major factor in improving the resolution of microscopy. The advent of aberration correctors in early 20 century has further pushed the performance of electron microscopy. This image is taken from reference (174) with some modification and permission © Springer.

For an in-depth review of the different components of an electron microscope, one can check references (163,165).

In addition to the structural differences between SEM and TEM/ STEM, there is a significant difference in the accelerations ranges that SEMs and TEMs/ STEMs employ. For most applications, SEMs are used in 0-10 KeV energy ranges, while the TEMs normally used with a few hundreds of KeVs<sup>6</sup>. At these energies, electrons have very high speeds that can approach the speed of light. Thus, it is essential to consider relativistic effects when working with such high accelerations. Table 2-1 demonstrates the increased importance of the relativistic effects and the failing of classical considerations at energies.

<sup>6</sup> For studying 2D materials such as graphene and  $MoS_2$ , TEMs/ STEMs operate in lower energy ranges, such as 20-80 KeV (175).

The last column of this table lists the calculated energy neglecting the relativistic effect, which uses the resting electron mass without considering the increased effective mass of the electrons at higher speed.

Table 2-1: the demonstration of relativistic effects on the speed and the mass of electrons.  $E$  represent the electron beam energy,  $\gamma = m^*/m_0$  where  $m^*$  and  $m_0$  are the effective and resting electron masses,  $v$  and  $c$  are the speed of electrons and light, respectively. The last column represents the classical calculations of kinetic energy, showing how it fails for electrons traveling at speeds close to the speed of light. This table is taken from (165) with permission © Springer.

$E$ (KeV)	$\gamma$	$v/c$	$m_0 v^2/2$ (KeV)
60	1.12	0.45	51
100	1.2	0.55	77
200	1.39	0.70	124
300	1.59	0.78	154
1000	2.96	0.94	226

It is to be noted that at first approximation, increasing the voltage can increase the resolution. However, this increased acceleration can have adverse side effects that negatively impact the resolution. For instance, the increased interaction volume in SEM will result in lowering of resolution and losing surface details (167). This is the reason the acceleration is kept in much lower ranges in SEM compared to TEM and STEM, where the low thickness of the sample limits the interaction volume and can prevent from this resolution degradation at high voltages. This low thickness in TEM/ STEM images is to increase the resolution and lower plural scattering phenomena discusses earlier. However, it adds extra steps to sample preparation for TEM/ STEM imaging compared to SEM, where most conductive samples can be readily inserted into the microscope chamber and be images immediately. The sample loading in TEM/ STEM is done via TEM grids, which are small circular pieces that have some parts of the specimen attached to them. Often, grid preparation for TEM/ STEM can be done by mechanical polishing or focused ion beam (FIB)<sup>7</sup>, which is the technique used in this thesis and will be discussed in the next section.

## 2.2.2 Focused Ion Beam (FIB)

FIB is used to cut a piece of sample, called lamella, attach it to a TEM grid and thin it down so that it becomes suitable to TEM/ STEM imaging.

A FIB machine is composed of four main parts: an SEM column, an ion gun, a source for material deposition and a manipulator. The SEM part of is used to monitor the operations in real-time and adjust the process. The ion gun generates a beam of ions onto the sample by applying a strong electromagnetic field on positively charged liquid metal ions. The purpose of this ion beam is two-fold: first, it is used

---

<sup>7</sup> For NW and nanoparticles, the grid preparation can be done by simply scaping the grid on the sample.

to cut the specimen and thin down the lamella. In addition, it is used to accelerate the deposition/welding process when used in conjunction with the deposition gas. The deposition source, which is in form of a gas, is used to provide a layer on the lamella to protect the sample from the beam damage caused by the ion beam and also attach the lamellas to the manipulator/ TEM grid. The manipulator is used to transfer the lamella from the sample to the grid. The ion and deposition sources in this thesis have been gallium and carbon, while the manipulator has been made from tungsten. The ion and electron beams are at a  $54^\circ$  angle configuration with respect to each other.

The standard FIB procedure is as follows: first, microscope alignment is done and the sample is moved to the eucentric point of electron and ion beams. Then, a carbon layer is deposited on the sample surface by the help of electron and ion beams, Figure 2-12 (a). This protective layer specifies the lamella area. The area around the lamella is cut using the ion beam, Figure 2-12 (b), and then the manipulator is attached to one side of the lamella, Figure 2-12 (c). Next, the lamella is released from the sample, Figure 2-12 (d), and attached to the TEM lamella, Figure 2-12 (e). Finally, this lamella is gradually thinned down to the desired thickness, Figure 2-12 (f).

A common challenge with FIB is amorphization of the lamellas, which renders them worthless for studying the crystalline structure of the sample. This happens because, as the lamella is gradually thinned down, not much material is left on it to act as thermal sink. The excess heat provided by the FIB gun therefore can amorphize the structure. In order to prevent this, the fibbing current is gradually reduced. In addition to being too prone to amorphization, the lamellas that get too thin are also structurally fragile. In practice, the lamella is thinned down to 100 - 200 nm. This is thin enough to enable atomic imaging and prevent plural scattering and is thick enough to prevent from amorphization and give structural robustness.

Due to the choice of ion and deposition materials, care must be taken when using fibbed lamella for chemical analysis by EDX. For instance, gallium ions will be embedded into the lamella during the fibbing process, introducing chemical artifacts that make the compositional analysis unreliable when the specimen has gallium as its constituting elements. It is therefore recommended to use other ion sources in such cases.



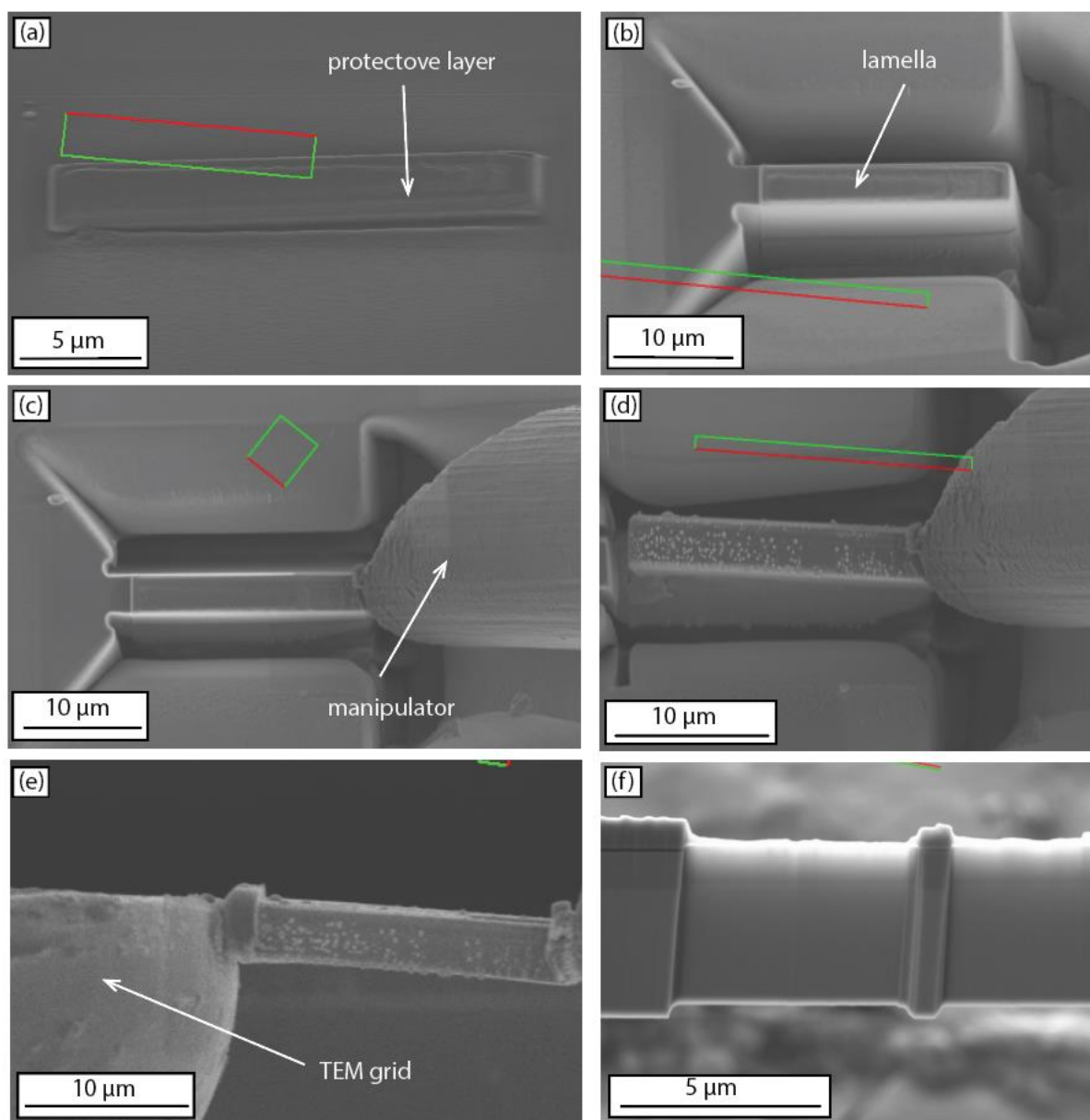


Figure 2-12. (a): deposition of a carbon protective layer. (b) cutting the area around the lamella. (c): attaching the manipulator to the lamella. (d) releasing the lamella from the substrate. (e): attaching the lamella to the TME grid. (f) thinning down the lamella. Images (a) to (e) are taken from the top view, while image (f) is taken from the side view.

### 2.2.3 Raman Spectroscopy

Raman spectroscopy is a non-destructive technique widely used for identification of molecular structures and compounds and can be used to characterize oxides, ceramics, polymers, nanomaterials, powders, glasses, bio-materials and semiconductors (175). It offers a non-destructive method for a quick phase identification and crystalline quality assessment. In Raman spectroscopy, the probing beam is a laser light. The Raman effect is used to characterize the sample. A quantum- mechanical description of Raman effect is as follows: when a phonon interacts with a crystal lattice or a molecule, it can promote

that lattice or molecule to a virtual, higher energy state. There could be multiple outcomes for such high-energy state, one of which involves relaxation to a vibrational energy level <sup>8</sup>. The difference in the energy of this state and the original state before excitation can be released by photon emission. The frequencies of these photons, often called Raman shifts, are used for the characterization of the sample (176). The discovery of the Raman effect by Chandrasekhara Venkata Raman won him the Nobel Prize in Physics in 1930 (177).

When the frequency of the incident light is higher than the frequency of the scattered light, Stokes Raman shift is said to have happened. In the reverse cases in which the frequency of the incident light is lower than the scattered light, anti-Stokes effect has occurred. Since Stokes shift involved the transitions from higher to lower energy levels, they are more likely. Consequently, the Stokes lines are more intense in a Raman spectrum. Therefore, in modern conventional Raman spectroscopy, only Stokes lines are measured, while the anti-Stokes lines are measured in fluorescent samples as fluorescence causes interference with Stokes lines (178). The scattered photons that have energies identical to the incident photons are said to have undergone Rayleigh scattering. The magnitude of Raman shift does not depend on the wavelength of the incident light. However, the intensity of the Raman scattering is highly dependent on the incident wavelength, so the magnitude of peaks in Raman spectra will change as a function of laser wavelength (177).

Beside the chemical composition, Raman spectra can be affected by a few other factors such as crystal symmetry. For molecular Raman spectroscopy, the Raman spectra consists of narrow bands, the widths of which depend on the intensity of chemical interactions between the molecules: strong interactions will broaden the Raman peaks (177).

The Raman spectra of the same solid compound in crystalline and amorphous configurations will be different due to the presence or absence of long and small-range spatial orders and translational symmetry. Amorphous solids can be considered as a collection of units with identical chemical formula, but varying bond lengths and angles. The distribution in the bond lengths and angles causes a distribution in the vibrational states, and consequently, Raman shifts, which in turn broadens the Raman peaks (177). For monocrystalline solids, these distributions collapse into single values due to the presence of long-range order and translational symmetry. Polycrystalline and nanocrystalline solids lay in between the two extreme cases of amorphous and monocrystalline solids. Figure 2-13 demonstrates this fact for amorphous and polycrystalline  $Zn_3P_2$ . The red and black curves the Raman spectra of an amorphous and crystalline film for measurements done at room temperature. The peaks in the spectra of the amorphous film are broader compared to those in the spectra of the crystalline film. Indeed, some of the peaks for the amorphous film are merged and form broad shoulders. This is the case for the families of peaks in  $50 - 100\text{ cm}^{-1}$ ,  $120 - 210\text{ cm}^{-1}$  and  $270 - 350\text{ cm}^{-1}$  ranges. Cryogenic Raman measurements and theoretical modeling have revealed that the low-frequency region with Raman Shift  $< 210\text{ cm}^{-1}$  and high-frequency region with Raman shifts  $> 225\text{ cm}^{-1}$  are dominated by  $Zn P$  sub-lattices, respectively, while a phonon gap in  $210 - 225\text{ cm}^{-1}$  exist (93).

---

<sup>8</sup> The probability of Raman scattering is very low: approximately 1 in every 10 million laser photons undergoes this phenomenon (176)

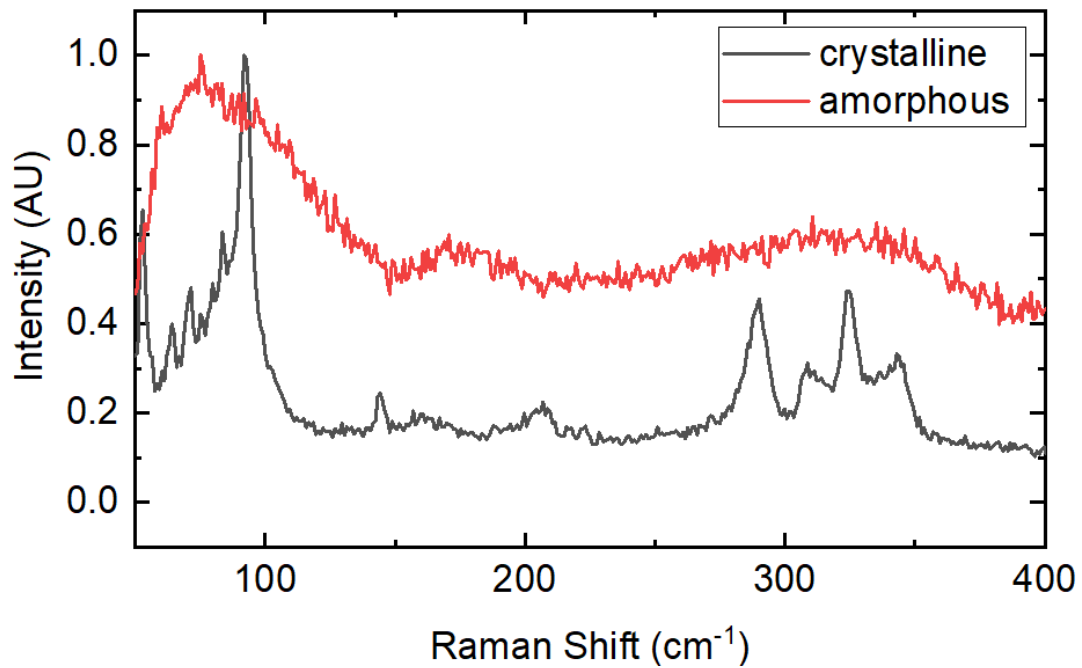


Figure 2-13. The comparison of Raman spectra for amorphous and polycrystalline  $Zn_3P_2$  thin films measured with identical parameters.

A Raman spectrometer has these components, as shown in Figure 2-14 : a monochromated laser source, a filter to discriminate the Stokes photons from anti-Stokes and Raleigh photons. A diffraction grating will then bend the Raman shifted light according to the wavelength of the photons. Finally, a detector is used to record the signal. A few other parts such as mirrors and lenses are used to guide the laser and scattered light.

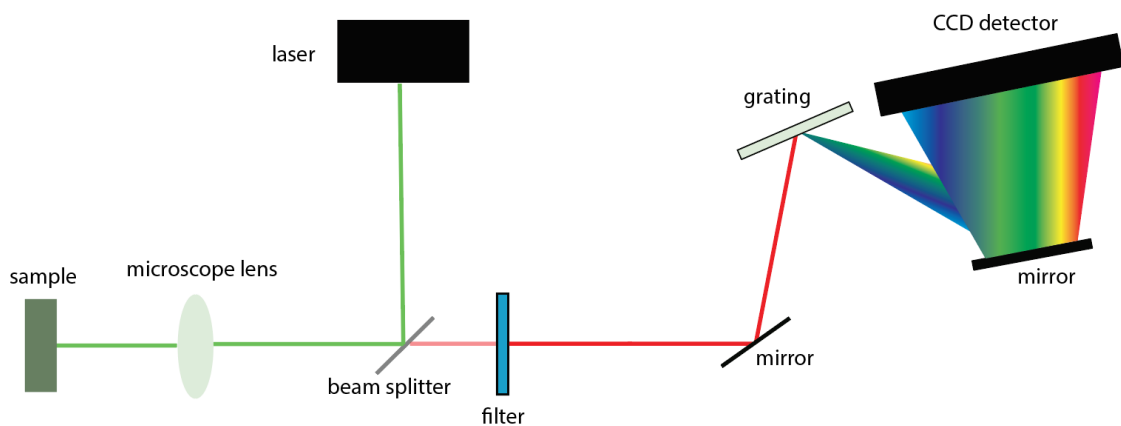


Figure 2-14. Schematic view of basic structure of a Raman setup.

## 2.2.4 XRD

XRD is one of the most common structural characterization methods in materials science due to its great versatility, ease of sample preparation and relative quickness.

The principles of XRD were discovered in 1912 when Max von Laue discovered that crystalline materials can effectively act as diffraction gratings for x-rays, which won him a Nobel Prize in Physics in 1914 (179). The radiant X-ray can have constructive interference with the sample lattice according to Bragg's law of diffraction,  $n\lambda = 2d\sin\theta$ , where  $\lambda$  and  $\theta$  are the X-ray wavelength and the diffraction angle,  $d$  is the atomic spacing and  $n$  is an integer and is often called the order of reflection (180). Given that the  $\lambda$  is a known quantity, measuring  $\theta$  can lead to calculation of  $d$ . Since different atomic planes have different spacings, diffraction often occurs in multiple angles, the combination of which is unique to each material. The position of these peaks then can be compared to the values in XRD databases for phase identification.

XRD can be performed with different configurations for the X-ray source and detector. In grazing incident XRD (GIXRD), Figure 2-15(a), the source is kept at a very low incident angle,  $\beta$  with respect to the sample and the detector is rotated around the sample. The intensity of diffraction is recorded for each  $\theta$  angle. The very low incident angle makes the penetration depth very low in this configuration, rendering it very sensitive to the surface. In Gonio configuration, otherwise known as theta-2theta scan and shown in Figure 2-15(b), the source and detector have identical angles with respect to the substrate and are moved at the same time. This configuration can only detect planes that are parallel to the sample surface, so it is ideal for characterizing the growth direction (181). However, for thin films samples, often the signature of the substrate is also observed in the diffraction pattern due to the high penetration depth of the X-ray radiation.

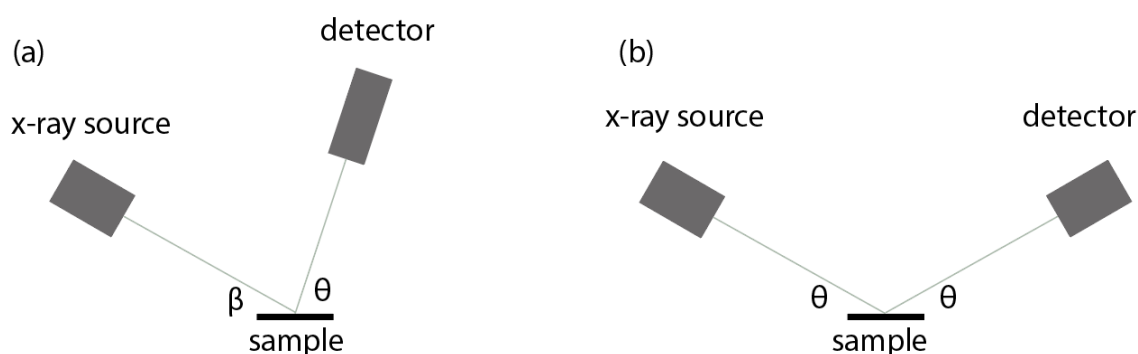


Figure 2-15. (a): GIXRD configuration in which the source is kept at a constant angle and the detector is rotated around the sample. (b): Gonio XRD in which the source and detector have identical angles with respect to the sample and are moved at the same time.

For phase identification, XRD is often performed on samples that are ground into powders. Different powder particles will have different orientation with respect to the incident x-ray, making it possible to observe all the possible diffractions in the detection range. However, in this thesis, the samples have been of known phases and the interest have been to check the crystalline quality and the growth orientation. The measurements on the as-grown thin films are realized in Gonio configuration. Figure 2-16 shows the XRD pattern for a polycrystalline and a monocrystalline  $Zn_3P_2$  film grown on  $InP(001)$  substrate. Both these patterns feature a prominent  $InP(200)$  peak denoted by light green. All

the other peaks labeled on this figure belong to  $Zn_3P_2$ <sup>9</sup>. The most intense peak of  $Zn_3P_2$  in both cases is (004). However, there is a pronounced difference in the intensity of this peak between the two samples as the peak is much stronger for the monocrystalline thin film. The only other peaks belonging to  $Zn_3P_2$  on the monocrystalline thin film are (002) and (006), which, in conjunction with the strong (004) peak indicate that the growth direction for this film is [001]. This fact and the monocrystalline nature of this thin film have also been independently confirmed by TEM. There are numerous higher-index peaks in 30° – 40 ° range for the polycrystalline film, which are absent on the monocrystalline film. The presence of these peaks is a signature of the polycrystalline structure for this sample.

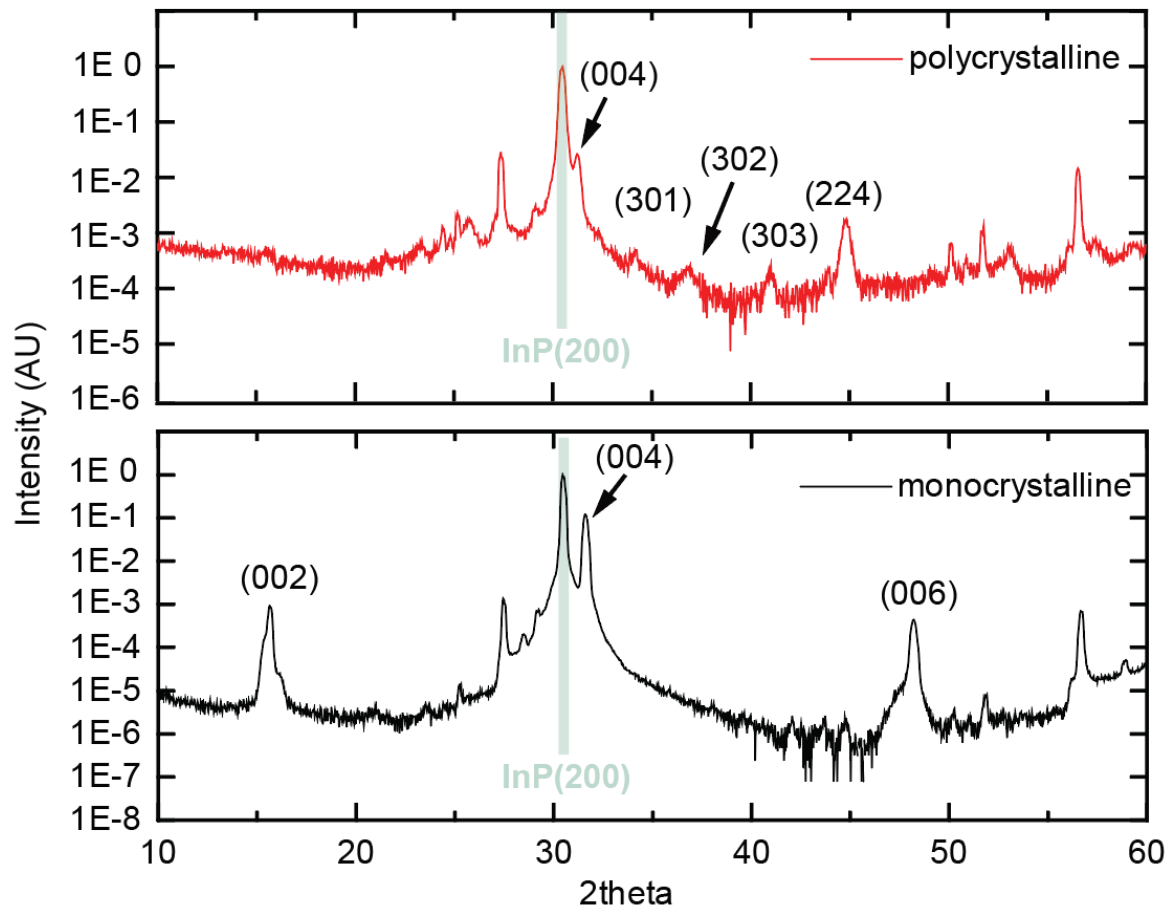


Figure 2-16. The comparison of the XRD pattern of a polycrystalline (top) and a monocrystalline (bottom) thin film. The monocrystalline film only exhibits peaks belonging to [001] direction, which is in contrast to the observation of multiple high-index peaks between 30° and 40 ° on the polycrystalline film.

Due to the inherent reliance on x-rays, extra care must be taken when performing XRD to minimize the risks. Modern XRD machines have an enclosure around them, ensuring the safety of the operators.

<sup>9</sup> The other peaks not labeled belong to the substrate

## 3: Results & Discussion

In this chapter, the main results of the thesis are provided. These results are composed of the findings on the effect of droplet liquid ordering at the interface with the NW on the properties of self-catalyzed *GaAs* NWs, and the growth optimization of  $Zn_3P_2$  thin films on *InP*(100) substrate. The results on  $Zn_3P_2$  thin films have been submitted for publication and are accepted with minor revision at the time of this writing, while the findings on the liquid ordering are published in an open-access and peer-reviewed publication. First, a short description of the work done is provided for each of articles.

### 3.1 Growth optimization of $Zn_3P_2$ thin films on *InP* (001) substrate

Despite its potential, the mainstream adaptation of  $Zn_3P_2$  for cheap and scalable photovoltaic applications is hindered by the inherent difficulties in the growth of high-quality  $Zn_3P_2$  thin films, which were listed in the first chapter of this thesis. In short, the unit cell of  $Zn_3P_2$  is very large, making it difficult to find a lattice-matched substrate for epitaxial growth. In addition, the very large thermal expansion coefficient of this material makes thin films of  $Zn_3P_2$  grown at high temperature to crack upon cooling down after the growth. In practice, reports on the growth of monocrystalline thin films of  $Zn_3P_2$  have been rare and limited to 150 nm in thickness, with higher thicknesses resulting in strain relaxation through cracking and deterioration of functional properties such as carrier mobility and concentration (50). In addition, doping control in  $Zn_3P_2$  has proven challenging due to the tendency of *P* atoms to get incorporated into the empty sites in the lattice of  $Zn_3P_2$ , causing intrinsic p-doping. In addition, it is observed that the doping behavior of this material is highly dependent on the concentration of its defect states. In this work, we have focused on improving the crystalline quality of  $Zn_3P_2$  and demonstrated a method for reproducible growth of monocrystalline  $Zn_3P_2$  thin films up to the thickness of 1  $\mu m$ . In addition to improving properties such as carrier life time and mobility, this can be helpful in order to control the doping behavior of this material.

The process for the growth of thin films in this work are as followed: first, the *InP*(001) substrates undergo two steps of degassing at 150 °C and 300 °C, each of which have the duration of two hours. Then, a third degassing stage at 580 °C is implemented to remove the native oxides from the substrate. The duration of this step is variable and its effects are discussed below. The growth is then performed on the degassed substrates.

First, the effects growth parameters, such as the ratio between  $P_2$  and *Zn* fluxes (*V/II* ratio) and growth temperature on the thin film type is studied by Raman spectroscopy and SEM. It is observed that an increase in *V/II* ratio and growth temperature results in the growth of amorphous films, in agreement with previous observations of growth on graphene (182). On the other hand, reduction in the growth temperature and *V/II* ratio results in polycrystalline films with increased number of grains.

To study the effects increasing the duration of degassing time at 580 °C, a series of growths with degassing times varying between 10 min and 75 min is conducted. The results indicate that with a fixed growth temperature of  $T = 245\text{ }^\circ\text{C}$ ,  $V/II = 0.72$  and  $P = 5.81 \times 10^{-7}\text{ torr}$ , for degassing times  $\geq 30$  min, the  $Zn_3P_2$  thin films grown on both n-doped and p-doped *InP*(001) substrates adopt monocrystalline configurations. The n-doped and p-doped substrates have been used to see if the process for the growth of monocrystalline films depend on the substrate doping type.

Electron microscopy is used to shed light on the structural differences of poly and monocrystalline thin films and in particular of the initial stages of growth as elucidated by the characteristics of the interface with the substrate. As expected, the monocrystalline films exhibit a clean and defect-free structure. Interestingly, the interface between the substrate and the film is sharp, and transition from  $InP$  to  $Zn_3P_2$  occurs through the formation of a mixed  $In/Zn$  monolayer at the interface. The growth direction of the monocrystalline films is determined to be (001) by XRD and TEM. On the other hand, polycrystalline films demonstrate a columnar and granular structure with many small grains forming at the interface with the substrate, which gradually merge to form bigger grains as the growth continues. Interestingly, the polycrystalline thin films exhibit a blurred interface with the thickness of  $\sim 15$  nm, which prevents the continuous epitaxial relationship between the substrate and the thin film. We attribute this to the cause of polycrystallinity. Furthermore, core-loss EELS studies reveal that, unlike the interface of monocrystalline films, the interface of polycrystalline films hosts oxygen atoms. Therefore, the increase in the degassing time at 580 °C promotes the monocrystallinity by effectively removing the native oxide that is present on the substrate. The careful engineering of the atomic order at the interface is therefore deemed fundamentally important for controlling the crystalline quality of  $Zn_3P_2$  thin films.

The structural differences between amorphous, polycrystalline and monocrystalline samples are also investigated by XRD. As expected,  $Zn_3P_2$  peaks are completely absent from the XRD pattern of amorphous films. Polycrystalline films, on the other hand, exhibit (004) peak in addition to multiple other higher order peaks such as (302), (303) and (224). On the other hand, the monocrystalline film only exhibits (002), (004) and (006) peaks, further confirming that these films indeed grow in [001] direction.

Finally, low-temperature PL is used to investigate the optical properties of  $Zn_3P_2$  thin films. It is found that the emission properties of the polycrystalline samples strongly depend on the growth parameters. Defect-related emissions at few dozen  $meV$  below 1.4 eV are observed for the polycrystalline films. In addition to the variation in the optical emission between different polycrystalline samples, the peak positions and intensities could also slightly change on the same sample depending on the probing position, which could be due to the local variation in the defect types and densities. On the other hand, the monocrystalline samples exhibit a homogenous emission over the whole area of the film. In addition to the substrate emission at 1.43 eV, two peaks at 1.3 eV and 1.52 eV are also observed, the latter of which is consistent with the direct bandgap emission of  $Zn_3P_2$ . We think these initial results open an avenue to use this material in photovoltaic devices and the growth mechanism could be relevant for other materials systems.

The results of this work have been submitted for publication in a peer-reviewed journal and are accepted with minor revision at the time of this writing.

Additional data on the optical and electrical properties of these thin films, still under preparation for a publication, can be found in the appendix.





## The path towards 1 $\mu\text{m}$ monocrystalline $\text{Zn}_3\text{P}_2$ films on $\text{InP}$ : substrate preparation, growth conditions and luminescence properties

Mahdi Zamani <sup>1</sup>, Elias Stutz <sup>1</sup>, Simon Escobar <sup>1</sup>, Reza Zamani <sup>2</sup>, Rajrupa Paul <sup>1</sup>, Jean-Baptiste Leran <sup>1</sup>, Mirjana Dimitrievska <sup>1</sup>, Anna Fontcuberta i Morral <sup>1,3,\*</sup>

<sup>1</sup> Laboratory of Semiconductor Materials, Institute of Materials, École Polytechnique Fédérale de Lausanne, 1015 Lausanne, Switzerland

<sup>2</sup> Centre Interdisciplinaire de Microscopie Électronique, École Polytechnique Fédérale de Lausanne, 1015 Lausanne, Switzerland

<sup>3</sup> Institute of Physics, École Polytechnique Fédérale de Lausanne, 1015 Lausanne, Switzerland

\* corresponding author : [anna.fontcuberta-morral@epfl.ch](mailto:anna.fontcuberta-morral@epfl.ch)

### Abstract

Semiconductors made with earth abundant elements are promising as absorbers in future large-scale deployment of photovoltaic technology. This paper reports on the epitaxial synthesis of monocrystalline zinc phosphide ( $\text{Zn}_3\text{P}_2$ ) films with thicknesses up to 1  $\mu\text{m}$  thickness on  $\text{InP}$  (100) substrates, as demonstrated by high resolution transmission electron microscopy and X-ray diffraction. We explain the mechanisms by which thick monocrystalline layers can form. We correlate the crystalline quality with the optical properties by photoluminescence at 12 K. Polycrystalline and monocrystalline films exhibit dissimilar photoluminescence below the bandgap at 1.37 and 1.30 eV, respectively. Band edge luminescence at 1.5 eV is only detected for monocrystalline samples. This work establishes a reliable method for fabricating high-quality  $\text{Zn}_3\text{P}_2$  thin films that can be employed in next generation photovoltaic applications.

Keywords:  $\text{Zn}_3\text{P}_2$ , thin films, earth-abundant semiconductors, photovoltaics

### Introduction

The adverse impact of global energy consumption on the environment necessitates a massive shift in energy production toward more sustainable and non-fossil energy sources. A prominent part of a multicomponent solution is the large-scale deployment of photovoltaic (PV) energy production, which can be facilitated using semiconductors made of earth-abundant elements (1–3). However, many earth-abundant semiconductors suffer from narrow growth windows, thermodynamic instability, coexistence of multiple phases and long term degradation among other factors (4–8), affecting the performance of PV devices. A common challenge with many of these materials is the inclusion of a cation with multiple oxidation states, which, especially in high oxidation states, is likely to switch to lower oxidation numbers (9).  $\alpha\text{-Zn}_3\text{P}_2$ , on the other hand, is a candidate material with promising advantages, such as the simplicity of  $\text{Zn}-\text{P}$  system phase diagram (10–12) and thermodynamic stability thanks to the singular oxidation state of zinc. It demonstrates high absorption of more than  $10^4\text{ cm}^{-1}$  in the visible range of the electromagnetic spectrum (13,14), reported bandgap close to

the optimal value of the Shockley–Queisser limit (12,15), carrier diffusion length in the range of 5 – 10  $\mu\text{m}$  (16) and passive grain boundaries (17), which in turn could improve the performance of PV devices based on this material

Epitaxial growth of high-quality  $\text{Zn}_3\text{P}_2$  is inherently difficult, in part because of its very large tetragonal unit cell (18), with  $a = 8.089\text{ Å}$  and  $c = 11.45\text{ Å}$  (19), making it challenging to find commercially available substrate for epitaxial growth.  $\text{Zn}_3\text{P}_2$  tends to grow in the (001) direction (20). In this orientation, the  $P$  sub-lattice of the tetragonal unit cell exhibits a low lattice mismatch with the group V elements of (001) oriented  $\text{InP}$  and  $\text{GaAs}$  (2.4% and 1.3% respectively). Still, monocrystalline layers have been limited to a thickness of 150 nm on  $\text{GaAs}$  (100) (17). The other difficulty in the growth of high-quality  $\text{Zn}_3\text{P}_2$  thin films stems from its high thermal expansion coefficient. For instance, this coefficient is  $14 \times 10^{-6}\text{ K}^{-1}$  at room temperature for  $\text{Zn}_3\text{P}_2$  (21) in comparison to  $6 \times 10^{-6}\text{ K}^{-1}$  and  $3 \times 10^{-6}\text{ K}^{-1}$  for  $\text{GaAs}$  and  $\text{Si}$ , respectively. Upon cooling down, the mismatch in coefficient of thermal expansion results in formation of cracks in the thin films grown at high temperatures (22). A recent

solution that overcome these challenges corresponds to growth on graphene substrates by van der Waals epitaxy (23). In addition, restricting the interface with the substrate to nanoscale regions via the creation of nanowires or selective area epitaxy are also being investigated as potential solutions (23–26). To the best of our knowledge, to date none of these strategies has yet provided large area monocrystalline structures.

In this work, we report on the growth requirements to achieve monocrystalline  $Zn_3P_2$  thin films on  $InP(100)$  substrates. Growth parameters such as substrate temperature, ratio between P and Zn fluxes ( $V/II$  ratio) and substrate preparation are varied, resulting in amorphous, polycrystalline and monocrystalline thin films. A range of characterization techniques including Raman spectroscopy, X-ray diffraction (XRD), (scanning) transmission electron microscopy (S/TEM) and electron energy loss spectroscopy (EELS) have been employed to shed light on the differences between thin films obtained in different conditions. As a key parameter, we find that substrate surface preparation by effectively removing the native oxide is essential for obtaining monocrystalline layers. Finally, the optical properties of the thin films are investigated using photoluminescence (PL) spectroscopy and the differences between the optical characteristics of different  $Zn_3P_2$  thin film types are demonstrated.

## Results and Discussion

We start by exploring the role of the  $V/II$  ratio calibrated using a beam flux monitor and the manipulator temperature on the crystalline quality of the thin films. Substrate preparation includes two steps of sample degassing for two hours each at  $150^\circ C$  and  $300^\circ C$  in ultra-high vacuum, and a third step under  $P_2$  flux  $> 1 \times 10^{-6}$  torr at a manipulator temperature of  $580^\circ C$  to fully remove surface contaminants and the native oxide. The effects of duration of the last annealing step are discussed further down. Figure 1(a) and 1(b) depict cross-sectional scanning electron microscopy (SEM) images of typical amorphous and polycrystalline thin films, grown with  $V/II = 0.83$ ,  $T = 280^\circ C$  and  $V/II = 0.48$ ,  $T = 265^\circ C$ , respectively. The thin film in Fig. 1(a) shows a continuous and smooth structure, while in Fig. 1(b) one finds a granular structure, denoting the polycrystalline nature of the film. In this case, the cross-section SEM indicates that growth starts by forming small grains that gradually merge into larger grains as growth continues. Room temperature Raman measurements have been conducted on the samples to assess their crystalline quality. Figure 1(c) displays the Raman spectra for thin films

grown with  $V/II$  ratios between 0.43 and 1.37 and substrate temperatures between  $250^\circ C$  and  $290^\circ C$ . The characteristic spectrum of  $\alpha - Zn_3P_2$  is observed (27). A dozen low-wavenumber peaks, dominated by Zn atom displacements, merge into the broad peak at approximately  $93\text{ cm}^{-1}$ , while the high-wavenumber peaks, mainly dominated by P atom displacements, merge into a series of overlapping peaks in the range from  $280\text{ cm}^{-1}$  to  $360\text{ cm}^{-1}$  (27). The spectra of thin films grown at high  $V/II$  ratios (1.35 and 0.95) are mainly featureless or with few broad peaks, suggesting that samples obtained at high  $V/II$  ratios are amorphous, as reported in (26). This is also the case for thin films obtained at the highest temperature,  $280^\circ C$ . For  $V/II$  ratios between 0.72 and 0.95 Raman spectra of thin films grown at  $250^\circ C$  and  $265^\circ C$  are consistent with crystallinity. Similar trends have been recently observed for growth of  $Zn_3P_2$  on graphene (26).

To further improve the crystalline quality and reproducibility, effects of the third degassing step at  $580^\circ C$  for different durations are investigated. Figure 2 shows representative SEM cross-section micrographs of thin films obtained for increased degassing durations, namely 10, 20, 30, 45, 60 and 75 min. We observe that for the identical growth conditions, increasing the degassing time renders the thin films less granular. In fact, the granular nature disappears for annealing periods of 30 min or higher. Raman studies indicate that these samples are crystalline. In addition, the top surfaces of the thin films get smoother. It is to be noted that while increasing this degassing time makes it possible to obtain monocrystalline samples in a reproducible manner, a few samples with degassing times of 10 min were also monocrystalline, as presented in Figure 3. However, the occurrence of the monocrystallinity tends to be non-reproducible for samples with degassing times less than 20 min. In Figure 2(g), we show representative Raman spectra of a monocrystalline and a polycrystalline thin film acquired at 12 K with an incidence wavelength of 532 nm. A lower material temperature increases the phonon lifetime. This decreases the uncertainty of the phonon energy, lowering peak width and thus the overlap between the multiple peaks. We find that the Raman spectra obtained in different spots on each sample consistent, indicating relatively homogeneous crystalline quality. However, changes in relative intensities of the peaks can be observed between the two samples. We attribute these differences to changes in the concentrations of point defects such as interstitials/vacancies or grain boundaries, which affect different vibrational modes of the lattice in varying ways. A detailed study to identify the defects in  $Zn_3P_2$  thin films with Raman spectroscopy is ongoing.

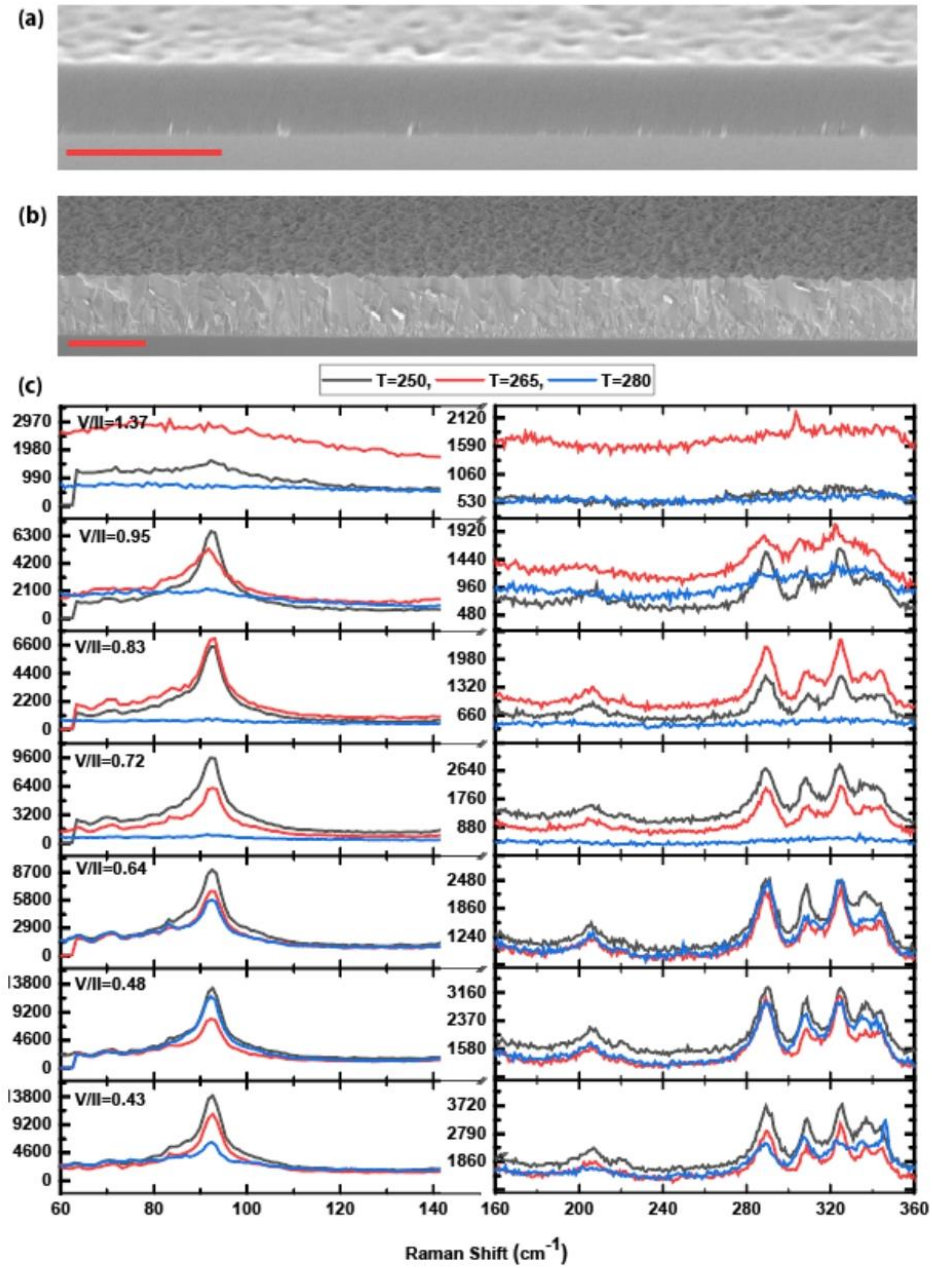


Figure 1: effect of growth temperature and  $V/II$  ratios. (a):  $20^\circ$  tilted cross section image of an amorphous  $Zn_3P_2$  thin film grown with  $V/II = 0.83$  and  $T = 280^\circ C$ . (b): tilted cross section image of a polycrystalline  $Zn_3P_2$  thin film grown with  $V/II = 0.48$  and  $T = 265^\circ C$ , demonstrating the presence of grain boundaries. Scale bars are  $1\mu m$ . (c) Raman measurements for samples grown at different growth temperatures and  $V/II$  ratios. Increasing the growth temperature and  $V/II$  ratio makes the films amorphous. All the samples reported in this figure have degassing time at  $580^\circ C$  of 10 mins and P flux of  $4.3 \times 10^{-7}$  torr.

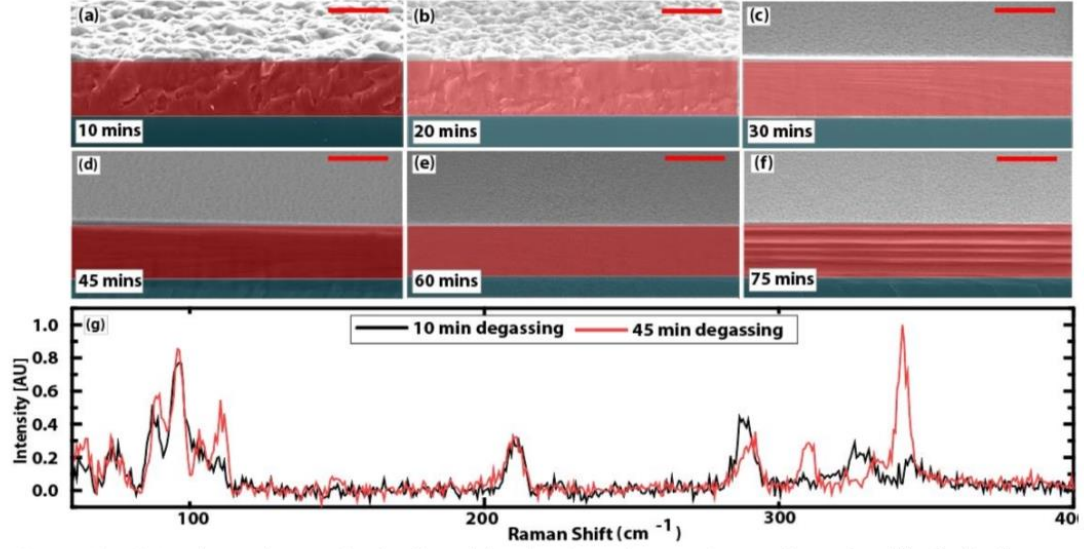


Figure 2: (a) – (f) SEM images demonstrating the effects of degassing time at 580 °C on the crystalline quality of  $Zn_3P_2$  thin films. No apparent grains are observed for a degassing time  $\geq 30$  mins. The red scale bar is 1  $\mu m$ . The transparent blue layer indicated the substrate, while the transparent red area highlights the cross section of the thin films. (g) comparison of the Raman spectra of samples with degassing time at 580 °C of 10 min and 45 min. These samples are polycrystalline and monocrystalline, respectively. All the samples reported here are grown on p-doped  $InP(100)$  substrates with identical growth conditions of  $T = 245^\circ C$ ,  $V/II = 0.72$  and  $P = 5.81 \times 10^{-7} torr$ . The SEM images are acquired at 20° tilt.

High-resolution (HR) TEM and aberration-corrected high-angle annular dark-field (HAADF) STEM are used to investigate the crystalline quality. Figure 3(a) corresponds to a HRTEM image of a thin film obtained with  $V/II = 0.72$ ,  $T = 265^\circ C$  and the degassing time of 10 min at 580 °C. HRTEM indicates that this is a monocrystalline thin film. The diffraction pattern obtained on a larger area also corroborates the monocrystallinity, as shown in the inset of Figure 3(a). Calculations of atomic distances based on the selective-area diffraction pattern demonstrates a lattice mismatch of 2% considering the pseudo-cubic structure of  $Zn_3P_2$  and the growth direction of  $[001]$ , consistent with previous studies (20,25). The HAADF-STEM image of this sample in Figure 3(b) adds further details of the interface between the film and the substrate. Considering that the heavier atoms appear brighter in HAADF-STEM images due to Z-contrast (28–30), the constituting elements can be assigned across the interface. The brightness of atoms at the interface, intermediate between the one observed for In in the substrate and Zn in the layer

indicates the formation of a mixed  $Zn - In$  monolayer, as depicted in the blue inset of figure 3(b). The monolayer Zn-In intermixing establishes the epitaxial transition from the  $InP$  substrate to the  $Zn_3P_2$  film. The red inset of this figure establishes that while monocrystalline, these films may still include some structural defects stemming from misalignment of the systematic vacant sites in c direction. Figure 3(c) probes the oxygen core-loss EELS signature at 532 eV across the interface of this sample, demonstrating a uniform absence of oxygen around this area. Figure 3(d) corresponds to a low magnification TEM image of a sample obtained at  $V/II = 0.48$ ,  $T = 265^\circ C$  and with a degassing time of 10 min at 580 °C. The micrograph shows the polycrystalline nature with a clear pattern of columnar-structured grains. The HAADF-STEM image of this sample in Figure 3(e) further highlights the difference between the polycrystalline and the monocrystalline thin films, as the area above the interface appears diffused as opposed to the sharp interface of the monocrystalline film. Moreover, in this micrograph one can



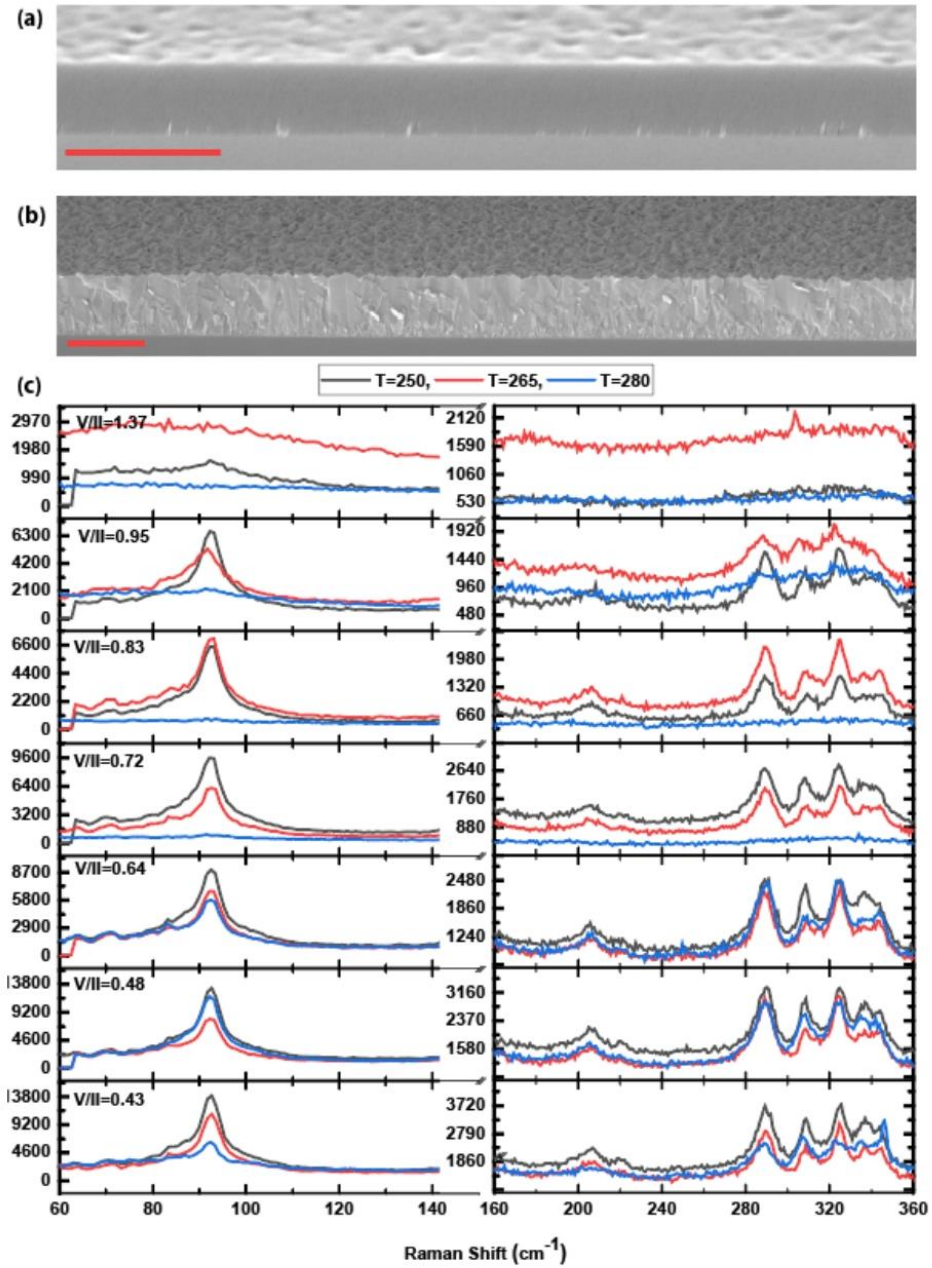


Figure 1: effect of growth temperature and  $V/II$  ratios. (a): 20 ° tilted cross section image of an amorphous  $Zn_3P_2$  thin film grown with  $V/II = 0.83$  and  $T = 280^\circ C$ . (b): tilted cross section image of a polycrystalline  $Zn_3P_2$  thin film grown with  $V/II = 0.48$  and  $T = 265^\circ C$ , demonstrating the presence of grain boundaries. Scale bars are  $1\mu m$ . (c) Raman measurements for samples grown at different growth temperatures and  $V/II$  ratios. Increasing the growth temperature and  $V/II$  ratio makes the films amorphous. All the samples reported in this figure have degassing time at  $580^\circ C$  of 10 mins and P flux of  $4.3 \times 10^{-7}$  torr.

notice the randomly oriented atomic fringes in the thin film. Figure 3(f) corresponds to the oxygen map by core-loss EELS of the interface area shown in Figure 3(e). There is a clear oxygen signature at the interface. The presence of an oxide could be the reason for the lack of sharpness of the interface in the HAADF image. In conclusion, the increase in degassing

time at 580 °C promotes the complete desorption of the substrate native oxide, which in turn facilitates the formation of a monocrystalline thin film.

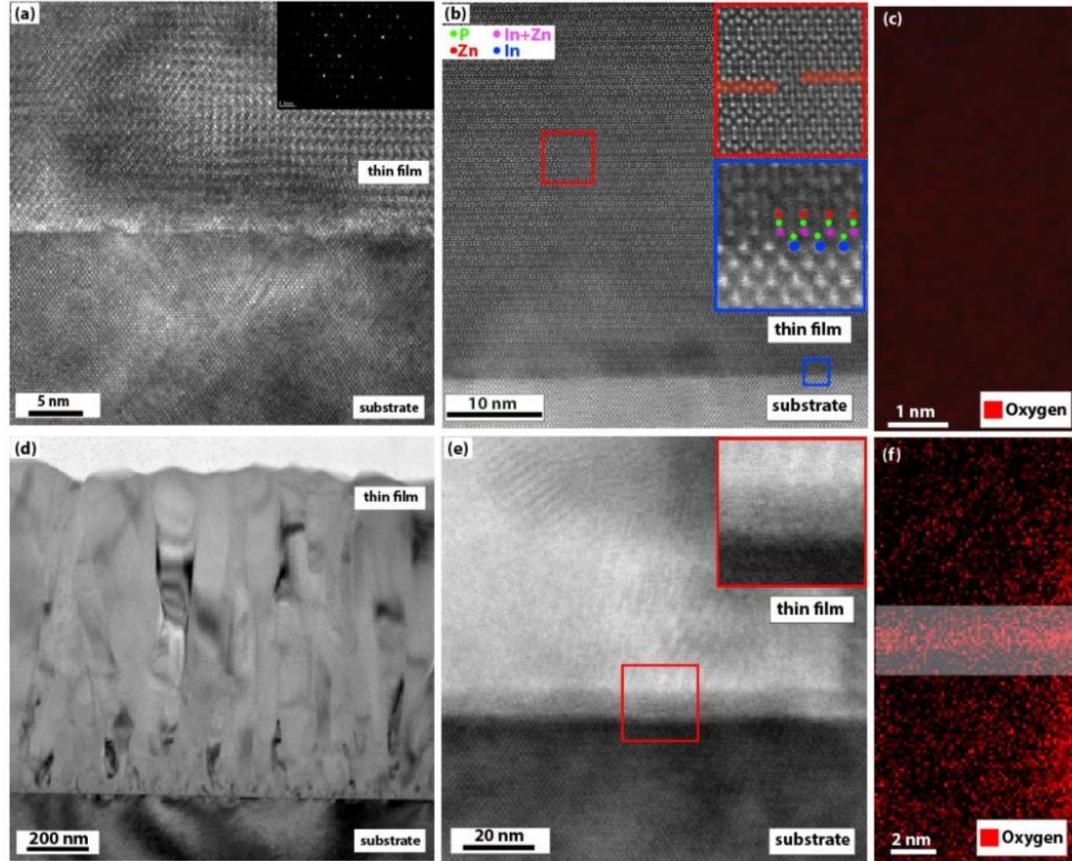


Figure 3: (S)TEM/ EELS comparison of monocrystalline and polycrystalline thin films. (a) HRTEM image of a monocrystalline sample grown at  $V/II = 0.72$ ,  $T = 265\text{ }^{\circ}\text{C}$  and with a degassing time of 10 min at 580 °C. The inset depicts a diffraction pattern corresponding to a larger area. (b) HAADF-STEM image of the same sample showing the epitaxial relationship between the substrate and the thin film. The blue inset demonstrates the state of interface while the red inset highlights in-plane defect stemming from the vertical misalignment of the systematic vacant sites. (c) The core-loss oxygen EELS map of the interface between the substrate and the monocrystalline thin film demonstrating the absence of oxygen across the interface. (d) low-magnification TEM image of a polycrystalline sample grown at  $V/II = 0.48$ ,  $T = 265\text{ }^{\circ}\text{C}$  and the degassing time of 10 min at 580 °C. (e) HAADF-STEM image of the same sample showing the diffused interface and the lack of epitaxial relationship between the substrate and the polycrystalline thin film. (f) The core-loss oxygen EELS map of the interface between the substrate and the polycrystalline thin film demonstrating the pronounced concentration of oxygen across the interface highlighted by the transparent white strip overlaying the map.

To further examine the crystalline quality of the thin films obtained under the different conditions, high resolution XRD

was performed. Figure 4 compares the XRD pattern for bare *InP* substrate, amorphous, polycrystalline and



monocrystalline  $Zn_3P_2$  thin films. The growth conditions of each thin film are presented in the figure caption. The most intense peak, observed at  $30.4^\circ$ , corresponds to the (200) reflection of the  $InP$  substrate (31). Dashed vertical lines are employed to highlight the location of the peaks stemming from the  $InP$  substrate. Some of these peaks are absent on the amorphous sample (with broad peaks of  $Zn_3P_2$  in the Raman spectra). The main crystalline signature of  $Zn_3P_2$ , observed at  $31.4^\circ$  corresponds to the (004) reflection (32), and is observed on both polycrystalline and monocrystalline thin films. Multiple peaks corresponding to the higher index planes are observed for the polycrystalline thin film between  $30^\circ$  and  $50^\circ$ . These peaks are absent on the monocrystalline film, with only peaks corresponding to (002), (004) and (006) directions of  $Zn_3P_2$  being visible. This indicates that the growth direction of the monocrystalline film is [001], consistent with the HRTEM analysis.

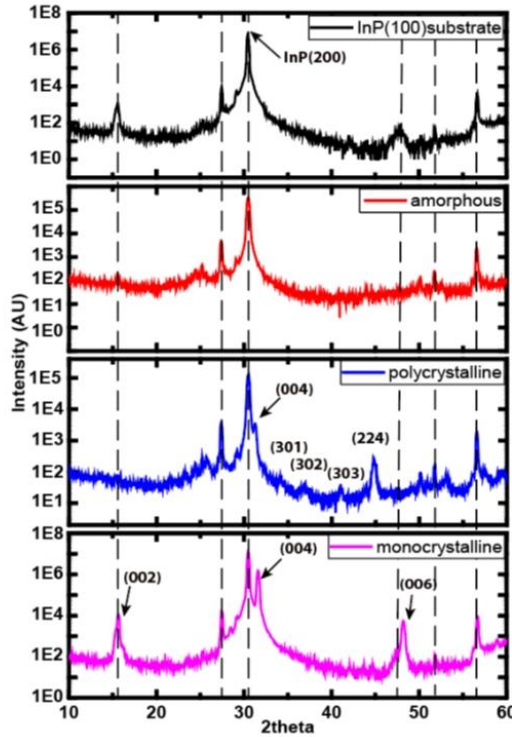


Figure 4: XRD comparison of different sample types. (a) XRD scan of a bare  $InP(100)$  substrate showing a pattern dominated by (200) peak at  $30.4^\circ$  and few other  $InP$  peaks. The dashed black lines indicate the position of  $InP$  substrate peaks which are also observed on the other samples. (b) XRD pattern of an amorphous sample with  $V/II = 0.83$  and  $T = 280^\circ C$  (c) XRD pattern of a polycrystalline sample grown at  $V/II = 0.48$ ,  $T = 265^\circ C$  and with

a degassing time of 10 min at  $580^\circ C$ , demonstrating the  $Zn_3P_2(004)$  peak at  $31.4^\circ$  in addition to other, less intense peaks between  $30^\circ$  and  $50^\circ$  that correspond to higher-index planes. (d) XRD pattern of a monocrystalline sample grown at  $V/II = 0.72$ ,  $T = 265^\circ C$  and with a degassing time of 10 min at  $580^\circ C$ . From  $Zn_3P_2$ , only (002), (004) and (006) peaks are observed, which all belong to the {001} family.

Low temperature PL was performed to evaluate and compare the optical properties of the polycrystalline and monocrystalline samples. In general, we find that the emission spectrum from polycrystalline samples strongly depends on the growth parameters. In Figure 5, representative PL measurements for one polycrystalline and one representative monocrystalline sample measured with an excitation wavelength of 488 nm at 20 K are shown. In addition, the emission spectrum of a bare  $InP$  substrate is also included as a reference. The orange curve in Figure 5 corresponds to the PL data of a typical polycrystalline sample. The emission spectra from polycrystalline  $Zn_3P_2$  thin films consists of a single peak or a single set of overlapping peaks at energies lower than the direct bandgap energy (15,33). Similar results have been observed in  $Zn_3P_2$  and in other systems in the past and are attributed to defects (34,35). Other polycrystalline films, not shown in this figure, emit at slightly different energies, generally within a few dozen meV below 1.4 eV. The substrate emission is almost always observed, even though the film thickness is several times the penetration depth of the laser (15). In addition to the differences in the optical properties of the different polycrystalline films, their emission shows minor variation based on the location, which could be due to the local variation of the properties such as density of defects across the thin film. If the probability of recombining through a radiative path instead of a non-radiative path is different in the substrate and the film, any change in the diffusion and trapping of carriers may affect the relative intensities of the substrate and film emissions.

Our monocrystalline thin films exhibit a homogeneous emission spectrum over the whole sample. In Figure 5, a representative photoluminescence spectrum of a monocrystalline sample is demonstrated by the black curve. The  $InP$  substrate emission is still measurable at 1.43 eV. For  $Zn_3P_2$  we observe two peaks: a broad peak at lower energy, 1.3 eV and another at higher-energy centered around 1.52 eV. The latter is consistent with the direct bandgap of  $Zn_3P_2$  (15). The inset in Figure 5 illustrates a magnified view of this peak. Although Kimball *et al.* attributed the 1.3 eV emission to the indirect bandgap (15), we find it difficult to justify a higher emission intensity for an indirect transition. We think this emission may rather be linked to radiative recombination from defect levels below the bandgap. On the other hand, Briones *et al.* assigned the transitions observed in their spectra in the

range of 1.31 eV to 1.37 eV to donor-acceptor pair transitions (37). We think this might be a more accurate description of the optical recombination process.

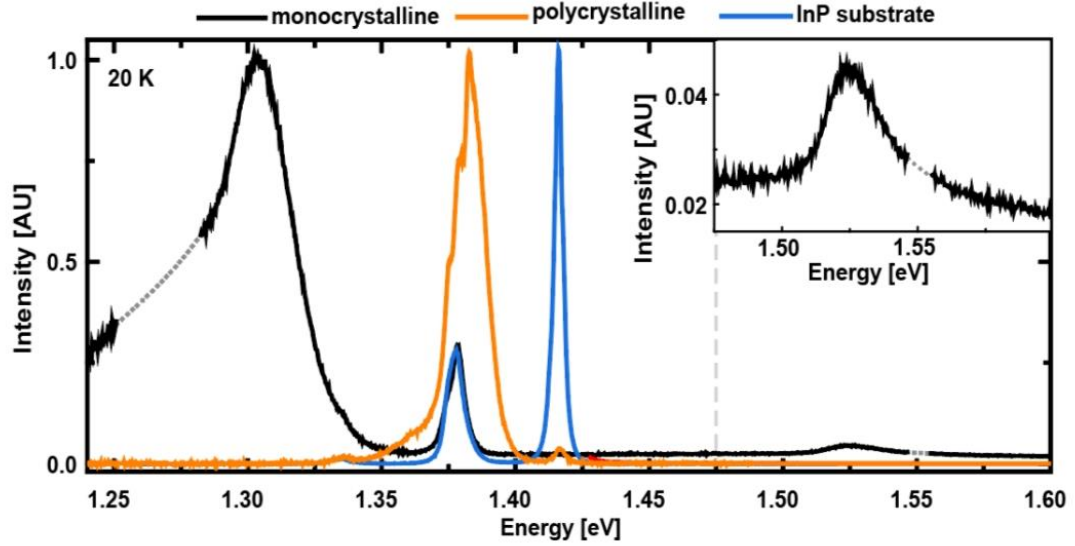


Figure 5: Photoluminescence measurements showing the difference in the optical properties of polycrystalline and monocrystalline samples. The dashed parts of the curves are where the laser peaks have been removed for the spectra of the monocrystalline sample. The measurements have been conducted at 20 K using radiant fluxes of  $470\mu W$ ,  $0.47\mu W$  and  $1170\mu W$  on the monocrystalline, polycrystalline and InP substrate samples, respectively.  $V/II = 0.72$   $T = 265^\circ C$  and  $V/II = 0.48$ ,  $T = 265^\circ$  have been used to grow the monocrystalline and polycrystalline samples, respectively, with a degassing time of 10 min at  $580^\circ C$  for both.

## Conclusion

In this study, we provide the main elements for the growth of monocrystalline  $Zn_3P_2$  films with thicknesses up to  $1\mu m$  on  $InP(100)$ , ranging from the tuning of the growth conditions to the substrate preparation. While this study focus on InP substrate, we believe the lessons learned can be relevant to other substrates. In particular, we highlight the long time necessary to completely desorb the native substrate oxide, key to obtain monocrystalline layers. We also provide the temperature and  $II/V$  flux window that lead to stoichiometric and crystalline growth. Finally, we compare the luminescence between monocrystalline and polycrystalline layers. Luminescence from polycrystalline samples is dominated by emission below the bandgap. Monocrystalline samples also exhibit luminescence below the bandgap. Compared to the polycrystalline, the emission is considerably brighter and at lower energy. In addition, we observe band-edge luminescence, a sign of the high quality of the material. Further work is needed to identify the physical origin of the luminescence bands below the bandgap.

## Methods

$Zn_3P_2$  thin films were grown using a Veeco GENxplor MBE system operating with separate  $Zn$  and  $P$  sources. The samples are obtained on  $InP(100)$  substrate. Substrate preparation includes two steps of degassing for two hours at  $150^\circ C$  and  $300^\circ C$  and a third stage at  $580^\circ C$  under  $P_2$  equivalent beam pressures  $> 1 \times 10^{-6} Torr$ . Unless otherwise stated, the duration of this step is 10 mins.

All the Raman measurements reported in Figure 1 are done using confocal Raman spectroscopy operating with a 532 nm laser. The spectra offered is accumulation of 20 counts, each having the exposure time of 1s and laser power of  $9\mu W$ .

The micro-Raman measurements shown in Figure 2 have been acquired in back-scattering geometry at 12 K using the 532 nm line of a Coherent Sapphire SF laser for excitation. A microscope objective with a numerical aperture of 0.75 was used to focus the light onto the sample to a spot with a



diameter of about  $1\ \mu\text{m}$ . The incident light is linearly polarized, while all the scattered light is collected regardless of the polarization. The signal was analysed using a TriVista triple spectrometer with 900, 900 and  $1800\ \text{mm}^{-1}$  gratings in subtractive mode and a Princeton Instruments multichannel CCD PyLoN camera. The SEM images in Figure 1 and Figure 2 are acquired in a Zeiss Merlin field emission microscope. The TEM samples in Figure 3 are prepared by Zeiss NVision 40 CrossBeam dual focused ion beam (FIB)/ SEM with liquid Ga ion source. TEM images in Figure 3 are captured by FEI Tecnai Osiris operating at  $200\ \text{KeV}$ . The STEM images and EELS maps in Figure 3 are captured by a FEI Titan Themis 60-300 kV, equipped with X-FEG, monochromator,  $C_s$  aberration (image and probe) correctors, and Gatan GIF Quantum ERS spectrometer, operating at  $200\ \text{KeV}$ .

The XRD patterns in Figure 4 are captured by a Panalytical Empyrean diffractometer operating in Goni scan configuration with a Cu ( $K\alpha$ ) X-ray source of  $1.54\ \text{\AA}$  operating at  $45\ \text{KeV}$  and  $40\ \text{mA}$ .

The micro-photoluminescence measurements, shown in figure 5, have been acquired in back-scattering geometry at  $20\ \text{K}$  using the  $488\ \text{nm}$  line of a Coherent Sapphire SF laser and an Andor iDus DV420A-OE detector. The spectra have been corrected for the response of the detector. A microscope objective with a numerical aperture of 0.75 was used to focus the light onto the sample to a spot with a diameter of about  $1\ \mu\text{m}$ . Radiant fluxes of approximately  $470\ \mu\text{W}$ ,  $470\ \mu\text{W}$ ,  $0.47\ \mu\text{W}$  and  $1170\ \mu\text{W}$  were used on the monocrystalline, polycrystalline 1, polycrystalline 2 and InP substrate samples, respectively. 100 accumulations of 1s,  $\sim 0.01\text{s}$  and  $\sim 0.01\text{s}$  were used on the first three samples, respectively, and 1 accumulation of  $\sim 0.01\text{s}$  was used to acquire the spectrum from InP.

## References

- Wadia C, Alivisatos AP, Kammen DM. Materials availability expands the opportunity for large-scale photovoltaics deployment. *Environ Sci Technol*. 15 Maart 2009;43(6):2072–7.
- Zhang X, Huang M, Xu P, Dai CM, Cai ZH, Han D, et al. Earth-abundant photovoltaic semiconductor  $\text{NaSbS}_2$  in the rocksalt-derived structure: A first-principles study. *Prog Nat Sci Mater Int*. 01 Junie 2019;29(3):322–8.
- Earth-Abundant Materials for Solar Cells:  $\text{Cu}_2\text{-II-IV-VI}_4$  Semiconductors | Wiley.
- Hall RB, Birkmire RW, Phillips JE, Meakin JD. Thin-film polycrystalline  $\text{Cu}_2\text{S}/\text{Cd}_1\text{-xZnx S}$  solar cells of 10% efficiency. 1998;
- Wadia C, Wu Y, Gul S, Volkman SK, Guo J, Alivisatos AP. Surfactant-assisted hydrothermal synthesis of single phase pyrite  $\text{FeS}_2$  nanocrystals. *Chem Mater*. 14 Julie 2009;21(13):2568–70.
- Yuan B, Luan W, Tu ST, Wu J. One-step synthesis of pure pyrite  $\text{FeS}_2$  with different morphologies in water. *New J Chem*. 01 Mei 2015;39(5):3571–7.
- Yin L, Cheng G, Feng Y, Li Z, Yang C, Xiao X. Limitation factors for the performance of kesterite  $\text{Cu}_2\text{ZnSnS}_4$  thin film solar cells studied by defect characterization. *RSC Adv*. 30 April 2015;5(50):40369–74.
- S. P, P. T. Thin Film Solar Cells Using Earth-Abundant Materials. In: *Solar Cells - Research and Application Perspectives*. InTech; 2013.
- Scrugg JJ, Dale PJ, Colombara D, Peter LM. Thermodynamic aspects of the synthesis of thin-film materials for solar cells. *ChemPhysChem*. 27 Augustus 2012;13(12):3035–46.
- Liu Y, Zhou B, Lv W, Wu C, Su X, Wang J. Experimental investigation and thermodynamic assessment of the  $\text{Zn-Si-P}$  system. *Surf Coatings Technol*. 25 November 2016;306:370–7.
- Tu H, Yin F, Su X, Liu Y, Wang X. Experimental investigation and thermodynamic modeling of the  $\text{Al-P-Zn}$  ternary system. *Calphad Comput Coupling Phase Diagrams Thermochem*. 01 Desember 2009;33(4):755–60.
- Ghasemi M, Stutz E, Escobar Steinvall S, Zamani M, Fontcuberta i Morral A. Thermodynamic reassessment of the  $\text{Zn-P}$  binary system. *Materialia*. 01 Junie 2019;6:100301.
- Swinkels MY, Campo A, Vakulov D, Kim W, Gagliano L, Steinvall SE, et al. Measuring the Optical Absorption of Single Nanowires. *Phys Rev Appl*. 01 Augustus 2020;14(2):024045.
- Fagen EA. Optical properties of  $\text{Zn}_3\text{P}_2$ . *J Appl Phys*. 25 Oktober 1979;50(10):6505–15.
- Kimball GM, Müller AM, Lewis NS, Atwater HA. Photoluminescence-based measurements of the energy gap and diffusion length of  $\text{Zn}_3\text{P}_2$ . *Appl Phys Lett*. 14 September 2009;95(11):112103.
- Wyeth NC, Catalano A. Spectral response measurements of minority-carrier diffusion length in  $\text{Zn}_3\text{P}_2$ . *J Appl Phys*. 29 Maart 1979;50(3):1403–7.
- Pseudomorphic growth and strain relaxation of  $\alpha\text{-Zn}_3\text{P}_2$  on  $\text{GaAs}(001)$  by molecular beam epitaxy. *J*

- Cryst Growth. 15 Januarie 2013;363:205–10.
18. Sierański K, Szatkowski J, Misiewicz J. Semiempirical tight-binding band structure of II3V2 semiconductors: Cd3P2, Zn3P2, Cd3As2, and Zn3As2. *Phys Rev B*. 15 September 1994;50(11):7331–7.
  19. Stackelberg MVPP. Investigation of Phosphides and Arsenides of Zinc and Cadmium, The Structure of Zn3P2. *phys Chem*. 1935;427–760.
  20. Suda T, Kakishita K, Sato H, Sasaki K. N-type zinc phosphide grown by molecular beam epitaxy. *Appl Phys Lett*. 04 Junie 1996;
  21. Long J. The Growth of Zn[sub 3]P[sub 2] by Metalorganic Chemical Vapor Deposition. *J Electrochem Soc*. 1983;130(3):725.
  22. Chu TL, Chu SS, Murthy K, Stokes ED, Russell PE. Deposition and properties of zinc phosphide films. *J Appl Phys*. 14 April 1983;54(4):2063–8.
  23. Escobar Steinvall S, Tappy N, Ghasemi M, Zamani RR, Lagrange T, Stutz EZ, et al. Multiple morphologies and functionality of nanowires made from earth-abundant zinc phosphide. *Nanoscale Horizons*. 01 Februarie 2020;5(2):274–82.
  24. Escobar Steinvall S, Ghisalberti L, Zamani RR, Tappy N, Hage FS, Stutz EZ, et al. Heterotwin Zn<sub>3</sub>P<sub>2</sub> superlattice nanowires: the role of indium insertion in the superlattice formation mechanism and their optical properties. *Nanoscale*. 20 November 2020;12(44):22534.
  25. Escobar Steinvall S, Stutz EZ, Paul R, Zamani M, Dzade NY, Piazza V, et al. Towards defect-free thin films of the earth-abundant absorber zinc phosphide by nanopatterning. *Nanoscale Adv*. 2020;
  26. Paul R, Humblot N, Humblot N, Steinvall SE, Stutz EZ, Joglekar SS, et al. Van der Waals Epitaxy of Earth-Abundant Zn<sub>3</sub>P<sub>2</sub> on Graphene for Photovoltaics. *Cryst Growth Des*. 03 Junie 2020;20(6):3816–25.
  27. Stutz EZ, Escobar Steinvall S, Litvinchuk AP, Leran J-B, Zamani M, Paul R, et al. Raman spectroscopy and lattice dynamics calculations of tetragonally-structured single crystal zinc phosphide (Zn<sub>3</sub>P<sub>2</sub>) nanowires. *Nanotechnology*. 19 Februarie 2021;32(8):085704.
  28. Grillo V, Carlino E, Glas F. Influence of the static atomic displacement on atomic resolution Z-contrast imaging. *Phys Rev B - Condens Matter Mater Phys*. 11 Februarie 2008;77(5):054103.
  29. De La Mata M, Magen C, Gazquez J, Utama MIB, Heiss M, Lopatin S, et al. Polarity assignment in ZnTe, GaAs, ZnO, and GaN-AlN nanowires from direct dumbbell analysis. *Nano Lett*. 09 Mei 2012;12(5):2579–86.
  30. Zamani RR, Gorji Ghalamestani S, Niu J, Sköld N, Dick KA. Polarity and growth directions in Sn-seeded GaSb nanowires. *Nanoscale*. 07 Maart 2017;9(9):3159–68.
  31. PDF 00-032-0452 [Internet]. [cited 13 November 2020]. Available at: <https://www.icdd.com/pdfsearch/>
  32. PDF 00-053-0591 [Internet]. [cited 13 November 2020]. Available at: <https://www.icdd.com/pdfsearch/>
  33. Stamov IG, Syrbu NN, Dorogan A V. Energetic band structure of Zn3P2 crystals. *Phys B Condens Matter*. 01 Januarie 2013;408(1):29–33.
  34. Yamazaki M, Nakagawa M, Jimbo K, Shimamune Y, Katagiri H. Photoluminescence study of Cu<sub>2</sub>ZnSnS<sub>4</sub> thin film solar cells. *Phys Status Solidi Curr Top Solid State Phys*. 01 Junie 2017;14(6).
  35. Halliday DP, Potter MDG, Mullins JT, Brinkman AW. Photoluminescence study of a bulk vapour grown CdTe crystal. *J Cryst Growth*. 15 November 2000;220(1–2):30–8.
  36. Nayak A, Rao DR. Photoluminescence spectra of Zn3P2-Cd 3P2 thin films. *Appl Phys Lett*. 02 Augustus 1993;63(5):592–3.
  37. Briones F, Wang FC, Bube RH. Pair transitions in Zn3P2. *Appl Phys Lett*. 15 November 1981;39(10):805–7.

## 3.2 Liquid ordering at the interface of crystalline *GaAs* and liquid *Ga*

In this work, we tried to shed some light on the reason for the structural differences between A- polar and B- polar *GaAs* NWs. As discussed in Introduction chapter, A- polar NWs exhibit higher crystalline quality without defects and polytypism, which is the opposite of common observations in B- polar NWs. The reasons for these differences have not been understood before.

In order to study the origins of this phenomenon, a new framework for analyzing the growth of NWs needed to be developed. Up to now, the atomistic nature of the interface between the NWs and their catalyst droplet had been neglected and the interface between these two phases had been treated as a passive border with infinitely small thickness and no distinct structural and functional properties. In this study, we have demonstrated for the first time that the atomistic structure of the interface and its properties indeed play a vital role in determining the growth properties of *GaAs* NWs.

This study is composed of two main parts. In the experimental section, aberration corrected HAADF-STEM is used to shed light on the atomistic structure of the interface between the crystalline *GaAs* and liquid *Ga* in both A- polar and B- polar NWs. The growth of these NWs was first reported in reference (117). Special care is given to minimize the beam damage and preserve the fragile, quasi- liquid structure of this interface. The order range perpendicular to the interface is observed to be vastly different between A-polar and B- polar cases: for A-polar interface, only one layer of ordered liquid is present, while the order can last for up to four layers for the B-polar interface. Then, low loss EELS is used to establish for the first time that this ordered region has its own distinct functional properties. Due to the delocalized nature of the plasmonic oscillations, it is not possible to directly access the EELS spectra of this ordered liquid region, and special mathematical treatment in the form of independent component analysis (ICA) is employed to separate these spectra.

The second part of this study, performed by the laboratory of computational science and modeling (COSMO) lead by Prof. Michele Ceriotti at EPFL, uses machine-learning based molecular dynamics to calculate the atomistic structure of this liquid- solid interface. The HAADF-STEM images are used to cross-check the accuracy of these simulations. Once validated, the simulation results provide a 3D view of the ordering at the interface, which is not possible with electron microscopy. These results provide insight into the fundamental differences in the growth of A- polar and B- polar NWs. The differences in the atomic stacking of liquid *Ga* atoms at the interface between A- polar and B-polar cases are used to understand the reasons for the structural differences of these two types of growths and inherent difficulty of growing A- polar NWs. To the best of our knowledge, this is the first time that the 3D nature of ordering at the liquid solid interface has been identified and correlated to crystal growth properties.

Reprinted with open access permission from M. Zamani *et al.* “3D Ordering at the Liquid-Solid Polar Interface of Nanowires” *Advanced Materials*, 2020, 32, 2001030 © Wiley- VCH.

# 3D Ordering at the Liquid–Solid Polar Interface of Nanowires

Mahdi Zamani, Giulio Imbalzano, Nicolas Tappy, Duncan T. L. Alexander, Sara Martí-Sánchez, Lea Ghisalberti, Quentin M. Ramasse, Martin Friedl, Gözde Tütüncüoğlu, Luca Francaviglia, Sebastien Bienvenue, Cécile Hébert, Jordi Arbiol, Michele Ceriotti,\* and Anna Fontcuberta i Morral\*

The nature of the liquid–solid interface determines the characteristics of a variety of physical phenomena, including catalysis, electrochemistry, lubrication, and crystal growth. Most of the established models for crystal growth are based on macroscopic thermodynamics, neglecting the atomistic nature of the liquid–solid interface. Here, experimental observations and molecular dynamics simulations are employed to identify the 3D nature of an atomic-scale ordering of liquid Ga in contact with solid GaAs in a nanowire growth configuration. An interplay between the liquid ordering and the formation of a new bilayer is revealed, which, contrary to the established theories, suggests that the preference for a certain polarity and polytypism is influenced by the atomic structure of the interface. The conclusions of this work open new avenues for the understanding of crystal growth, as well as other processes and systems involving a liquid–solid interface.

Understanding the nature of interfaces is key to determining and engineering their properties. However, while liquid–solid interfaces are fundamental to many applications and interactions, relatively little is known about them at the atomic level. Here, we use vapor–liquid–solid (VLS) grown nanowires (NWs) as a model system to identify and interpret the atomistic nature of a liquid–solid interface in three dimensions. VLS is a widely used method of crystal growth relying on the precipitation of a solid from a supersaturated nanodroplet.<sup>[1]</sup> Recent in situ investigations have revealed that precipitation/growth proceeds in a layer-by-layer fashion, similarly to thin film epitaxy.<sup>[2,3]</sup> Growth of NWs can occur

M. Zamani, N. Tappy, L. Ghisalberti, Dr. M. Friedl, Dr. G. Tütüncüoğlu, Dr. L. Francaviglia, Prof. A. Fontcuberta i Morral  
Laboratory of Semiconductor Materials  
Institute of Materials  
Faculty of Engineering  
École Polytechnique Fédérale de Lausanne  
EPFL  
Lausanne 1015, Switzerland  
E-mail: anna.fontcuberta-morral@epfl.ch  
G. Imbalzano, S. Bienvenue, Prof. M. Ceriotti  
Laboratory of Computational Science and Modeling  
Institute of Materials  
Faculty of Engineering  
École Polytechnique Fédérale de Lausanne  
EPFL  
Lausanne 1015, Switzerland  
E-mail: michele.ceriotti@epfl.ch  
Dr. D. T. L. Alexander, Prof. C. Hébert  
Electron Spectrometry and Microscopy Laboratory  
Institute of Physics  
Faculty of Basic Sciences  
École Polytechnique Fédérale de Lausanne  
EPFL  
Lausanne 1015, Switzerland

Dr. D. T. L. Alexander  
Interdisciplinary Centre for Electron Microscopy (CIME)  
École Polytechnique Fédérale de Lausanne  
EPFL  
Lausanne 1015, Switzerland  
Dr. S. Martí-Sánchez, Prof. J. Arbiol  
Catalan Institute of Nanoscience and Nanotechnology (ICN2)  
CSIC and BIST  
Campus UAB, Bellaterra, Barcelona, Catalonia 08193, Spain  
Prof. Q. M. Ramasse  
SuperSTEM Laboratory  
SciTech Daresbury Campus  
Keckwick Lane, Daresbury WA4 4AD, UK  
Prof. Q. M. Ramasse  
School of Chemical and Process Engineering and School of Physics and Astronomy  
University of Leeds  
Leeds LS2 9JT, UK  
Prof. C. Hébert  
Institute of Materials  
Faculty of Engineering  
École Polytechnique Fédérale de Lausanne  
EPFL  
Lausanne 1015, Switzerland  
Prof. J. Arbiol  
ICREA  
Pg. Lluís Companys 23  
Barcelona, Catalonia 08010, Spain  
Prof. A. Fontcuberta i Morral  
Institute of Physics  
Faculty of Basic Sciences  
École Polytechnique Fédérale de Lausanne  
EPFL  
Lausanne 1015, Switzerland

 The ORCID identification number(s) for the author(s) of this article can be found under <https://doi.org/10.1002/adma.202001030>.

© 2020 The Authors. Published by Wiley-VCH GmbH. This is an open access article under the terms of the Creative Commons Attribution License, which permits use, distribution and reproduction in any medium, provided the original work is properly cited.

DOI: 10.1002/adma.202001030



in different growth directions, crystal structures, and polarities,<sup>[4–6]</sup> currently understood by relating the prevalence of these properties to the wetting characteristics of the liquid on the tip of the NWs,<sup>[5,7]</sup> where the role of the liquid droplet contact angle is widely discussed but remains controversial.<sup>[4,8]</sup> So far, the liquid–solid boundary is considered as a clear-cut, binary interface, with no regard for its structure. Modeling has mostly reasoned in terms of macroscopic parameters, including contact angle, the surface energies at the solid–vapor and liquid–solid interfaces and the chemical potentials.<sup>[9,10]</sup> The atomistic nature of the participating parts has rarely been considered.

The idea that a solid surface can induce local order to an adjacent liquid phase has previously been demonstrated in simulations of interfaces between solids and aqueous solutions, as well as liquid metals in contact with their solid compounds.<sup>[11–13]</sup> In addition, there have been some experimental attempts to study such ordering.<sup>[14–16]</sup> In particular, grazing incident X-ray diffraction has been used to study the ordering of liquid AuSi alloy,<sup>[17,18]</sup> and in situ X-ray diffraction has been employed to study the liquid ordering at the interface between P-terminated crystalline InP substrate and liquid InAu phase.<sup>[19]</sup> While this second study was targeted at understanding VLS-NW growth, due to the geometrical difficulties for probing NWs using X-rays, it was limited to investigating an interface in which a bulk liquid completely covers a bulk substrate, as opposed to the measurement of a nanoscale droplet in contact with the crystalline NW. It further applied an assumption of a fixed spacing between the ordered liquid layers. In addition, the composition of the liquid phase was tuned to match that observed in the gold-catalyzed growth of InP NWs; therefore, it is not clear if the results can apply to the self-catalyzed growth of III–V NWs. Using electron microscopy, Kaplan and co-workers studied the longitudinal ordering of liquid Al at the interface with Al<sub>2</sub>O<sub>3</sub>, which can extend up to five layers depending on the facets.<sup>[14]</sup> However, thus far, the effect of such ordering has been ignored in the VLS growth.

In this work, we combine scanning transmission electron microscopy (STEM), electron energy loss spectroscopy (EELS), atomic simulations using machine learning potentials and molecular dynamics (MD) to demonstrate, for the first time, the polarity-dependent 3D nature of the liquid ordering at the solid interface.

The study is performed in the frame of the VLS growth of NWs. We elucidate the interplay between the ordering and the formation of a new bilayer, the preference for a certain polarity and the effect of ordering on defect formation. While our study concentrates on the Ga-assisted growth of GaAs, the results can extend to other relevant cases such as Au-assisted NW growth, bulk crystal growth from the melt, and even liquid–solid interaction in the context of biological environments.

We start by providing experimental evidence of liquid ordering at the interface with the solid in a VLS-grown NW using aberration-corrected STEM. Our study focuses on the Ga(l)–GaAs(s) interface of A and B polar GaAs NWs obtained by the Ga-assisted method.<sup>[20,21]</sup> A schematic drawing of the process is provided in **Figure 1A**. A Ga droplet preferentially gathers As<sub>4</sub> molecules, which dissolve in the droplet. The chemical bonding between As and Ga results in the growth of GaAs at the bottom of the droplet.<sup>[20]</sup> Along the [111] direction, GaAs is organized as indivisible bi-layers of As–Ga pairs, known as dumbbells. Due to their different electron affinity and the relative position with respect to the (111) surface, each bilayer exhibits an intrinsic electric field, called polarity. Positive (A) and negative (B) polarities correspond to termination by Ga and As, respectively.

Representative aberration-corrected high-angle annular dark-field (HAADF) STEM images of the interface for two NWs observed along the  $[1\bar{1}0]$  zone axis of zinc-blende (ZB) and  $[11\bar{2}0]$  of wurtzite (WZ), with A and B-polarities, are shown in **Figure 1B,C**. We mark the As and Ga atoms in blue and red, respectively. Polarity determination for these NWs is offered in **Figure S1** of the Supporting Information. The A-polar NW

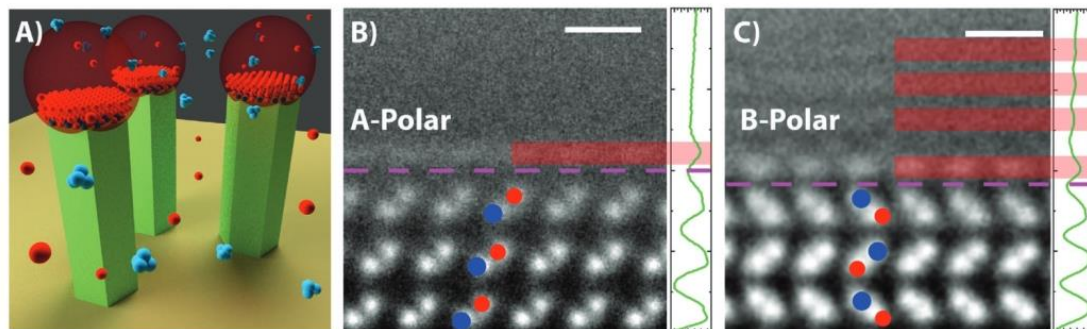


**Figure 1.** Microscopic view of the Ga(l)–GaAs(s) interface. A) Graphic representation of Ga-assisted growth of GaAs NWs: As<sub>4</sub> arrives on the Ga droplet and is dissolved. The Ga atoms at the interface with the GaAs are ordered following the underlying crystalline structure. B,C) HAADF-STEM images of the liquid–solid interface of the A- and B-polar NWs observed along  $[1\bar{1}0]$  ZB and  $[11\bar{2}0]$  WZ zone axes, respectively. The positions of the As and Ga atoms are indicated by the blue and red disks, respectively, as deduced from HAADF intensities. The stacking for the A-polar GaAs is ABCABC, corresponding to the zinc-blende crystal structure, whereas the stacking in the tip of the B-polar NW is ABAB, which is indicative of the wurtzite crystal structure. The right-side panels of (B) and (C) show intensity profiles from the STEM images integrated along the direction parallel to the NW surfaces. The peaks in the intensity correspond to the visually apparent ordered layers in the STEM images, which are in addition highlighted by the overlapping transparent red rectangles. The pink dashed line indicates the position of the interface. The liquid on the B-polar surface exhibits a longer range ordering. The white scale bar on the top left panels of (B) and (C) is 0.5 nm.

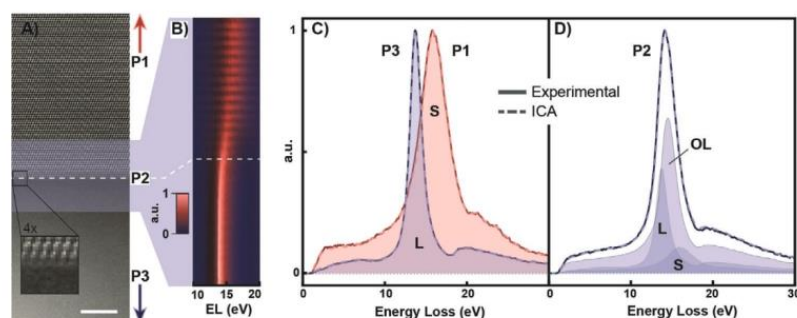


**Figure 2.** EELS analysis of the liquid–solid interface on an A-polar NW. A) Atomic-resolution HAADF image acquired simultaneously with the EELS map. The interface is indicated by the dashed line and the scale bar is 5 nm. The inset shows a magnified view of the interface, where the ordered liquid region is visible. B) Variation in the plasmon peak position close to the interface. C,D) Comparison of EELS measurements (solid lines) with ICA model (dashed curves), and ICA decomposition corresponding to ordered liquid (OL), liquid phase (L), and solid (S) phase. Spectra are extracted from the ZB GaAs (P1), interface (P2), and liquid Ga (P3) regions of the map indicated in panel (A). The color plot and all curves show normalized spectra averaged on horizontal lines of the map.

exhibits a pure ZB structure, whereas the B-polar NW exhibits a mixed-phase structure, finishing with WZ. We attribute this to the change in conditions upon growth termination and the known tendency toward polytypic growth along this polarity.<sup>[5]</sup> Thanks to their intensity dependence on the atomic number as  $\approx Z^{1.7-2}$ , HAADF images provide an easily interpretable and chemically sensitive representation of the structure. As expected, the solid shows strong peaks corresponding to the atomic columns, whereas, further from the interface, the liquid shows a uniform intensity because of its disordered nature. However, close to the interface, the liquid shows intensity fluctuations corresponding to an ordering. For the A-polar interface, this is limited to one additional layer, while several layers are observed for the B-polar interface. This is confirmed in the integrated HAADF intensity profiles shown in the right of panels of Figure 1B,C and we attribute it to a longer-range ordering on top of the B-polar interface. The first layer seems to be more clearly structured, with further layers becoming gradually more amorphous. This is in contrast to the findings by Krogstrup et al.,<sup>[19]</sup> in which the first three layers show similarly strong ordering, with an abrupt reduction in ordering for the fourth layer. One should note that, while high-resolution transmission electron microscopy has been employed before to visualize the ordering of a liquid in contact with a crystalline solid,<sup>[14]</sup> aberration-corrected HAADF-STEM offers a more directly interpretable image contrast, free of both thickness/focus related contrast inversions and delocalization effects. This derives from the incoherent nature of this imaging mode.

We further analyze the liquid–solid interface using EELS hyperspectral mapping to probe the bulk plasmon response around the interface. Being related to the valence/free electron density and characteristics of a material, this technique can discriminate between different chemical/structural phases. Compared to analysis by core-loss EELS or energy dispersive X-ray spectroscopy, the required electron beam dose is orders of magnitude lower, allowing us to apply the technique without destroying the fragile structure of the interface.

Low-loss EELS spectrum images of the interface were recorded using an atomically sized probe. As an example,

Figure 2A shows a HAADF-STEM image acquired simultaneously with the EELS signal from a spectrum image of an A-polar GaAs NW in contact with a Ga droplet. Figure 2B depicts the corresponding spectral evolution integrated across a region of the interface, represented by the blue area shown in Figure 2A.

The bulk plasmon excitation shifts smoothly from a broad peak in the GaAs to a sharper peak in the liquid Ga, over a spatial distance of  $\approx 10$  nm. Intensity oscillations in the GaAs corresponding to the atomic planes are clearly observable due to signal convolution with an elastic scattering contribution. Reference spectra extracted away from the interface at positions deep in the Ga and GaAs phases (marked P1 and P3 in Figure 2A), and a spectrum extracted from the interface (at position P2 in Figure 2A) are presented in Figure 2C,D, respectively. The spectrum at P2 might be assumed to be a linear combination of the contributions of the liquid and solid phases. However, this cannot correctly describe the P2 spectrum: a non-negligible residual is found, as presented in Figure S2 of the Supporting Information. We interpret this residue as the interface contribution. To quantitatively study this interface contribution, we use independent component analysis (ICA), which identifies a finite number of spectral components that can reconstruct the spectrum image.<sup>[22–24]</sup> Although care must be taken when interpreting the components obtained from ICA, it has been successfully applied to unmix independent components in low loss EELS data.<sup>[22]</sup>

Once scaled in intensity, the first two components in our ICA analysis, shown in Figure 2C and labeled S and L, match spectra P1 and P3 well and can be safely interpreted as representing the solid GaAs and liquid Ga components. A third ICA component is also found, which is interpreted as the “ordered liquid” (OL) contribution, dominating the P2 interface signal, see Figure 2D. A reconstruction of the entire dataset using this three-component model shows a negligible residual, demonstrated in Figure S2 of the Supporting Information, confirming that these three components are sufficient to describe the data. This is further emphasized from an analysis of the scree plot in Figure S2 of the Supporting Information, a common tool in multivariate statistical analysis used to identify the number of significant



sources of information in a dataset, which shows that the first three components represent the majority of variations in the spectrum image.<sup>[24]</sup> Considering the confined width of the OL region between GaAs and Ga, combined with the delocalized nature of the plasmon oscillations, the low-loss EELS response of the ordered liquid region cannot be isolated by a direct measurement. While the effect of an ordered liquid region on the overall low-loss EEL spectra of liquid–solid interfaces has been shown previously,<sup>[25]</sup> our use of ICA isolates its response for the first time. A similar analysis of B-polar WZ interfaces is demonstrated in the Supporting Information, leading to an ordered liquid spectral contribution similar to the A-polar component in the range around the plasmon peak. From these results, it is possible to determine a “bulk plasmon” energy for the OL of 14.6 eV (compared to 13.7 and 15.9 eV for Ga and GaAs), with a full width at half maximum (FWHM) of 2.35 eV (compared with 1.95 and 5.3 eV for Ga and GaAs, respectively). Thus, the peak position and FWHM of the plasmon for the OL sit between those of the liquid Ga and solid GaAs. Because of the single, Lorentzian-shaped bulk plasmon peak for each component, the response is consistent with that given by the Drude model, in which the peak position and its FWHM can be linked to the free electron density,  $n$ , and its damping constant,  $\Gamma$ .<sup>[26]</sup> The results indicate that both  $n$  and  $\Gamma$  decrease from the solid GaAs through the ordered liquid to the liquid Ga. The extent of damping depends on the lattice and band structure. For instance, damping can be caused by the transfer of energy from the plasmon resonance to single-electron transitions (i.e., creation of  $e^-h^+$  pairs). Conversely, the closer the electronic nature of a material approximates a free electron gas, the smaller the damping constant is. It is therefore logical that the solid semiconducting GaAs NW has a larger  $\Gamma$  than the metallic liquid Ga, since the lattice and band structure of the former will increase the probability of energy transfer to single electron transitions. A similar difference is seen between semiconducting Si and metals such as Al.

From this analysis, one can conclude that the ordered liquid has a distinct electronic nature, which can intuitively be correlated with its semistructured nature. Considering this and given the fact that the ordered liquid cannot exist as a bulk phase outside of the interface, we propose that it can be considered as an interfacial complex.<sup>[27–29]</sup> The existence of complexation could have profound consequences for crystal growth. To understand this, the 3D nature of the ordering and the influence of the polarity on its structure are key aspects, which we shall address next.

We now investigate the nature of the ordering using MD simulations. For this purpose, we use the 2D projection of the structure in STEM imaging to validate the MD results.

Given the size and time scales needed for these simulations, brute-force *ab initio* MD is prohibitively expensive. To circumvent this, we have trained a neural network potential (NNP)<sup>[30,31]</sup> based on a relatively small number of reference density functional theory (DFT) calculations.<sup>[32,33]</sup> Then, we have used this machine-learning model to drive the dynamics.<sup>[31,34]</sup> MD details in addition to the calculations and validation of the NN based on a multiple-timestep integration<sup>[35,36]</sup> are discussed in the Supporting Information.

Figure 3A,B compare the projected linear density obtained across the simulation cell with intensity line profiles derived

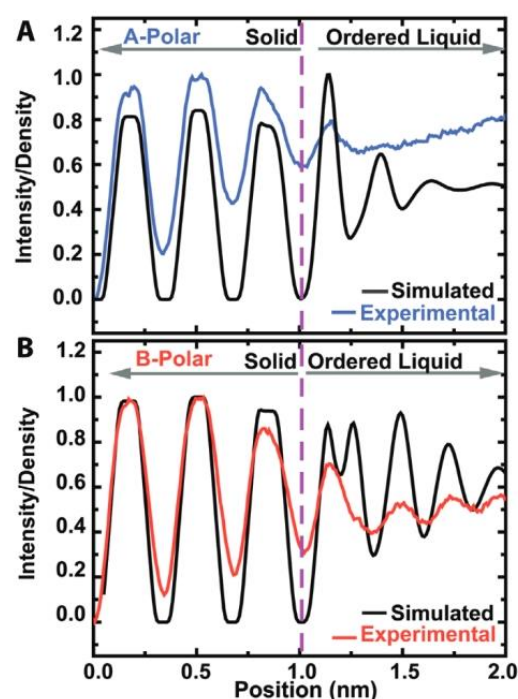


**Figure 3.** Comparison of intensity/mean atom density profiles from experimental STEM and MD simulations. The ZB A-polar and WZ B-polar interfaces are demonstrated in (A) and (B), respectively. The dashed pink line indicates the interface position.

from experimental images for A- and B-polar cases, respectively. For any given polarity, simulations do not show significant differences in the liquid ordering with respect to the ZB or WZ solid phases. The experimental curves are obtained by projecting the intensity profiles from Figure 1B,C along the axis normal to the surface. In the solid, we obtain regularly ordered peaks at the positions of the dumbbells. The liquid also exhibits some peaks in the density profile, characteristic of atomic-level ordering. The range of the ordering is different for the two polarities. As noted earlier, in STEM images, while the B-polar order is observed for four layers, it does not extend beyond the first layer for the A-polar case. Similar to the experimental observations, the simulations show that the ordering gradually diminishes when the distance from the crystalline phase is increased, which is in contrast to the conclusions given by Algra et al.<sup>[19]</sup> for InP in contact with liquid InAu. This tendency correlates well with the simulations, which show that the in-plane order of the A-polar case is more diffuse than that of B-polar, as demonstrated in Figure S6 of the Supporting Information. Note that an exact correlation of the projected linear density obtained from the simulations with the HAADF-STEM integrated intensities is not expected: although the latter scales approximately with the former, a full quantum mechanical image simulation using the atomistic model derived from MD would be necessary for a quantitative comparison.

The key observation, however, is that there is a quantitative match between the MD predictions of the spacing between ordered layers with the experimental observations. This is demonstrated in Table S3 of the Supporting Information, in which the experimental observations and MD predictions of the spacing between ordered layers are compared for a B-polar interface. We therefore conclude that MD based on the NNP correctly predicts the nature of the liquid ordering.

The 3D representations from the simulations indicate that the order in the liquid extends fully within the plane parallel to the interface, as illustrated in Figure S6 of the Supporting Information, consistent with the fact that this order is visible in HAADF images. One interesting observation is that contrary to what is assumed by Algra et al.,<sup>[19]</sup> the spacings between consecutive ordered liquid layers are not identical. As clear from Table S3 of the Supporting Information, these layers gradually become closer to each other as the distance from the crystalline solid is increased. We further find that the order at the liquid–solid interface is dominated by the tendency of Ga atoms to form Ga–Ga pairs. Ga atoms form pairs with the solid when the surface is Ga-terminated, while it forms Ga–Ga pairs in the liquid when the solid is As-terminated. This tendency for dimerization is well-known in liquid Ga, which is often referred to as a molecular metal.<sup>[37]</sup> We should note that besides this remarkable ordering at the liquid–solid interface, the liquid remains a liquid as the position of the atoms is dynamic and thus varies with time. In Figure S19 of the Supporting Information, we provide a comparison of the Ga–Ga radial pair distribution functions of the solid, liquid, and interface phases as an illustration.

The simulations shown previously were performed at 300 K, corresponding to the temperature used to acquire the STEM images. To make the link with the growth process, we performed the same simulations at the growth temperature (900 K). **Figure 4** depicts the ordering of the interface at 900 K for both polarities where the spatial variation in the Ga atomic density is indicated by red isosurfaces. Figure 4A depicts a 3D view of

the ensemble for a B-polar WZ solid in contact with liquid Ga. Figure 4B provides top and side views for the A- and B-polar solids. In both cases, we find ordering within the plane, however with significant differences in the arrangement of Ga atoms as a function of the polarity.

On the B-polar surface, Ga is adsorbed right on top of the terminal As. This is consistent with the large electronegativity difference between As and Ga that is likely to induce strong electrostatic interactions. In-plane ordering is also present at the A-polar surface. Here, instead, Ga atoms in the liquid pair with the terminal Ga atoms in the solid, consistent with the dimerization tendency of Ga. As expected, at the higher temperature, the range of the order has decreased relative to observations at 300 K, with simulations indicating the presence of at most one ordered layer on top of the solid. Most of the qualitative features of the liquid ordering, however, are preserved between the two temperatures, suggesting that experiments performed at 300 K can provide insights into the relevant mechanisms for growth at higher temperatures.

We move now to the microscopic picture of GaAs growth. Any new layer of GaAs forms new Ga–As pairs. Ga and As atoms are shown in red and blue in Figure 4, while the positions leading to ZB and WZ configurations are indicated by squares and hexagons, respectively. The inclined dashed lines provide a guide to define the atomic positions that lead to the relevant crystalline structures in Figure 4B,C. In the A-polar case, As must displace and occupy the position of ordered Ga in the liquid, with which it may form a dumbbell. The Ga atoms have two choices, as indicated in Figure 4 by the square and hexagon. Depending on the position selected, ZB (ABCABC stacking) or a twin (ABA stacking) is formed. These two positions are not equivalent in terms of their first and second nearest neighbors configuration. In the ABC stacking, Ga is found at the middle of a projected hexagon, while in the ABAB it is at a vertex. Further calculations beyond the scope of this work should corroborate if there is a position that is more energetically favorable. Still, to form a new bilayer, As

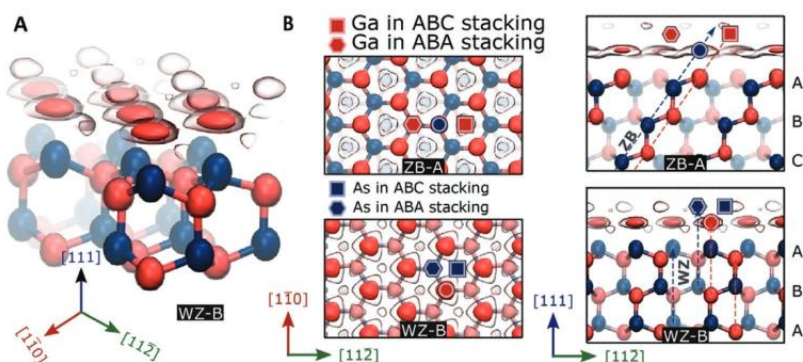


**Figure 4.** Simulations of the Ga(l)–GaAs(s) interface at 900 K. Isocontours of the Ga atom density, showing order at the liquid–Ga/GaAs interface—corresponding to density  $\rho = 0.11 \text{ Bohr}^{-3}$  (opaque) and  $\rho = 0.06 \text{ Bohr}^{-3}$  (translucent). As and Ga atoms are drawn in blue and red, respectively. Objects further from the viewer are represented with less contrast as a depth cue. A) 3D view of WZ GaAs terminated with B-polarity; B) views along the  $[111]$  (left) and  $[1\bar{1}0]$  ZB/ $[11\bar{2}0]$  WZ (right) directions; in the case of A-polar ZB and B-polar WZ (top and bottom, respectively). Similar isocontours presented for simulations at 300 K in the Supporting Information. We indicate the positioning of the As and Ga atoms that are required to create a new Ga–As bilayer, taking the isocontours and the underlying structure as the canvas.



atoms should first displace the ordered Ga layer on top of the NW, and this should increase the formation barrier. This is consistent with the difficulty in synthesizing A-polar GaAs NWs,<sup>[5,21]</sup> suggesting that the slower process may help the growing layer achieve the more thermodynamically stable ABC stacking.

The associated low probability of twinning also reduces the probability of WZ formation, as both are closely connected.<sup>[38]</sup> Experimentally, the A-polar GaAs NWs exhibit mostly a ZB structure with an absence of transverse twins.<sup>[5,21]</sup>

During the formation of a new bilayer for the B-polar surface, the Ga atoms adsorbed on top of the As-terminated surface can stay at their position. The incoming As atoms occupy empty positions in the second row. The fact that the growth can proceed without displacing Ga atoms is consistent with the observation of a more facile growth for this polarity. The higher growth rate can also partly explain the higher propensity to introduce stacking defects and polytypism in B-polar GaAs NWs.<sup>[5]</sup> These results could explain why in polar semiconductors, growth in a certain polarity is preferred and how polarity determines the tendency for polytypism.

In conclusion, we have demonstrated that interfaces between a solid GaAs NW and the liquid Ga droplet exhibit a 3D order that depends on the polarity of the solid and the temperature. This order can be explained by the electrostatic interactions within the liquid and the solid termination. Detailed simulations of the interface, enabled by the combination of first-principles calculations and machine-learning, provide an atomistic picture of the growth process from the liquid, the likelihood for growth in a certain polarity and defect formation. This work lays the foundations for further atomistic studies of crystal growth processes. While our results have been obtained for the Ga(l)–GaAs(s) system, we believe they are of a general character. Similar ordering features likely play an important role in the crystal growth of other materials and in more general solidification processes, raising new questions for groups observing NW growth by in situ electron microscopy. This work also opens analogous perspectives in other fields such as catalysis and (photo)electrochemistry.

## Experimental Section

**NW Growth:** GaAs NWs were grown on GaAs (100) substrates as described by Zamani et al.<sup>[21]</sup> HF etching was used to remove the substrate native oxide. Silicon oxide layers were obtained by spin-coating a solution of hydrogen silsesquioxane and methyl isobutyl ketone. The spin-coated layers were annealed at 300 °C for 10 min. The oxide thicknesses used for the growth was around 3.3 nm. Two additional annealing steps at 150 and 300 °C, lasting 2 h each were performed inside the MBE chamber. The growth conditions for the NWs were: a V/III ratio of 1.9, equivalent 2D Ga-limited GaAs growth rate of 0.24 Å s<sup>−1</sup>, at a substrate temperature of 640 °C.

**HAADF-STEM Imaging:** The STEM samples were prepared by scraping as-grown samples onto Cu TEM grids with amorphous holey carbon films. The STEM imaging was performed using a double aberration-corrected FEI Titan Themis 60–300, operated at 300 kV high tension (HT). To minimize both electron-beam induced damage to the interface and scan distortions from, e.g., sample drift, the HAADF-STEM images were acquired as 24-frame image series, which were then averaged while correcting for rigid and nonrigid displacements using

the SmartAlign plug-in for DigitalMicrograph.<sup>[39]</sup> Consecutive frames were acquired at a 90° rotations using a low beam current (<40 pA). The electron probe convergence semiangle and HAADF detector inner collection semiangles were 20 and 50.5 mrad. Fischione photomultiplier tube was used as the HAADF detector. Pixel dwell time of 0.5 μs and pixel step size ≈6 pm were employed. The images were captured with 2k × 2k size.

**EELS Hyperspectral Imaging:** The data were acquired with the same microscope, HT and probe convergence semiangle, using a Gatan GIF Quantum ERS spectrometer with Ultrascan 2k × 2k detector. In order to avoid damaging the interface, the probe current was set to 75 pA and a scan step size of ≈0.9 Å was applied. The energy dispersion was set to 0.05 eV per ch, while the zero-loss peak FWHM was 1.05 eV. A spectrometer entrance aperture of 2.5 mm, corresponding to a collection semiangle of 47 mrad was employed. For the measurements on the A-polar NW discussed in Figure 2 and in the Supporting Information, per spectrum pixel time was 0.25 ms, while this value was 0.5 ms for the measurement on B-polar NW reported in the Supporting Information. For all the EELS data, detector was binned by 130× on nondispersive axis and it was operating in high speed mode. “High quality dark correction” was applied. Processing the data started with removing spectral spikes from cosmic rays, centering the zero-loss peak to compensate for HT fluctuations and removing it, removing plural scattering and the plasmon peak replica. Then, second-order ICA was performed using the DigitalMicrograph plugin described by Lucas et al.,<sup>[24]</sup> details of which are presented in the Supporting Information.

**Molecular Dynamics:** To investigate the ordering at the interface at the two (111) surfaces, an orthorhombic supercell composed of a central solid GaAs section (144 atoms, corresponding to 6 layers of 24 atoms), in contact with liquid Ga (192 atoms) on both of its surfaces, totaling 336 atoms, was used.

The initial lattice parameter for the solid part was set to the one obtained from DFT calculations, whereas the initial density of liquid Ga was set to that obtained with independent simulations in a smaller (96 atoms) box at the objective temperature. All the simulations were run using i-PI<sup>[36]</sup> in combination with large-scale atomic/molecular massively parallel simulator,<sup>[34]</sup> and n2p2<sup>[37]</sup> to evaluate the NNP. First, the system was equilibrated in the NVT ensemble, allowing the cell degrees of freedom to change independently. After equilibration, production simulations were run in the NVT ensemble, using the average lattice parameters, at the temperatures indicated in the text.

The temperatures were controlled using a combination of a generalized Langevin<sup>[40]</sup> and stochastic velocity rescaling<sup>[41]</sup> thermostats. Pressures, where applicable, were constrained using an anisotropic barostat.<sup>[42]</sup>

Simulations were run with a timestep of 4 fs (at 300 K) and 2 fs (at 900 K), for a total of 10 ns.

**Neural Network and Ab Initio Calculations:** A neural network potential of the Behler–Parrinello kind<sup>[30]</sup> was trained to reproduce the results obtained with DFT calculations. A total of 970 structures were used to fit the potential, with a 90/10 split between training and test. At the end of the training procedure, the average error in the test set was 2.4 meV per atom for energies and 120 meV Å<sup>−1</sup> for forces.

The DFT calculations were carried out with the plane-wave code Quantum-Espresso,<sup>[32]</sup> using the Perdew–Burke–Ernzerhof exchange–correlation functional,<sup>[43]</sup> and ultrasoft pseudopotentials<sup>[33]</sup> from the SSFP library (version 0.7).<sup>[44]</sup>

The wavefunction energy cutoff was set to 50 Ry for all calculations, whereas the kinetic energy cutoff was set to 400 Ry.

Energy and forces for the structures used as training points were computed with a converged (<1 meV per atom absolute convergence) 3 × 3 × 1 Monkhorst–Pack k-point grid.<sup>[45]</sup>

## Supporting Information

Supporting Information is available from the Wiley Online Library or from the author.

## Acknowledgements

M.Z., N.T., and A.F.i.M. were supported by SNF Back-Up Schemes Consolidator Grant Nos. BSC-G10\_157705 and NCCR QSIT, G.I. and M.C. were supported by the NCCR MARVEL, funded by the Swiss National Science Foundation. ICN2 acknowledges funding from Generalitat de Catalunya 2017 SGR 327 and the Spanish MINECO project ENE2017-85087-C3. ICN2 was supported by the Severo Ochoa program from Spanish MINECO (Grant No. SEV-2017-0706) and was funded by the CERCA Programme/Generalitat de Catalunya. Part of the present work was performed in the framework of Universitat Autònoma de Barcelona Materials Science Ph.D. program. S.M.-S. acknowledges funding from "Programa Internacional de Becas 'la Caixa'-Severo Ochoa." The authors acknowledge support from CSIC Research Platform on Quantum Technologies PTI-001. SuperSTEM is the UK National Research Facility for Advanced Electron Microscopy, supported by the Engineering and Physical Sciences Research Council (EPSRC).

## Conflict of Interest

The authors declare no conflict of interest.

## Author Contributions

M.Z. and G.I. contributed equally to this work. The samples were grown by M.Z. The STEM images and EELS data were captured by D.T.L.A. Processing of STEM images was done by M.Z. M.Z. and N.T. performed the analysis of EELS spectra and the application of ICA. D.T.L.A. and C.H. helped with discussions on the application of ICA and its results. MD simulations were done by G.I. and S.B. under the supervision of M.C., M.Z., N.T., L.F., and G.I. made the figures. S.M.-S., Q.M.R., and J.A. contributed to the discussions on the electron microscopy aspects of this research and obtained complementary STEM images and EELS spectra. M.Z. and G.I. made the Supporting Information section. The manuscript was mainly written by A.F.i.M., N.T., and M.C. For discussion on implications of results on NW growth, M.Z., M.F., L.G., G.T., L.F., G.I., M.C., and A.F.i.M. had input. G.T. and A.F.i.M. proposed and conceptualized the idea. M.Z. and A.F.i.M. coordinated the collaboration between different groups. A.F.i.M. directed the work. All the authors have contributed to the correction and proofreading.

## Keywords

liquid ordering, liquid–solid interface, nanowires

Received: February 13, 2020

Revised: June 29, 2020

Published online: August 6, 2020

- [1] R. S. Wagner, W. C. Ellis, *Appl. Phys. Lett.* **1964**, *4*, 89.
- [2] C. Y. Wen, J. Tersoff, M. C. Reuter, E. A. Stach, F. M. Ross, *Phys. Rev. Lett.* **2010**, *105*, 195502.
- [3] J. C. Harmand, G. Patriarche, F. Glas, F. Panciera, I. Florea, J. L. Maurice, L. Travers, Y. Ollivier, *Phys. Rev. Lett.* **2018**, *121*, 166101.
- [4] F. Glas, J. C. Harmand, G. Patriarche, *Phys. Rev. Lett.* **2007**, *99*, 146101.
- [5] X. Yuan, P. Caroff, J. Wong-Leung, L. Fu, H. H. Tan, C. Jagadish, *Adv. Mater.* **2015**, *27*, 6096.
- [6] R. R. Zamani, S. Gorji Ghalamestani, J. Niu, N. Sköld, K. A. Dick, *Nanoscale* **2017**, *9*, 3159.

- [7] D. Jacobsson, F. Panciera, J. Tersoff, M. C. Reuter, S. Lehmann, S. Hofmann, K. A. Dick, F. M. Ross, *Nature* **2016**, *531*, 317.
- [8] L. Ghisalberti, H. Potts, M. Friedl, M. Zamani, L. Güniat, G. Tütüncüoğlu, W. C. Carter, A. F. I. Morral, *Nanotechnology* **2019**, *30*, 285604.
- [9] P. Krogstrup, H. I. Jørgensen, E. Johnson, M. H. Madsen, C. B. Sørensen, A. F. I. Morral, M. Aagesen, J. Nygård, F. Glas, *J. Phys. D: Appl. Phys.* **2013**, *46*, 313001.
- [10] V. G. Dubrovskii, *Cryst. Growth Des.* **2017**, *17*, 2544.
- [11] J. Q. Broughton, G. H. Gilmer, *J. Chem. Phys.* **1983**, *79*, 5095.
- [12] H. E. A. Huitema, M. J. Vlot, J. P. Van Der Eerden, *J. Chem. Phys.* **1999**, *111*, 4714.
- [13] S. Toxvaerd, *Faraday Symp. Chem. Soc.* **1981**, *16*, 159.
- [14] S. H. Oh, Y. Kauffmann, C. Scheu, W. D. Kaplan, M. Rühle, *Science* **2005**, *310*, 661.
- [15] M. Gandman, Y. Kauffmann, W. D. Kaplan, *Appl. Phys. Lett.* **2015**, *106*, 051603.
- [16] Y. Kauffmann, S. H. Oh, C. T. Koch, A. Hashibon, C. Scheu, M. Rühle, W. D. Kaplan, *Acta Mater.* **2011**, *59*, 4378.
- [17] O. G. Shpyrko, R. Streitel, V. S. K. Balagurusamy, A. Y. Grigoriev, M. Deutsch, B. M. Ocko, M. Meron, B. Lin, P. S. Pershan, *Science* **2006**, *313*, 77.
- [18] T. U. Schüll, R. Daudin, G. Renaud, A. Vaysset, O. Geaymond, A. Pasturel, *Nature* **2010**, *464*, 1174.
- [19] R. E. Algra, V. Vonk, D. Wermeille, W. J. Szewern, M. A. Verheijen, W. J. P. Van Enkevort, A. A. C. Bode, W. L. Noorduyn, E. Tancini, A. E. F. De Jong, E. P. A. M. Bakkers, E. Vlieg, *Nano Lett.* **2011**, *11*, 44.
- [20] C. Colombo, D. Spirkoska, M. Frimmer, G. Abstreiter, A. Fontcuberta, I. Morral, *Phys. Rev. B* **2008**, *77*, 155326.
- [21] M. Zamani, G. Tütüncüoğlu, S. Martí-Sánchez, L. Francaviglia, L. Güniat, L. Ghisalberti, H. Potts, M. Friedl, E. Markov, W. Kim, J. B. Leran, V. G. Dubrovskii, J. Arbiol, A. Fontcuberta I Morral, *Nanoscale* **2018**, *10*, 17080.
- [22] N. Bonnet, D. Nuzillard, *Ultramicroscopy* **2005**, *102*, 327.
- [23] F. de la Peña, M. H. Berger, J. F. Hochepeid, F. Dynys, O. Stephan, M. Walls, *Ultramicroscopy* **2011**, *111*, 169.
- [24] G. Lucas, P. Burdet, M. Cantoni, C. Hébert, *Micron* **2013**, *52–53*, 49.
- [25] M. Gandman, Y. Kauffmann, W. D. Kaplan, *Appl. Phys. Lett.* **2015**, *106*, 051603.
- [26] R. F. Egerton, *Electron Energy-Loss Spectroscopy in the Electron Microscope*, Springer, USA **2011**.
- [27] W. D. Kaplan, D. Chatain, P. Wynblatt, W. C. Carter, *J. Mater. Sci.* **2013**, *48*, 5681.
- [28] M. Tang, W. C. Carter, R. M. Cannon, *Phys. Rev. B: Condens. Matter Mater. Phys.* **2006**, *73*, 024102.
- [29] S. J. Dillon, M. Tang, W. C. Carter, M. P. Harmer, *Acta Mater.* **2007**, *55*, 6208.
- [30] J. Behler, M. Parrinello, *Phys. Rev. Lett.* **2007**, *98*, 146401.
- [31] A. Singraber, T. Morawietz, J. Behler, C. Dellago, *J. Chem. Theory Comput.* **2019**, *15*, 3075.
- [32] P. Giannozzi, O. Andreussi, T. Brumme, O. Bunau, M. Buongiorno Nardelli, M. Calandra, R. Car, C. Cavazzoni, D. Ceresoli, M. Cococcioni, N. Colonna, I. Carnimeo, A. Dal Corso, S. De Gironcoli, P. Delugas, R. A. Distasio, A. Ferretti, A. Floris, G. Fratesi, G. Fugallo, R. Gebauer, U. Gerstmann, F. Giustino, T. Gorni, J. Jia, M. Kawamura, H. Y. Ko, A. Kokalj, E. Küçükbenli, M. Lazzeri, M. Marsili, N. Marzari, F. Mauri, N. L. Nguyen, H. V. Nguyen, A. Otero-De-La-Roz, L. Paulatto, S. Poncè, D. Rocca, R. Sabatini, B. Santra, M. Schlipf, A. P. Seitsonen, A. Smogunov, I. Timrov, T. Thonhauser, P. Umari, N. Vast, X. Wu, S. Baroni, *J. Phys. Condens. Matter* **2017**, *29*, 465901.
- [33] D. Vanderbilt, *Phys. Rev. B* **1990**, *41*, 7892.
- [34] S. Plimpton, *J. Comput. Phys.* **1995**, *117*, 1.
- [35] M. Tuckerman, B. J. Berne, G. J. Martyna, *J. Chem. Phys.* **1992**, *97*, 1990.



- [36] V. Kapil, M. Rossi, O. Marsalek, R. Petraglia, Y. Litman, T. Spura, B. Cheng, A. Cuzzocrea, R. H. Meißner, D. M. Wilkins, B. A. Helfrecht, P. Juda, S. P. Bienvenue, W. Fang, J. Kessler, I. Poltavsky, S. Vandenbrande, J. Wieme, C. Corminboeuf, T. D. Kühne, D. E. Manolopoulos, T. E. Markland, J. O. Richardson, A. Tkatchenko, G. A. Tribello, V. Van Speybroeck, M. Ceriotti, *Comput. Phys. Commun.* **2019**, 236, 214.
- [37] W. J. Hulsman, J. F. Peters, M. J. Zwanenburg, S. A. De Vries, T. E. Derry, D. Abernathy, J. F. Van der Veen, *Nature* **1997**, 390, 379.
- [38] J. Arbiol, A. Fontcuberta I Morral, S. Estradé, F. Peiró, B. Kalache, P. Roca I Cabarrocas, J. R. Morante, *J. Appl. Phys.* **2008**, 104, 064312.
- [39] L. Jones, H. Yang, T. J. Pennycook, M. S. J. Marshall, S. Van Aert, N. D. Browning, M. R. Castell, P. D. Nellist, *Adv. Struct. Chem. Imaging* **2015**, 1, 8.
- [40] M. Ceriotti, G. Bussi, M. Parrinello, *J. Chem. Theory Comput.* **2010**, 6, 1170.
- [41] G. Bussi, D. Donadio, M. Parrinello, *J. Chem. Phys.* **2007**, 126, 014101.
- [42] P. Raiteri, J. D. Gale, G. Bussi, *J. Phys. Condens. Matter* **2011**, 23, 334213.
- [43] J. P. Perdew, K. Burke, M. Ernzerhof, *Phys. Rev. Lett.* **1996**, 77, 3865.
- [44] G. Prandini, A. Marrazzo, I. E. Castelli, N. Mounet, N. Marzari, *npj Comput. Mater.* **2018**, 4, 72.
- [45] H. J. Monkhorst, J. D. Pack, *Phys. Rev. B* **1976**, 13, 5188.



## 4: Conclusion and Outlook

In this thesis, we have looked at crystalline order of compound semiconductors and the way the interface control can lead to higher crystalline quality. In particular, we have focused on two different material systems, *GaAs* NWs and  $Zn_3P_2$  thin films.

In publication 1, the delicate liquid ordering at the interface of self-catalyzed *GaAs* NWs and their *Ga* droplet is investigated using a combination of experimental methods and simulations. First, HAADF-STEM imaging is employed to shed light on the atomistic differences between the interfaces of A and B-polar NWs with their catalyst *Ga* droplet. It is observed that A-polar interface exhibits just one layer of liquid ordering, which is in contrast to the behavior of the B-polar interface in which four layers of ordering perpendicular to the interface is formed. The thickness of this ordered regions is extremely low and it can reach up to 1 nm in the B-polar case. This is the first experimental confirmation of atomistic difference in the liquid ordering of A-polar and B-polar interfaces in VLS-grown *GaAs* NWs.

Employing low-loss EELS, it is then proved that these ordered liquid regions have their own distinct functional properties. Due to the delocalized nature of plasmonic oscillations and the extremely small thickness of these ordered liquid regions, it is not possible to directly measure their low-loss EELS spectra. Instead, we have used independent component analysis to unmix the spectra and extract the low-loss signature of the ordered liquid layer. This approach is very generalizable and can be applied to other interfaces, too.

In order to have a better understanding of the structural differences of A and B-polar interfaces, machine learning-based molecular dynamics simulations are used. In contrast to electron microscopy, these simulations have the benefit of offering a 3D image of the ordered liquid region and the interface. First, the results of the simulations are cross validated against the experimental observations, and great agreement is observed. The differences in the ordering between A-polar and B-polar interface is then used to explain the vastly different growth behavior of A-polar and B-polar interfaces. For A-polar growth, it is observed that first *As* atoms need to displace the ordered *Ga* layer on top of the interface, which adds a barrier to the growth and can explain the overall difficulty in the growth of A-polar NWs. On the other hand, new monolayers of *GaAs* can readily form in the B-polar case if new *As* atoms are just absorbed on top of the existing ordered *Ga* layer. No displacement of ordered *Ga* atoms is needed, which can explain the more facile growth of this polarity. The higher growth rate could also be used to partly explain the tendency of B-polar NWs to have a defective structure: the faster growth process does not allow the more thermodynamically stable ABC stacking to be perfectly achieved. The results of this study help explain why in polar semiconductors, growth in a certain polarity is preferred and how the polarity can determine the propensity for polytypism.

Future works on this topic can be explored in many different directions. Experimentally, using a monochromated electron beam to study the EELS spectra of the ordered liquid region can shed light on the details of the functional properties of these layers, including information on its band structure. The spectral features that can be useful for such studies are eliminated in this work due to the large energy spreading of the beam and the resulting data processing steps.

In order to better approximate the growth conditions, high-temperature holders can be used, which can increase the temperature of TEM grid inside the TEM chamber. This will enable us to study the variations in the structure and the EELS spectra of the ordered regions. Assessing such changes can

help establish the complexion transformations for the ordered liquid, which provide unprecedented fundamental understanding of the growth mechanism of the NWs.

As discussed in chapter 1 of this thesis, current models proposed for the VLS growth of NWs ignore the atomistic structure of the interface, which, as demonstrated here, has its own distinct properties and can help explain the growth behavior of semiconductor NWS. Models that explicitly consider the ordered interface are therefore needed to gain a better understanding of NW growth, which will enable us to have a better control over the properties of the wires.

The dynamic behavior of the ordering during the growth is what fundamentally determines the structure of the NWS. To study such behavior, in-situ TEM of NW growth can be conducted with a focus on the changes in the ordering during the growth. In particular, it would be interesting to see how the ordering is perturbed when a defect is formed in the structure of the NWs.

Furthermore, the link between the microscopic ordering and the macroscopic growth behavior such as droplet contact angle can be established. It is now known that, during *GaAs* NW growth, higher As fluxes result in lower contact angles, formation of WZ and a tendency for increased defectiveness. However, the atomistic picture of such change and its reasons are lacking now, which limits our fundamental understanding of NW growth.

The procedure developed here for the experimental study of the liquid-solid interfaces is easy to apply to other systems. In particular, it will be interesting to investigate the interface in the gold-catalyzed growth of *GaAs* NWs and observe the differences it has with the self-catalyzed case of NW growth. This could help understand the relative ease of control in the gold-catalyzed growth of NWs.

Finally, further MD studies can provide us with information that is otherwise impossible to acquire with experimental methods. Energy calculations for different ordering in hexagonal and cubic configurations, which are responsible for WZ and ZB growth, respectively, can shed light the polytypism and defecting properties of different interface polarities. In addition, new simulations can shed light on the changes in the ordering as a function of growth parameters. In particular, it would be interesting to see how an increase in the number of As atoms present in the liquid Ga phase can change the ordering behavior and link that to the experimental observation about the role of  $V/III$  ratio on the growth of NWs.

In publication 2, we have focused on the growth of thick high-quality and defect-free  $Zn_3P_2$  thin films. This is an important step in realization of the potential of this material for large-scale and cheap photovoltaic applications.

First, the effects of changing the growth parameters, such as  $V/II$  ratio and temperature on the crystalline quality of the thin films are studied by Raman spectroscopy. It is observed that high growth temperatures and  $V/II$  ratios favor amorphous films. Polycrystalline films with increased granularity are observed when using lower temperatures and  $V/II$  ratios.

Careful engineering of the atomistic nature of the substrate-thin film interface is carried out as a way to improve the quality of the films. Native oxide removal with high-temperature in-situ degassing is proven to be an effective way for growing monocrystalline films. These monocrystalline films have a very sharp interface with the substrate, and the transition from *InP* to  $Zn_3P_2$  happens via the formation of a mixed *Zn/In* monolayer at the interface. On the other hand, core-loss EELS studies reveal that the polycrystalline thin films have an oxygen-containing interfacial layer at their interface with the substrate, which hinders the epitaxial relationship between the film and the substrate and is the cause

of the polycrystallinity. Structurally, these films have a high concentration of small grains at their interface with the substrate, which gradually merge as the growth continues and result in a columnar structure.

XRD is employed to further shed light on the differences of polycrystalline and monocrystalline films, which indicate that the monocrystalline films grow in [001] direction. On the other hand, multiple high order peaks are observed in the XRD pattern of the polycrystalline films, which is consistent with their structure.

Finally, the functional properties of the films are studied by low-temperature PL. There is a variation in the emission of polycrystalline samples both between different polycrystalline samples. In addition, within the same sample, the optical emission is location-dependent. This is due to the fact that the optical behavior of polycrystalline samples is highly dependent on the local defect properties, which are likely to change according to the probing position. Interestingly, the bandgap emission from  $Zn_3P_2$  is absent on the polycrystalline samples. On the other hand, the monocrystalline samples offer a more uniform and consistent emission. While the emission from the *InP* substrate is still observed on these films, there is a pronounced contribution from bandgap emission, further demonstrating the superior properties of the monocrystalline films.

Up to now, the material properties reported by the different teams for  $Zn_3P_2$  have been vastly different, which is a result of the differences in the defect concentration and the stoichiometric properties of the films. Given the establishment of a robust method for a reproducible growth of monocrystalline thin films, the future studies on  $Zn_3P_2$  should be focused on turning the functional properties of these films. In particular,  $Zn_3P_2$  is prone to uncontrolled intrinsic p-doping. However, the extensive control provided by MBE could be exploited to fine-tune the stoichiometry of  $Zn_3P_2$  thin films and eliminate/limit the p-doping. This is a fundamentally important step for formation of an efficient junction for photovoltaic applications. Controlling the intrinsic p-doping will enable the researchers to employ extrinsic p-doping with very high degree of precision, an important step that will enable effective junction tuning.

In addition, the experimentally reported mobility and carrier diffusion length for  $Zn_3P_2$ , while higher than materials such as *GaAs*, are still far from the predicted theoretical values. This is because monocrystalline  $Zn_3P_2$  films before have been grown only for very low thicknesses, which makes them prone to the extensive contribution of surface effects that reduce the mobility of carriers. Mobility measurement of polycrystalline samples grown with different conditions can help optimize the properties of  $Zn_3P_2$  films.

After the optimization of the properties of the films, junction formation between the p-doped  $Zn_3P_2$  and the candidate n-doped layers can be study in depth. Prototype photovoltaic cells can be made to study the performance of  $Zn_3P_2$  as absorber in solar cells.





# Appendix A: Supporting information

© 2020 Wiley-VCH GmbH

**ADVANCED  
MATERIALS**

## Supporting Information

for *Adv. Mater.*, DOI: 10.1002/adma.202001030

### 3D Ordering at the Liquid–Solid Polar Interface of Nanowires

*Mahdi Zamani, Giulio Imbalzano, Nicolas Tappy, Duncan  
T. L. Alexander, Sara Martí-Sánchez, Lea Ghisalberti,  
Quentin M. Ramasse, Martin Friedl, Gözde Tütüncüoğlu,  
Luca Francaviglia, Sebastien Bienvenue, Cécile Hébert, Jordi  
Arbiol, Michele Ceriotti,\* and Anna Fontcuberta i Morral\**

## Supporting Information

### S1. Electron Microscopy Study of Liquid-Solid interface

#### S1.1 Polarity Determination for NWs:

Polarity determination for NWs shown in Figure 1 is offered in **Figure S1**. The two NWS are depicted in Figure S1a and S1b. The zoomed-in version of these images are offered in Figure S1c and S1d. The HAADF intensity profile for the green arrows in these figures are plotted in Figure S1e and S1f. Given the fact that the HAADF intensities are proportional to  $Z^{1.7}$ , heavier atoms will appear brighter in these images. From Figure S1e and S1f, we conclude that the dumbbells in Figure S1a and S1b are terminated by Ga and As, respectively. This indicates that these NWs are indeed of A and B-polarity, respectively.

#### S1.2 EELS Study of the Liquid-Solid Interface and application of the ICA

More details on the application of ICA on the EELS measurements are provided in **Figure S2**. Figure S2a shows an atomic-resolution HAADF image acquired simultaneously with the EELS map for a Ga droplet in contact with an A-polar GaAs NW. Figure S2b represents as a color map the plasmon peak energy for this interface, ranging from 13.7 eV in the liquid Ga to 15.9 eV in the GaAs crystal.

Figure S2c shows in bar histogram form the so-called logarithmic screeplot of the principal component analysis (PCA) carried out on the EELS hyperspectral dataset. This plot is widely used in multivariate statistical analysis to determine how many factors (also called components, or sources of information) must be used for dataset reconstruction. The steep part of this curve on its left corresponds to the components that contribute to meaningful variations in the data, while from component 4 onwards, the curve becomes linear indicating these correspond to noise or non-

significant data <sup>[1]</sup>. Therefore, the ICA analysis presented here considered only the first three components.

As a further criterion to judge whether or not three components can adequately be used to reconstruct the EELS maps, the normalized residues of multiple linear least square (MLLS) fit for two cases as a function of position are provided in Figure S2d. In the first case, EEL spectra from the liquid Ga and solid GaAs are used as the reference spectra for the fitting (2-component fit), while in the second case, EEL spectra from liquid Ga, solid GaAs and ordered liquid Ga, as determined by the ICA analysis are used for this purpose (3-component fit). The interface position is denoted by the dashed black line as a guide to the eye. The 2-component fit shows a clear increase in the residue around the interface, which indicates that a linear combination of spectra from liquid Ga and solid GaAs is not able to accurately describe the EELS response observed. The residue for 3-component fit, however, remains low all across the EELS map and does not increase in the area around the interface.

Figure S2e shows the normalized contribution coefficients of the three ICA components in the MLLS fit to the EELS map. As expected, moving from solid GaAs to liquid Ga results in a reduced contribution from the solid GaAs spectral component, while the contribution from the liquid Ga component starts to increase. In addition, the contribution from the ordered liquid Ga starts to increase around the interface and is maximum at the interface position. This is consistent with the fact that the ordered liquid Ga is physically confined to the area around the interface. Moving further away from the interface into the liquid Ga results in the diminished contribution from solid GaAs and ordered liquid Ga.

Figure S2f compares the EELS response of A and B-polar interfaces computed by ICA. This figure shows the third ICA component, which we interpret as the ‘bulk’ plasmon of the ordered liquid Ga, in the case of A and B-polar GaAs nanowires. The two components are almost indistinguishable, suggesting that the plasmon response of the A and B-polar interfaces are very similar.

## **S2 Molecular Dynamics Simulation of the Liquid-Solid Interface**

### **S2.1 Neural network potential**

A neural network potential (NNP) of the Behler-Parrinello kind<sup>[2]</sup> has been used in this work to fit the potential energy surface (PES) of the system. In this scheme, the total energy of the system is divided into atom-centered contributions. A symmetry invariant description of each atomic environment is obtained using a set of symmetry functions (SF), which are used to encode the set of Cartesian coordinates (traditionally used to describe the structure) in a “feature vector” that can be used as input to the neural network.

SFs are defined by a set of parameters that capture particular spatial and angular correlations within a given cut-off. A detailed description of the form and different types of SFs that have been historically used, as well as the details of the implementations in n2p2, can be found here<sup>(25)</sup> Using the same nomenclature, in this work we have used only  $G_2$  and  $G_3$  type SFs.

In order to determine a small, yet effective, set of SFs able to provide a complete description of the local environment we have used the method presented in <sup>[3][4]</sup>. The initial, systematic, set of 604 SFs has been reduced using the CUR selection, choosing 64 SFs for each element, which are presented in **Table S1** for  $G_2$  and **Table S2** for  $G_3$ .

For the set of chosen SFs, we trained a NNP with two hidden layers and 24 nodes per layer using the n2p2 code <sup>[4]</sup>. A total of 4370 randomly initialized weights have been trained using the set of structures detailed in section 1.2 with a 9:1 splitting between training and validation structures.

The root mean square error of the NNP used to run the dynamics is about 1.6 meV/atom for the training set and 2.4 meV/atom for the validation set. Errors on the forces are similar for both sets below  $120 \text{ meV}\text{\AA}^{-1}$ . The distribution of errors is presented in **Figure S3**.

## S2.2 Generation of the dataset

The set of reference structures used to train the NNP has been generated following an iterative procedure, aiming to reduce the number of DFT calculations needed, and adding only information that is relevant to the system.

With the geometry described in the Methods section of the paper and shown in **Figure S4**, which includes both the A and B surfaces interacting with liquid Ga, we have trained a NNP on short *ab initio* molecular dynamics trajectories that have been run with unconverged parameters to speed up the calculations (i.e. the k-point grid has been limited to the  $\Gamma$  point only, as opposed to fully converged calculations where  $3\times 3\times 1$  grids have been used). The potential obtained at this level was used to run longer simulations with the aid of advanced integration schemes, allowing to explore a larger part of the relevant phase space at a fraction of the original cost.

The multiple time stepping integration scheme <sup>[5]</sup> as implemented in the i-PI code<sup>[6]</sup> allows to decompose the contribution to the forces into a fast-varying, short-ranged effect and a slow-varying, long-ranged correction. Since the NNP is able to describe only interaction up to a predefined cut-off, we have used it to compute the short-range interactions. Then, the remaining

long-ranged correction has been computed using the difference between DFT and NNP. Simulations using the multiple time stepping scheme have been run on the NVT ensemble for about 50 ps each. The system containing ZB has been run with successive iterations of the potential at 400 K, 600 K, 750 K, and 1300 K, while the system containing WZ has been run at 400 K. Temperatures have been controlled with a combination of a generalized Langevin <sup>[7]</sup> and stochastic velocity rescaling<sup>[8]</sup> thermostats. The inner timestep has been set to 1 fs and the outer timestep to 20 fs, effectively allowing us to run *ab initio* quality calculations while reducing the original cost by a factor 20. Every new DFT calculation has been used both as a testing point for the current iteration of the NNP and later as a training point for the next iteration.

From the set of newly DFT computed structures, only those contributing with new information to the dataset have been included. The information content has been evaluated using a farthest point selection of configurations, defined with the structure-wide fingerprint based on SFs described here<sup>[31]</sup>. Continuous refinement of the potential has allowed to obtain a NNP able to reproduce very accurately the DFT results obtained during a MD simulation, as shown in **Figure S5**. At this point, the chosen configurations have been recomputed using converged DFT parameters, and the NNP retrained on the fully converged dataset.

The set of 800 structures obtained in this manner has been complemented with further 170 structures of bulk configurations of GaAs (ZB and WZ), Ga ( $\alpha$ , II, and III) and As (A7 structure) and the corresponding surfaces. These structures have been included to enforce the correct behavior of the bulk GaAs and correct values for the surface energies in contact with vacuum.

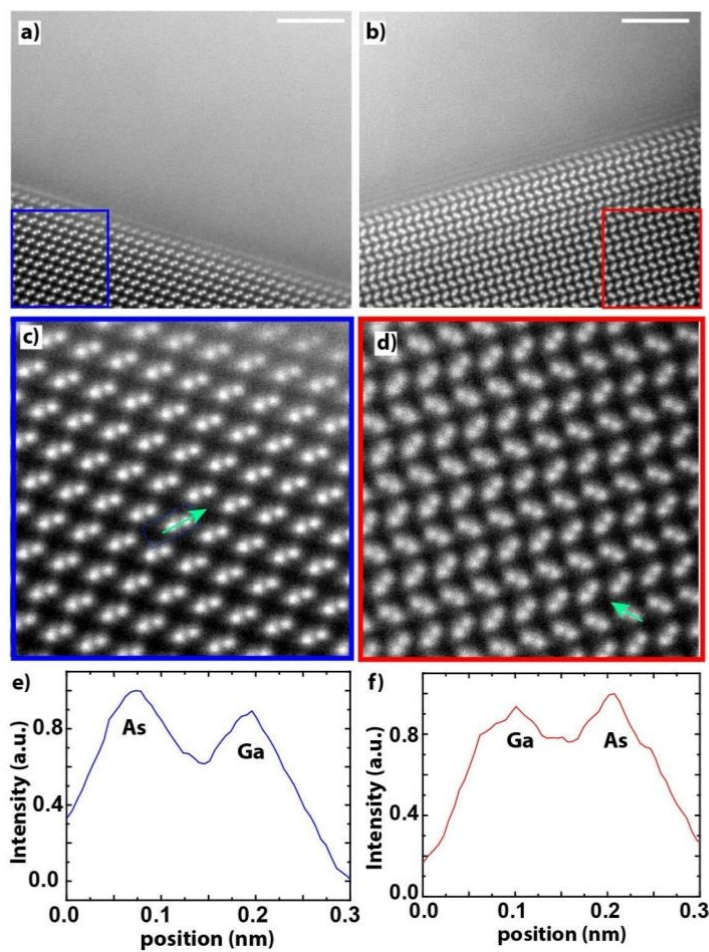
### S2.3 Comparison between the different bulk structures

The densities of the simulations run with both ZB and WZ are here reported for further comparison. **Figure S6** shows the atom density profile along the normalized z-coordinate for the two systems at 300 K. From this figure it is clear that the densities in both the solid and liquid region are the same, irrespective of the crystal structure of the bulk solid. There is, however, a very strong difference between the A polar and the B polar surfaces. This suggests that the ordering at the interface is influenced by the polarity of the surface but not by the bulk structure. The simulation profiles are compared to the experimental ones in the main paper, showing a very good agreement on the position of the peaks.

**Figure S7** and **Figure S8** show top and two side views of the layering at the interface for all 4 possible configurations (ZB-A, ZB-B, WZ-A, WZ-B) at 300 K and 900 K respectively. Similarly to the 1D profiles, the 3D densities are not particularly influenced by the solid bulk, whereas the surface polarity noticeably changes the ordering at the interface. It should be noted that the isocontours for Figure S7 and S8 are drawn at different values, in order to capture the maximum information about the ordering of the interface without cluttering the view.

### S3 Comparison between the experimental observations and MD simulation:

Table S3 lists the distances between the ordered liquid layers and the last crystalline solid layer at a B-polar interface from experimental observations and MD-based simulations. The position of each layer is determined by having a Gaussian fit to the HAADF intensities/ MD densities.



**Figure**

**S1:** Polarity Determination for the NWs. a) and b) The NWs shown in Figure S1. The white scale bar is 2nm. c) and d) Zoomed-in image for the blue and red frames from Figure S1a and S1b. e) and f) HAADF profiles along the green arrows in Figure S1c and S1d, demonstrating that the NWs in these figures are of A and B-polarity, respectively.



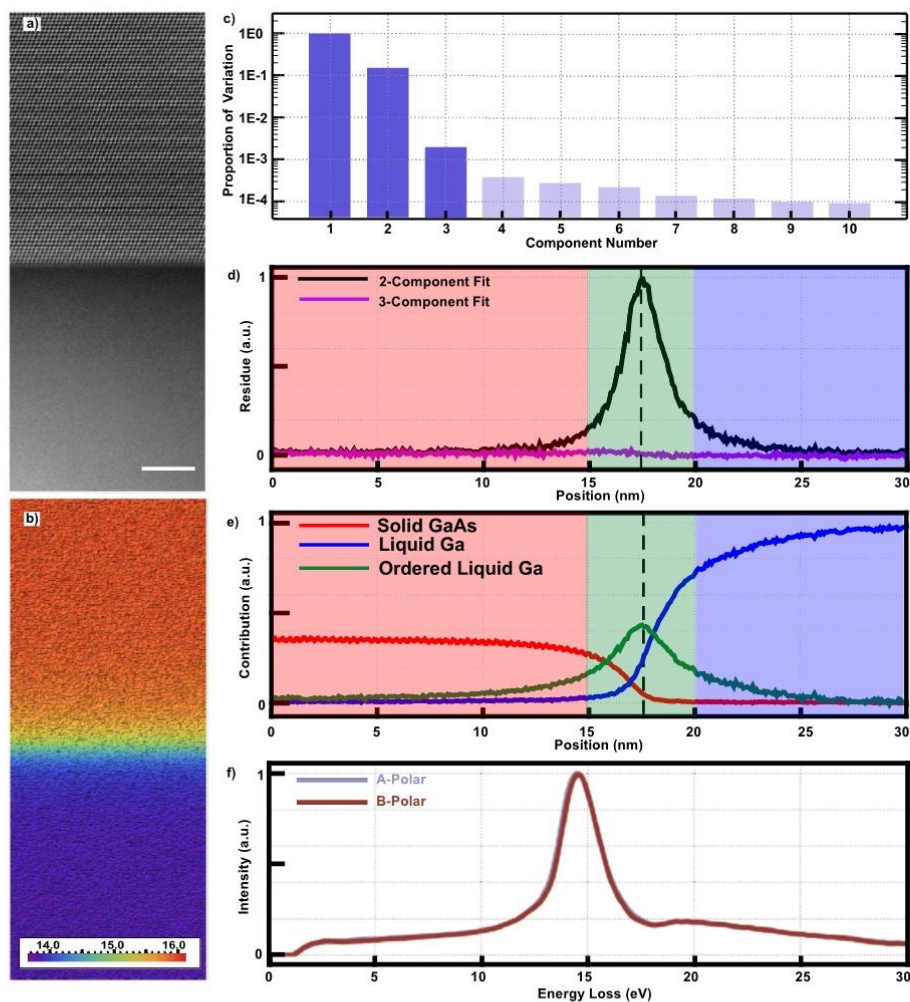


**Figure S2:** details on the application of ICA on the EELS measurements. a) Atomic-resolution annular HAADF image acquired simultaneously to the EELS map. The scale bar shows 5 nm. b) Map of the plasmon peak energy(maximum of the peak) , moving from solid GaAs at the top to liquid at the bottom Ga. c) Principal component analysis (PCA) screeplot

of the EELS hyperspectral dataset. d) Comparison of normalized residues for MLLS fitting based on 2 and 3 components as a function of position. The residue for the 2-component fit drastically increases around the interface, while it stays low in that region for the 3-component fit. The liquid Ga and solid GaAs regions are denoted by transparent blue and red areas, while the area around the interface is demonstrated by transparent green color. e) Normalized contribution coefficients (loading) of the 3 ICA components as a function of position. The same coloring as Figure S2c is used to show the three regions constructing the EELS map. f) Comparison of the EELS responses from the ordered liquid Ga (third component in the ICA analysis) on A and B-polar interfaces.

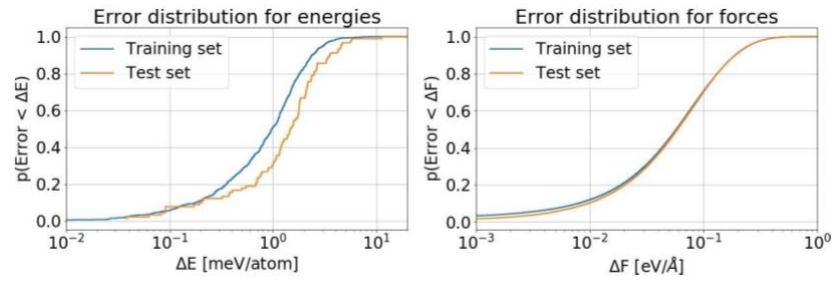


**Figure S3:** The cumulative probability distribution of the errors for the training and test set for both forces and energies.

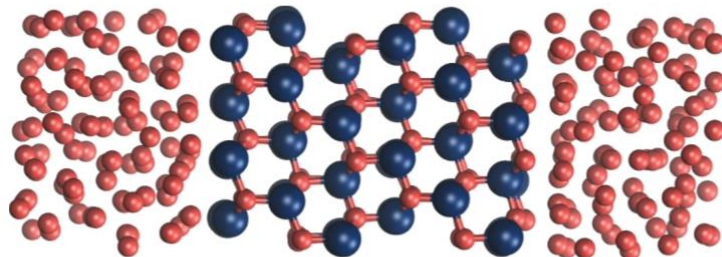


**Figure S4:** A snapshot from a simulation, depicting the geometry used for all of the ZB simulations presented in the paper and in the SM. For wurtzite simulations we have exchanged the solid part with an equal number of Ga and As atoms, changing the unit cell to WZ.

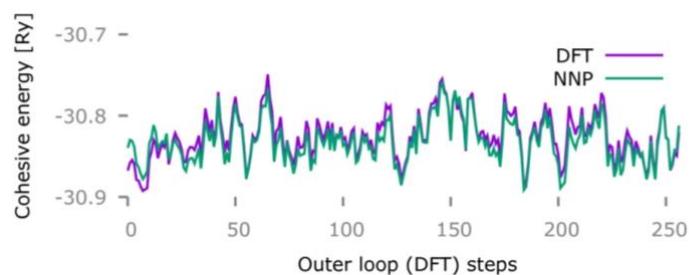


**Figure S5:** The energy predicted by the NNP vs the energy computed with DFT for a multiple time stepping MD run. This comparison let us see the quality of the NNP predictions for structures generated during a simulation, thus outside of the training/validation set. The similarity between NNP and DFT also hints at the fact that the structures generated during the simulations are physically reasonable.

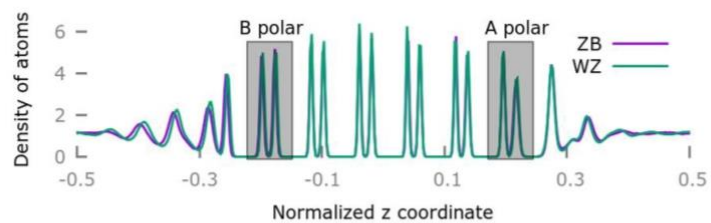


**Figure S6:** The density of atoms along the normalized z-axis for both ZB and WZ at 300 K.

The two curves seem to behave rather similarly, while the difference between the A and B surface is much more evident.

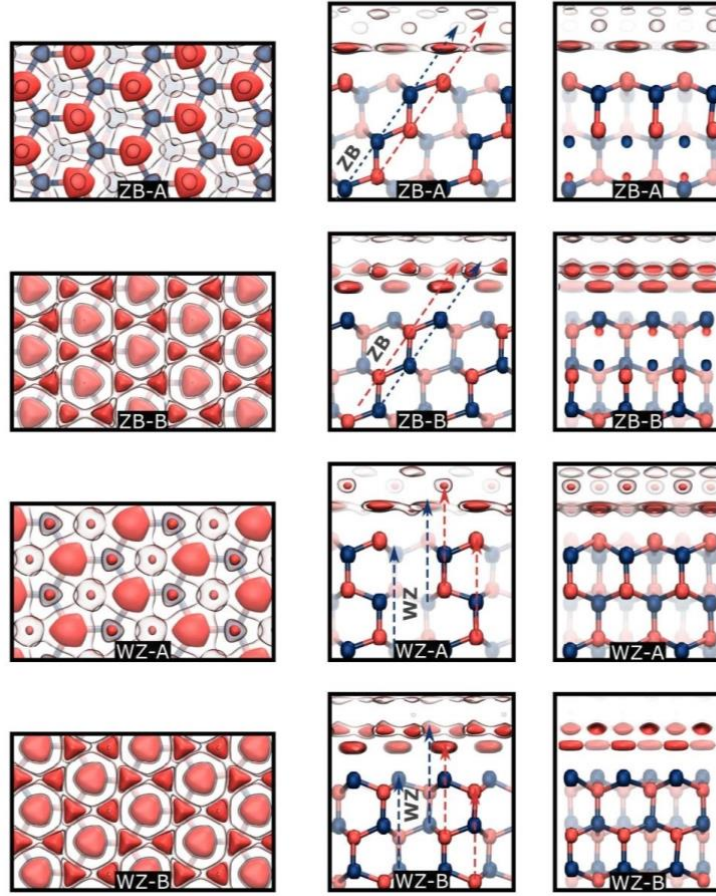


**Figure S7:** Isocontours of the Ga atom density at 300 K, showing ordering at the liquid-Ga/GaAs interface - corresponding to density  $\rho=0.175 \text{ Bohr}^{-3}$  (opaque) and  $\rho=0.09 \text{ Bohr}^{-3}$  (translucent). As and Ga atoms are drawn respectively in blue and red. Objects further from the viewer are represented with less contrast as a depth cue. Views along  $[1\ 1\ 1]$  (left),  $[1\ \bar{1}\ 0]$  (center), and  $[1\ \bar{1}\ 2]$  (right) are presented for both polarities and bulk solid structures, as indicated in the inset.



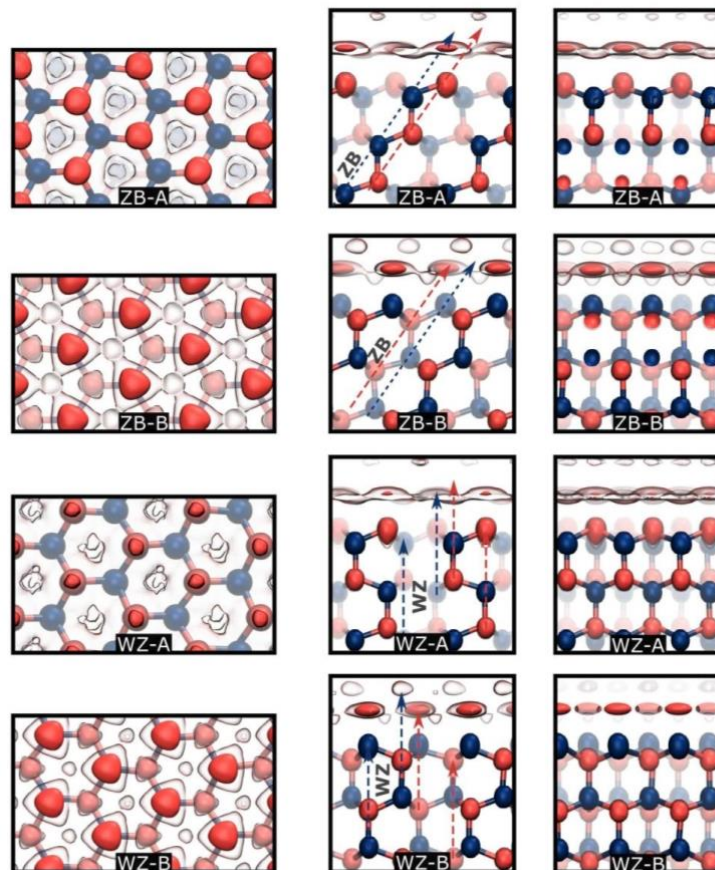


**Figure S8:** Isocontours of the Ga atom density at 900 K, showing ordering at the liquid-Ga/GaAs interface - corresponding to density  $\rho=0.11 \text{ Bohr}^{-3}$  (opaque) and  $\rho=0.06 \text{ Bohr}^{-3}$  (translucent). As and Ga atoms are drawn respectively in blue and red. Objects further from the viewer are represented with less contrast as a depth cue. Views along  $[1\ 1\ 1]$  (left) and  $[1\ \bar{1}\ 0]$  (center), and  $[1\ \bar{1}\ 2]$  (right) are presented for both polarities and bulk solid structures, as indicated in the inset.

**Table S1:** The list of symmetry functions chosen using CUR selection out of a bigger initial set, comprised of SFs with different cut-offs,  $\eta$  and  $r_s$ .

Atom 1	Atom 2	$\eta$	$r_s$	$r_c$	Atom 1	Atom 2	$\eta$	$r_s$	$r_c$
As	As	0.1239	0.000	8	Ga	As	0.1239	0.000	8
	As	0.0156	0.000	8		As	0.0156	0.000	8
	As	0.0541	0.000	8		Ga	0.1239	0.000	8
	Ga	0.1239	0.000	8		As	0.0358	0.000	8
	Ga	0.0156	0.000	8		As	0.0819	0.000	8
	As	0.0819	0.000	8		Ga	0.0156	0.000	8
	Ga	0.0358	0.000	8		Ga	0.0358	0.000	8
	As	0.0069	0.000	12		As	0.0069	0.000	12
	Ga	0.0819	0.000	8		Ga	0.0819	0.000	8
	As	0.0586	11.869	16		As	0.0586	11.869	16
	As	0.1065	8.805	16		As	0.1065	8.805	16
	Ga	0.0069	0.000	12		Ga	0.0069	0.000	12
	As	0.0039	0.000	16		As	0.0039	0.000	16
	As	0.0375	14.837	20		As	0.0375	14.837	20
	As	0.0682	11.006	20		As	0.0682	11.006	20
	As	0.1239	8.165	20		As	0.1239	8.165	20
	Ga	0.0586	11.869	16		Ga	0.0586	11.869	16
	Ga	0.1065	8.805	16		Ga	0.1065	8.805	16
	As	0.0025	0.000	20		As	0.0025	0.000	20
	As	0.0364	0.000	12		As	0.0364	0.000	12
	Ga	0.0039	0.000	16		Ga	0.0039	0.000	16
	Ga	0.0375	14.837	20		Ga	0.0375	14.837	20
	Ga	0.0682	11.006	20		Ga	0.0682	11.006	20
	Ga	0.1239	8.165	20		Ga	0.1239	8.165	20
	Ga	0.0025	0.000	20		Ga	0.0025	0.000	20
	Ga	0.0364	0.000	12		Ga	0.0364	0.000	12
	As	0.0083	0.000	20		As	0.0083	0.000	20
	Ga	0.0083	0.000	20		Ga	0.0083	0.000	20

**Table S2:** The list of symmetry functions chosen using the CUR selection of a bigger initial set, comprised of SFs with different cut-offs,  $\eta$  and  $\zeta$ .

Atom 1	Atom 2	Atom 3	$\eta$	$\lambda$	$\zeta$	$r_c$	Atom 1	Atom 2	Atom 3	$\eta$	$\lambda$	$\zeta$	$r_c$
As	As	As	0.0156	1	1	8	Ga	As	As	0.0156	-1	1	8
	As	As	0.0156	-1	1	8		As	As	0.0156	1	1	8
	Ga	As	0.0156	1	1	8		Ga	As	0.0156	1	1	8
	Ga	As	0.0156	1	8	8		Ga	As	0.0156	1	8	8
	As	As	0.0069	-1	4	12		As	As	0.0156	1	8	8
	As	As	0.0069	1	4	12		As	As	0.0069	-1	4	12
	Ga	Ga	0.0156	-1	1	8		As	As	0.0069	-1	2	12
	As	As	0.0069	1	1	12		As	As	0.0069	1	4	12
	Ga	As	0.0156	-1	1	8		As	As	0.0069	-1	1	12
	As	As	0.0156	1	8	8		Ga	Ga	0.0156	1	1	8
	As	As	0.0069	-1	1	12		As	As	0.0069	1	2	12
	Ga	As	0.0069	-1	4	12		As	As	0.0159	-1	4	12
	Ga	As	0.0069	1	4	12		Ga	As	0.0069	-1	4	12
	Ga	Ga	0.0156	1	1	8		Ga	As	0.0069	1	4	12
	Ga	As	0.0069	-1	2	12		As	As	0.0159	1	4	12
	As	As	0.0159	-1	1	12		Ga	As	0.0156	-1	1	8
	As	As	0.0159	1	4	12		As	As	0.0159	-1	1	12
	As	As	0.0159	-1	4	12		Ga	Ga	0.0156	-1	1	8
	As	As	0.0241	1	1	12		As	As	0.0241	1	1	12
	Ga	As	0.0069	1	1	12		Ga	As	0.0069	-1	1	12
	Ga	As	0.0159	1	4	12		As	As	0.0364	-1	2	12
	Ga	Ga	0.0069	-1	4	12		Ga	As	0.0069	1	1	12
	Ga	As	0.0159	-1	4	12		As	As	0.0105	1	1	12
	Ga	As	0.0105	-1	1	12		Ga	Ga	0.0069	-1	4	12
	As	As	0.0105	1	1	12		Ga	Ga	0.0069	1	4	12
	Ga	Ga	0.0069	1	4	12		Ga	As	0.0159	1	4	12
	Ga	As	0.0241	1	1	12		Ga	As	0.0159	-1	1	12
	Ga	As	0.0241	-1	2	12		Ga	As	0.0159	-1	4	12
	Ga	Ga	0.0069	-1	1	12		Ga	As	0.0241	1	1	12
	Ga	Ga	0.0159	-1	4	12		Ga	Ga	0.0069	1	1	12
	Ga	Ga	0.0069	1	1	12		Ga	Ga	0.0069	-1	1	12
	Ga	As	0.0364	1	4	12		Ga	As	0.0364	1	4	12
	Ga	Ga	0.0159	-1	1	12		Ga	Ga	0.0159	-1	1	12
	Ga	Ga	0.0159	1	4	12		Ga	Ga	0.0159	-1	4	12
	Ga	Ga	0.0241	1	1	12		Ga	Ga	0.0159	1	1	12
	Ga	Ga	0.0364	-1	2	12		Ga	Ga	0.0241	1	4	12

**Table S3. The distances of ordered liquid layers from the last crystalline layer (nm) for a B polar interface from experimental observations and MD simulations**

	1 <sup>st</sup> ordered layer	2 <sup>nd</sup> ordered layer	3 <sup>rd</sup> ordered layer	4 <sup>th</sup> ordered layer
HAADF image	0.263	0.578	0.802	1.014
Simulations	0.264	0.576	0.799	1.013



- [1] G. Lucas, P. Burdet, M. Cantoni, C. Hébert, *Micron* **2013**, 52–53, 49.
- [2] J. Behler, M. Parrinello, *Phys. Rev. Lett.* **2007**, 98, DOI 10.1103/PhysRevLett.98.146401.
- [3] G. Imbalzano, A. Anelli, D. Giofré, S. Klees, J. Behler, M. Ceriotti, *J. Chem. Phys.* **2018**, 148, DOI 10.1063/1.5024611.
- [4] A. Singraber, T. Morawietz, J. Behler, C. Dellago, *J. Chem. Theory Comput.* **2019**, 15, 3075.
- [5] M. Tuckerman, B. J. Berne, G. J. Martyna, *J. Chem. Phys.* **1992**, 97, 1990.
- [6] V. Kapil, M. Rossi, O. Marsalek, R. Petraglia, Y. Litman, T. Spura, B. Cheng, A. Cuzzocrea, R. H. Meißner, D. M. Wilkins, B. A. Helfrecht, P. Juda, S. P. Bienvenue, W. Fang, J. Kessler, I. Poltavsky, S. Vandenbrande, J. Wieme, C. Corminboeuf, T. D. Kühne, D. E. Manolopoulos, T. E. Markland, J. O. Richardson, A. Tkatchenko, G. A. Tribello, V. Van Speybroeck, M. Ceriotti, *Comput. Phys. Commun.* **2019**, 236, 214.
- [7] M. Ceriotti, G. Bussi, M. Parrinello, *J. Chem. Theory Comput.* **2010**, 6, 1170.
- [8] G. Bussi, D. Donadio, M. Parrinello, *J. Chem. Phys.* **2007**, 126, DOI 10.1063/1.2408420.



# Appendix B: Unpublished Experimental Results

In this section, some unpublished experimental data on  $Zn_3P_2$  thin films are presented.

First, we start by providing the PL spectra of three samples with varying compositions grown on p-type  $InP$  substrate. These samples are grown with identical parameters, except for the degassing time at  $580^\circ C$  and all have monocrystalline structures. Table B 2 shows the degassing time and the composition of these samples as measured by STEM-EDX. The reason for the differences in the compositions is not known at this point. The PL measurements are conducted at 12K and using a 488 nm laser.

Table B 2 : the degassing time and composition of the three samples studied by PL.

Degassing time at $580^\circ C$ (min)	Zn/P
30	1.75
60	1.51
75	1.94

The data has been corrected for the responsivity of the spectrometer. Figure B 1 show the PL spectra of the three samples measured with the laser power of  $9\text{ mW}$ . The three samples exhibit very strong emission at sub-1.3eV energies, down to the detection limit of the silicon detector. This emission is hypothesized to originate from defect transitions. The different emission between the three samples is likely attributable to different defect concentrations owing to the variations in growth conditions.

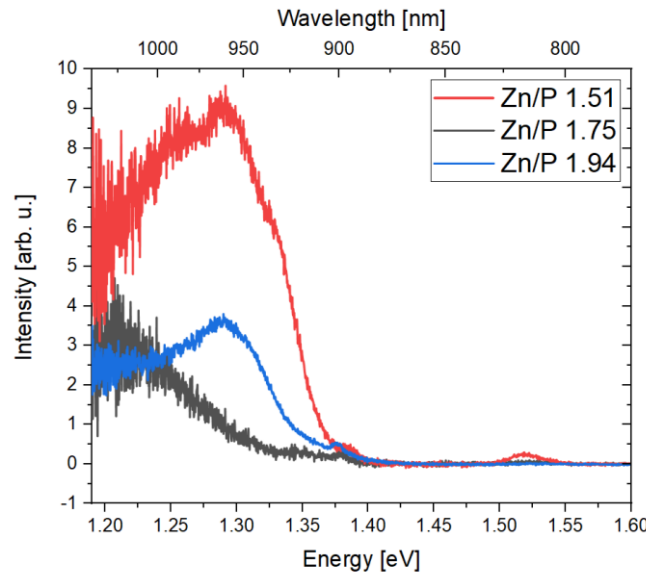


Figure B 1 : the PL spectra of three samples with different stoichiometries measured at 12K with the 488 laser and the laser power of  $9\text{ mW}$ .

The composition of the sample with  $Zn/P = 1.51$  is very close to the stoichiometric ratio of  $Zn_3P_2$  at 1.5 and its PL peaks around 1.52 eV are consistent with transitions across the direct bandgap, but the splitting of the peak is unexpected and still unexplained. For the other samples, despite the monocrystalline structure of the films, the peak at 1.52 eV is not observed, which could be explained by the non-stoichiometric composition of these films. In order to further investigate the properties of these thin films, Raman spectroscopy at 12 K with 9 mW power is conducted. Figure B 2 shows the comparison between the three samples and the shifts in the intensity of Raman peaks according to the composition. While there is a clear pattern of the change in the intensity of each peaks as a function of composition, the reason for this behavior is not known yet and is under study.

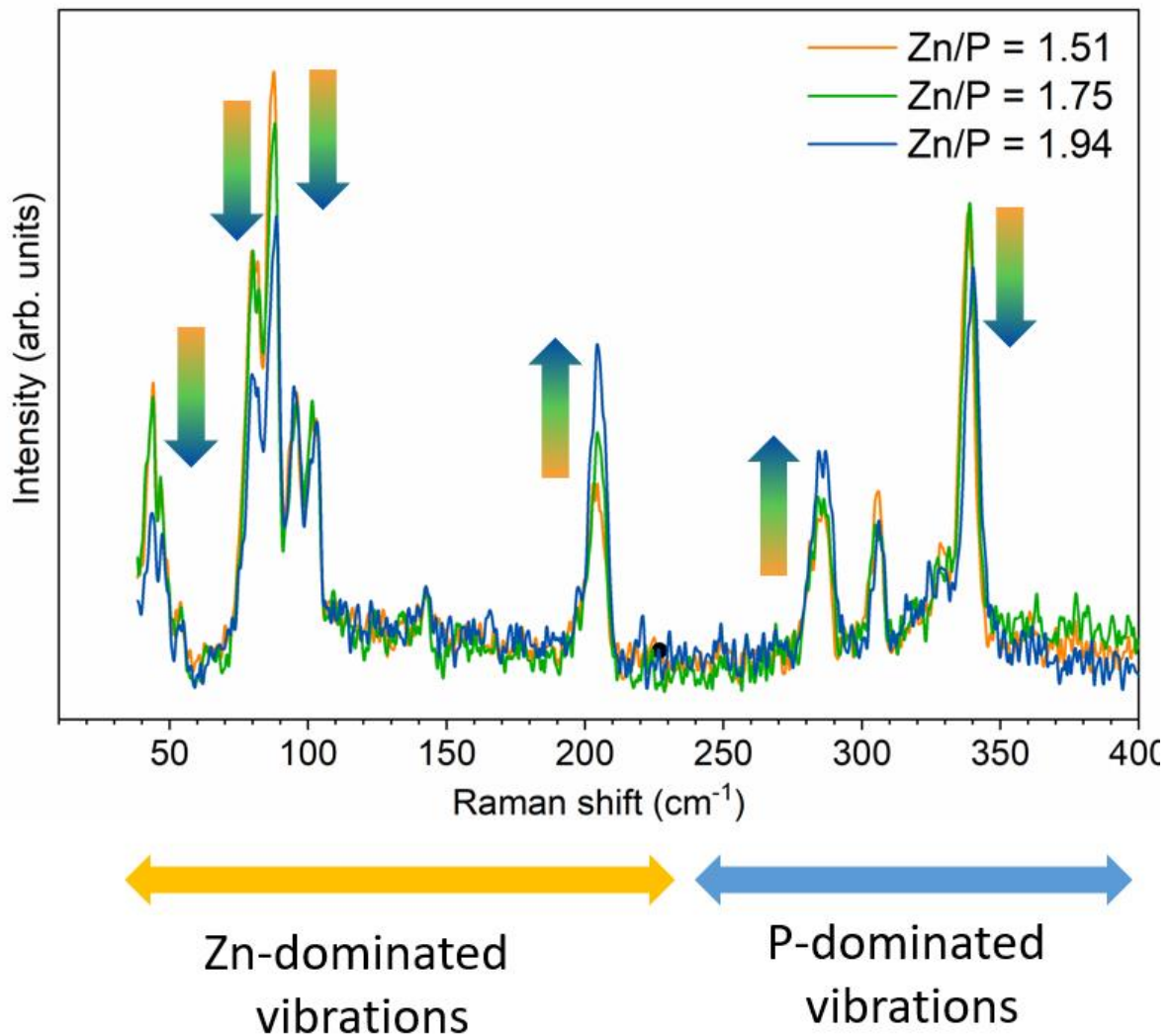


Figure B 2. The change in the intensity of Raman peaks for three monocrystalline thin films with different stoichiometries.

The PL and Raman measurements presented in this section are conducted by Elias Zsolt Stutz while the EDX measurements are done by Santhanu Panikar Ramanandan. In addition, Mirjana Dimitrievska has helped with the analysis. In addition to these measurements, EELS and Terahertz spectroscopy are being used to further understand the different aspects of  $Zn_3P_2$  thin films.

## Publication List

**Zamani M**, Stutz EZ, Escobar Steinvall S, Zamani R, Paul R, Leran JB, Dimitrievska M, Fontcuberta i Morral A, “The path towards 1  $\mu\text{m}$  monocrystalline  $\text{Zn}_3\text{P}_2$  films on  $\text{InP}$ : substrate preparation, growth conditions and luminescence properties”. Under review

Stutz EZ, Escobar Steinvall S, Litvinchuk AP, Leran J-B, **Zamani M**, Paul R, et al. “*Raman spectroscopy and lattice dynamics calculations of tetragonally-structured single crystal zinc phosphide ( $\text{Zn}_3\text{P}_2$ ) nanowires*”. Nanotechnology . 2021 Feb;32(8):085704.

Escobar Steinvall S, Stutz EZ, Paul R, **Zamani M**, Dzade NY, Piazza V, et al. “*Towards defect-free thin films of the earth-abundant absorber zinc phosphide by nanopatterning*”. Nanoscale Adv, 2021 Jan, (3): 326-332

Escobar Steinvall S, Ghisalberti L, Zamani RR, Tappy N, Hage FS, Stutz EZ, **Zamani M**, Paul R, et al. “*The role of indium insertion in the superlattice formation mechanism and their optical properties*”. Nanoscale . 2020 Nov;12(44):22534.

**Zamani M\***, Imbalzano G\*, Tappy N, Alexander DTL, Martí-Sánchez S, Ghisalberti L, et al. “*3D Ordering at the Liquid–Solid Polar Interface of Nanowires. Adv Mater*”. 2020 Sep ;32(38):2001030.

Paul R, Humblot N, Humblot N, Steinvall SE, Stutz EZ, Joglekar SS, Leran JB, **Zamani M**, et al. “*Van der Waals Epitaxy of Earth-Abundant  $\text{Zn}_3\text{P}_2$  on Graphene for Photovoltaics*”. Cryst Growth Des . 2020 Jun ;20(6):3816–25.

Escobar Steinvall S, Tappy N, Ghasemi M, Zamani RR, Lagrange T, Stutz EZ, Leran JB, **Zamani M**, et al. “*Multiple morphologies and functionality of nanowires made from earth-abundant zinc phosphide*”. Nanoscale Horizons . 2020 Feb ;5(2):274–82.

Ghasemi M, Stutz E, Escobar Steinvall S, **Zamani M**, Fontcuberta i Morral A. “*Thermodynamic re-assessment of the Zn–P binary system*”. Materialia. 2019 Jun ;6:100301.

Ghisalberti L, Potts H, Friedl M, **Zamani M**, Güniat L, Tütüncüoğlu G, et al. “*Questioning liquid droplet stability on nanowire tips: From theory to experiment*”. Nanotechnology. 2019 Apr ;30(28).

Güniat L, Martí-Sánchez S, Garcia O, Mégane B, Vindice D, Tappy N, Friedl M, Kim W, **Zamani M**, et al. “*III–V Integration on Si(100): Vertical Nanospades*”. ACS Nano. 2019 Apr ;13:53.

**Zamani M\***, Tütüncüoglu G\*, Martí-Sánchez S, Francaviglia L, Güniat L, Ghisalberti L, et al. “*Optimizing the yield of A-polar GaAs nanowires to achieve defect-free zinc blende structure and enhanced optical functionality*”. Nanoscale. 2018 Sep ;10(36):17080–91.

Friedl M, Cervený K, Weigele P, Tütüncüoglu G, Martí-Sánchez S, Huang C, Patlatiuk T, Potts H, Sun Z, O'Hill M, Güniat L, Kim W, **Zamani M**, et al. “*Template-Assisted Scalable Nanowire Networks*”. Nano Lett. 2018 Apr 11;18(4):2666–71.

# Bibliography

1. McCluskey MD, Janotti A. Defects in Semiconductors. J Appl Phys [Internet]. 2020 May 21 [cited 2021 Jan 4];127(19):190401. Available from: <http://aip.scitation.org/doi/10.1063/5.0012677>
2. Mahajan S. Defects in semiconductors and their effects on devices. Acta Mater. 2000 Jan 1;48(1):137–49.
3. Tuomisto F, editor. Characterisation and Control of Defects in Semiconductors [Internet]. Characterisation and Control of Defects in Semiconductors. Institution of Engineering and Technology; 2019 [cited 2021 Jan 4]. Available from: <https://digital-library.theiet.org/content/books/cs/pbcs045e>
4. Kressel H. The Effect of Crystal Defects on Optoelectronic Devices. Semicond Semimetals. 1981 Jan 1;16(C):1–52.
5. Ni K, Eneman G, Simoen E, Mocuta A, Collaert N, Thean A, et al. Electrical Effects of a Single Extended Defect in MOSFETs. IEEE Trans Electron Devices. 2016;63(8):3069–75.
6. Hellenbrand M, Memisevic E, Svensson J, Krishnaraja A, Lind E, Wernersson LE. Effect of gate oxide defects on tunnel transistor RF performance. In: Device Research Conference - Conference Digest, DRC. Institute of Electrical and Electronics Engineers Inc.; 2018.
7. Ferrazza F. Crystalline Silicon: Manufacture and Properties. In: Practical Handbook of Photovoltaics. Elsevier Ltd; 2012. p. 79–97.
8. Czochralski Process - an overview | ScienceDirect Topics [Internet]. [cited 2021 Jan 4]. Available from: <https://www.sciencedirect.com/topics/chemistry/czochralski-process>
9. Akasaki I. Key inventions in the history of nitride-based blue LED and LD. J Cryst Growth. 2007 Mar 1;300(1):2–10.
10. Nakamura S. Background Story of the Invention of Efficient InGaN Blue-Light-Emitting Diodes (Nobel Lecture). Angew Chemie Int Ed [Internet]. 2015 Jun 26 [cited 2021 Jan 4];54(27):7770–88. Available from: <http://doi.wiley.com/10.1002/anie.201500591>
11. Ernst F, Pirouz P. The formation mechanism of planar defects in compound semiconductors grown epitaxially on {100} silicon substrates. J Mater Res [Internet]. 1989 [cited 2021 Jan 4];4(4):834–42. Available from: <https://doi.org/10.1557/JMR.1989.0834>
12. Schwartzman AF. Misfit Dislocations at II-VI/GaAs Interfaces. MRS Proc [Internet]. 1990 [cited 2021 Jan 4];183. Available from: <https://www.cambridge.org/core/journals/mrs-online-proceedings-library-archive/article/abs/misfit-dislocations-at-ii-vi-gaas-interfaces/07A42C09697CE82A1E5B05F53D5B9C54>
13. Smith DJ. Atomic-resolution structure imaging of defects and interfaces in compound semiconductors. Vol. 66, Progress in Crystal Growth and Characterization of Materials. Elsevier Ltd; 2020. p. 100498.
14. Needleman DB, Poindexter JR, Kurchin RC, Marius Peters I, Wilson G, Buonassisi T. Economically sustainable scaling of photovoltaics to meet climate targets. Energy Environ Sci [Internet]. 2016 Jun 1 [cited 2021 Jan 5];9(6):2122–9. Available from: [www.rsc.org/ees](http://www.rsc.org/ees)



15. Ise F. Photovoltaics Report [Internet]. [cited 2021 Jan 5]. Available from: [www.ise.fraunhofer.de](http://www.ise.fraunhofer.de)
16. De Wild-Scholten MJ. Energy payback time and carbon footprint of commercial photovoltaic systems. *Sol Energy Mater Sol Cells*. 2013 Dec 1;119:296–305.
17. The Future of Solar Energy | MIT Energy Initiative [Internet]. 2015 [cited 2017 Sep 26]. Available from: [https://www.google.ch/\\_/chrome/newtab?espv=2&ie=UTF-8](https://www.google.ch/_/chrome/newtab?espv=2&ie=UTF-8)
18. McLellan B, Yamasue E, Tezuka T, Corder G, Golev A, Giurco D. Critical Minerals and Energy—Impacts and Limitations of Moving to Unconventional Resources. *Resources* [Internet]. 2016 May 13 [cited 2017 Sep 28];5(2):19. Available from: <http://www.mdpi.com/2079-9276/5/2/19>
19. Fulvio Ardente, Fabrice Mathieux MR. Recycling of electronic displays: Analysis of pre-processing and potential ecodesign improvements. *Resour Conserv Recycl* [Internet]. 2014 Nov 1 [cited 2017 Sep 28];92:158–71. Available from: <http://www.sciencedirect.com/science/article/pii/S0921344914001955>
20. Parag S. Vasekar, Tara P. Dhakal. Solar Cells - Research and Application Perspectives- Chapter 6:Thin Film Solar Cells Using Earth-Abundant Materials. In: *Solar Cells - Research and Application Perspectives* [Internet]. InTech; 2013 [cited 2017 Oct 2]. Available from: <http://www.intechopen.com/books/solar-cells-research-and-application-perspectives/thin-film-solar-cells-using-earth-abundant-materials>
21. Song X, Ji X, Li M, Lin W, Luo X, Zhang H. A Review on Development Prospect of CZTS Based Thin Film Solar Cells. *Int J Photoenergy* [Internet]. 2014 May 26 [cited 2017 Sep 28];2014:1–11. Available from: <http://www.hindawi.com/journals/ijp/2014/613173/>
22. J.Henry, K.Mohanraj GS. Electrical and optical properties of CZTS thin films prepared by SILAR method. *J Asian Ceram Soc* [Internet]. 2016 Mar 1 [cited 2017 Sep 28];4(1):81–4. Available from: <http://www.sciencedirect.com/science/article/pii/S2187076415300245>
23. Wang W, Shen H, Wong LH, Su Z, Yao H, Li Y. A 4.92% efficiency  $\text{Cu}_2\text{ZnSnS}_4$  solar cell from nanoparticle ink and molecular solution. *RSC Adv* [Internet]. 2016 [cited 2017 Sep 28];6(59):54049–53. Available from: <http://xlink.rsc.org/?DOI=C6RA08604G>
24. Wallace SK, Mitzi DB, Walsh A. The Steady Rise of Kesterite Solar Cells. *ACS Energy Lett* [Internet]. 2017 Apr 14 [cited 2017 Sep 28];2(4):776–9. Available from: <http://pubs.acs.org/doi/abs/10.1021/acsenenergylett.7b00131>
25. Best Research-Cell Efficiency Chart | Photovoltaic Research | NREL [Internet]. [cited 2021 Jan 25]. Available from: <https://www.nrel.gov/pv/cell-efficiency.html>
26. Chen S, Yang JH, Gong XG, Walsh A, Wei SH. Intrinsic point defects and complexes in the quaternary kesterite semiconductor  $\text{Cu}_2\text{ZnSnS}_4$ . *Phys Rev B - Condens Matter Mater Phys* [Internet]. 2010 Jun 8 [cited 2021 Jan 25];81(24):245204. Available from: <https://journals.aps.org/prb/abstract/10.1103/PhysRevB.81.245204>
27. Nazligul AS, Wang M, Choy KL. Recent Development in Earth-Abundant Kesterite Materials and Their Applications. *Sustainability* [Internet]. 2020 Jun 24 [cited 2021 Jan 25];12(12):5138. Available from: <https://www.mdpi.com/2071-1050/12/12/5138>
28. Minerals Information Team U. Mineral Commodity Summaries 2007. 2007.
29. Wadia C, Alivisatos AP, Kammen DM. Materials Availability Expands the Opportunity for Large-Scale Photovoltaics Deployment. *Environ Sci Technol* [Internet]. 2009 Mar 15 [cited 2017 Oct 2];43(6):2072–7. Available from: <http://pubs.acs.org/doi/abs/10.1021/es8019534>

30. Yin L, Cheng G, Feng Y, Li Z, Yang C, Xiao X. Limitation factors for the performance of kesterite  $\text{Cu}_2\text{ZnSnS}_4$  thin film solar cells studied by defect characterization. RSC Adv [Internet]. 2015 Apr 30 [cited 2017 Sep 28];5(50):40369–74. Available from: <http://xlink.rsc.org/?DOI=C5RA00069F>
31. Scragg JJ, Dale PJ, Colombara D, Peter LM. Thermodynamic aspects of the synthesis of thin-film materials for solar cells. ChemPhysChem [Internet]. 2012 Aug 27;13(12):3035–46. Available from: <https://chemistry-europe.onlinelibrary.wiley.com/doi/full/10.1002/cphc.201200067>
32. Scragg JJ, Wätjen JT, Edoff M, Ericson T, Kubart T, Platzer-Björkman C. A Detrimental Reaction at the Molybdenum Back Contact in  $\text{Cu}_2\text{ZnSn}(\text{S},\text{Se})_4$  Thin-Film Solar Cells. J Am Chem Soc [Internet]. 2012 Nov 28 [cited 2017 Sep 29];134(47):19330–3. Available from: <http://pubs.acs.org/doi/abs/10.1021/ja308862n>
33. Colombara D, Dale P, Peter L, Scragg J, Siebentritt S. CHAPTER 5. Thin-film Photovoltaics Based on Earth-abundant Materials- Advance Concepts in Photovoltaics. In 2014 [cited 2017 Sep 29]. p. 118–85. Available from: <http://ebook.rsc.org/?DOI=10.1039/9781849739955-00118>
34. Ahmed S, Reuter KB, Gunawan O, Guo L, Romankiw LT, Deligianni H. A High Efficiency Electrodeposited  $\text{Cu}_2\text{ZnSnS}_4$  Solar Cell. Adv Energy Mater [Internet]. 2012 Feb 1 [cited 2017 Sep 29];2(2):253–9. Available from: <http://doi.wiley.com/10.1002/aenm.201100526>
35. Yuan B, Luan W, Tu S, Wu J. One-step synthesis of pure pyrite  $\text{FeS}_2$  with different morphologies in water. New J Chem [Internet]. 2015 May 6 [cited 2017 Sep 29];39(5):3571–7. Available from: <http://xlink.rsc.org/?DOI=C4NJ02243B>
36. Krishnamoorthy A, Herbert FW, Yip S, Van Vliet KJ, Yildiz B. Electronic states of intrinsic surface and bulk vacancies in  $\text{FeS}_2$ . J Phys Condens Matter [Internet]. 2013 Jan 30 [cited 2017 Sep 29];25(4):045004. Available from: <http://stacks.iop.org/0953-8984/25/i=4/a=045004?key=crossref.5d2e51b3f892d5e97173d81ae1b4b692>
37. V.Antonucci, A.S.Arco', N.Giordano, P.L.Antonucci, U.Russo, D.L.Cocke FC. Photoactive screen-printed pyrite anodes for electrochemical photovoltaic cells. Sol Cells [Internet]. 1991 Mar 1 [cited 2017 Sep 29];31(2):119–41. Available from: <http://www.sciencedirect.com/science/article/pii/037967879190016I>
38. Wadia C, Wu Y, Gul S, Volkman SK, Guo J, Alivisatos AP. Surfactant-assisted hydrothermal synthesis of single phase pyrite  $\text{FeS}_2$  nanocrystals. Chem Mater [Internet]. 2009 Jul 14;21(13):2568–70. Available from: <http://pubs.acs.org>.
39. Hall RB, Birkmire RW, Phillips JE, Meakin JD. Thin-film polycrystalline  $\text{Cu}_2\text{S}/\text{Cd}_{1-x}\text{Zn}_x\text{S}$  solar cells of 10% efficiency. Appl Phys Lett [Internet]. 1981 Jun 4 [cited 2017 Sep 29];38(11):925–6. Available from: <http://aip.scitation.org/doi/10.1063/1.92184>
40. Wu Y, Wadia C, Ma W, Sadtler B, Alivisatos AP. Synthesis and Photovoltaic Application of Copper(I) Sulfide Nanocrystals. Nano Lett [Internet]. 2008 Aug [cited 2017 Oct 2];8(8):2551–5. Available from: <http://pubs.acs.org/doi/abs/10.1021/nl801817d>
41. Al-Dhafiri AM, Russell GJ, Woods J. Degradation in  $\text{CdS}-\text{Cu}_2\text{S}$  photovoltaic cells. Semicond Sci Technol [Internet]. 1992 Aug 1 [cited 2017 Oct 2];7(8):1052–7. Available from: <http://stacks.iop.org/0268-1242/7/i=8/a=005?key=crossref.65203dbd8ed9edc4ac943f5365ba06f7>
42. Partain LD, McLeod PS, Duisman JA, Peterson TM, Sawyer DE, Dean CS. Degradation of a  $\text{Cu}_x\text{S}/\text{CdS}$  solar cell in hot, moist air and recovery in hydrogen and air. J Appl Phys [Internet]. 1983 Nov 4 [cited 2017 Oct 2];54(11):6708–20. Available from:

<http://aip.scitation.org/doi/10.1063/1.331858>

43. Phase relations and optical properties of semiconducting ternary sulfides in the system Cu–Sn–S. *J Phys Chem Solids* [Internet]. 2003 Sep 1 [cited 2017 Oct 2];64(9–10):1859–62. Available from: <http://www.sciencedirect.com/science/article/pii/S0022369703001720>
44. Nelson J. *The Physics Of Solar Cells*. Imperial College Press. 2009.
45. Swinkels MY, Campo A, Vakulov D, Kim W, Gagliano L, Steinvall SE, et al. Measuring the Optical Absorption of Single Nanowires. *Phys Rev Appl*. 2020 Aug 1;14(2):024045.
46. Fagen EA. Optical properties of Zn<sub>3</sub>P<sub>2</sub>. *J Appl Phys*. 1979 Oct 25;50(10):6505–15.
47. Kimball GM, Müller AM, Lewis NS, Atwater HA. Photoluminescence-based measurements of the energy gap and diffusion length of Zn<sub>3</sub>P<sub>2</sub>. *Appl Phys Lett* [Internet]. 2009 Sep 14;95(11):112103. Available from: <http://aip.scitation.org/doi/10.1063/1.3225151>
48. Ghasemi M, Stutz E, Escobar Steinvall S, Zamani M, Fontcuberta i Morral A. Thermodynamic re-assessment of the Zn–P binary system. *Materialia*. 2019 Jun 1;6:100301.
49. Wyeth NC, Catalano A. Spectral response measurements of minority-carrier diffusion length in Zn<sub>3</sub>P<sub>2</sub>. *J Appl Phys* [Internet]. 1979 Mar 29;50(3):1403–7. Available from: <http://aip.scitation.org/doi/10.1063/1.326122>
50. Bosco JP, Kimball GM, Lewis NS, Atwater HA. Pseudomorphic growth and strain relaxation of  $\alpha$ -Zn<sub>3</sub>P<sub>2</sub> on GaAs(001) by molecular beam epitaxy. *J Cryst Growth*. 2013 Jan 15;363:205–10.
51. Liu Y, Zhou B, Lv W, Wu C, Su X, Wang J. Experimental investigation and thermodynamic assessment of the Zn–Si–P system. *Surf Coatings Technol*. 2016 Nov 25;306:370–7.
52. Tu H, Yin F, Su X, Liu Y, Wang X. Experimental investigation and thermodynamic modeling of the Al–P–Zn ternary system. *Calphad Comput Coupling Phase Diagrams Thermochem*. 2009 Dec 1;33(4):755–60.
53. Nayar PS, Catalano A. Zinc phosphide-zinc oxide heterojunction solar cells. *Appl Phys Lett* [Internet]. 1981 Jul 4 [cited 2017 Oct 4];39(1):105–7. Available from: <http://aip.scitation.org/doi/10.1063/1.92537>
54. Bhushan M, Catalano A. Polycrystalline Zn<sub>3</sub>P<sub>2</sub> Schottky barrier solar cells. *Appl Phys Lett* [Internet]. 1981 Jan 4 [cited 2017 Oct 4];38(1):39–41. Available from: <http://aip.scitation.org/doi/10.1063/1.92124>
55. A.Catalano RBH. Defect dominated conductivity in Zn<sub>3</sub>P<sub>2</sub>. *J Phys Chem Solids* [Internet]. 1980 Jan 1 [cited 2017 Oct 4];41(6):635–40. Available from: <http://www.sciencedirect.com/science/article/pii/0022369780900153?via%3Dihub>
56. Bhushan M. Schottky solar cells on thin polycrystalline Zn<sub>3</sub>P<sub>2</sub> films. *Appl Phys Lett* [Internet]. 1982 Jan 4 [cited 2017 Oct 4];40(1):51–3. Available from: <http://aip.scitation.org/doi/10.1063/1.92921>
57. Wyeth NC, Catalano A. Spectral response measurements of minority-carrier diffusion length in Zn<sub>3</sub>P<sub>2</sub>. *J Appl Phys* [Internet]. 1979 Mar 29;50(3):1403–7. Available from: <http://aip.scitation.org/doi/10.1063/1.326122>
58. Suda T, Suzuki M, Kurita S. Polycrystalline Zn<sub>3</sub>P<sub>2</sub>/Indium-Tin Oxide Solar Cells. *Jpn J Appl Phys* [Internet]. 1983 Oct 20 [cited 2017 Oct 4];22(Part 2, No. 10):L656–8. Available from: <http://stacks.iop.org/1347-4065/22/L656>

59. Catalano A, Bhushan M. Evidence of  $p/n$  homojunction formation in  $\text{Zn}_3\text{P}_2$ . Appl Phys Lett [Internet]. 1980 Sep 15 [cited 2017 Oct 4];37(6):567–9. Available from: <http://aip.scitation.org/doi/10.1063/1.91786>
60. Bhushan M. Mg diffused zinc phosphide  $n/p$  junctions. J Appl Phys [Internet]. 1982 Jan 13 [cited 2017 Oct 4];53(1):514–9. Available from: <http://aip.scitation.org/doi/10.1063/1.329956>
61. The growth of large  $\text{Zn}_3\text{P}_2$  crystals by vapor transport. J Cryst Growth [Internet]. 1980 Aug 1 [cited 2017 Oct 4];49(4):681–6. Available from: <http://www.sciencedirect.com/science/article/pii/0022024880902948>
62. Single crystal growth of  $\text{Zn}_3\text{P}_2$ . J Cryst Growth [Internet]. 1981 Nov 1 [cited 2017 Oct 4];55(2):268–72. Available from: <http://www.sciencedirect.com/science/article/pii/0022024881900245>
63. Zinc phosphide thin films grown by RF sputtering. J Cryst Growth [Internet]. 1988 Jan 1 [cited 2017 Oct 4];86(1–4):423–9. Available from: <http://www.sciencedirect.com/science/article/pii/0022024890907549?via%3Dihub>
64.  $\text{Zn}_3\text{P}_2$  epitaxial growth by MOCVD. J Cryst Growth [Internet]. 1991 Dec 2 [cited 2017 Oct 4];115(1–4):793–7. Available from: <http://www.sciencedirect.com/science/article/pii/002202489190847X>
65. Suda T, Kakishita K, Sato H, Sasaki K. N-type zinc phosphide grown by molecular beam epitaxy. Appl Phys Lett [Internet]. 1996 Jun 4 [cited 2017 Oct 4]; Available from: <http://aip.scitation.org/doi/10.1063/1.117659>
66. Suda T, Kakishita K. Epitaxial growth of zinc phosphide. J Appl Phys [Internet]. 1992 Mar 15 [cited 2017 Oct 4];71(6):3039–41. Available from: <http://aip.scitation.org/doi/10.1063/1.350989>
67. Zinc phosphide thin films grown by plasma assisted vapor phase deposition. J Cryst Growth [Internet]. 1990 Jan 1 [cited 2017 Oct 4];99(1–4):625–9. Available from: <http://www.sciencedirect.com/science/article/pii/002202489090596D?via%3Dihub>
68.  $\text{Zn}_3\text{P}_2$ —a new material for optoelectronic devices. Microelectronics J [Internet]. 1994 Aug 1 [cited 2017 Oct 4];25(5):xxiii–xxviii. Available from: <http://www.sciencedirect.com/science/article/pii/0026269294900787#>
69. Kimball GM, Lewis NS, Atwater HA. Mg doping and alloying in  $\text{Zn}_3\text{P}_2$  heterojunction solar cells. In: 2010 35th IEEE Photovoltaic Specialists Conference [Internet]. IEEE; 2010 [cited 2017 Oct 4]. p. 001039–43. Available from: <http://ieeexplore.ieee.org/document/5614641/>
70. Bosco JP, Scanlon DO, Watson GW, Lewis NS, Atwater HA. Energy-band alignment of II-VI/ $\text{Zn}_3\text{P}_2$  heterojunctions from x-ray photoemission spectroscopy. J Appl Phys [Internet]. 2013 May 28 [cited 2017 Oct 4];113(20):203705. Available from: <http://aip.scitation.org/doi/10.1063/1.4807646>
71. Jeon S, Bosco JP, Wilson SS, Rozeveld SJ, Kim H, Atwater HA. Growth Mechanism and Electronic Structure of  $\text{Zn}_3\text{P}_2$  on the Ga-Rich GaAs(001) Surface. J Phys Chem C [Internet]. 2014 Jun 19 [cited 2017 Oct 4];118(24):12717–26. Available from: <http://pubs.acs.org/doi/abs/10.1021/jp4127804>
72. Vazquez-Mena O, Bosco JP, Ergen O, Rasool HI, Fathalizadeh A, Tosun M, et al. Performance Enhancement of a Graphene-Zinc Phosphide Solar Cell Using the Electric Field-Effect. Nano Lett [Internet]. 2014 Aug 13 [cited 2017 Oct 4];14(8):4280–5. Available from: <http://pubs.acs.org/doi/abs/10.1021/nl500925n>

73. Kimball GM, Lewis NS, Atwater HA. Synthesis and surface chemistry of Zn<sub>3</sub>P<sub>2</sub>. In: 2008 33rd IEEE Photovoltaic Specialists Conference [Internet]. IEEE; 2008 [cited 2017 Oct 4]. p. 1–6. Available from: <http://ieeexplore.ieee.org/document/4922747/>
74. Ginting M, Leslie JD. Preparation and electrical properties of heterojunctions of ZnO on Zn<sub>3</sub>P<sub>2</sub> and CdTe. Can J Phys [Internet]. 1989 Apr [cited 2017 Oct 4];67(4):448–55. Available from: <http://www.nrcresearchpress.com/doi/abs/10.1139/p89-080>
75. Brockway L, Van Laer M, Kang Y, Vaddiraju S. Large-scale synthesis and in situ functionalization of Zn<sub>3</sub>P<sub>2</sub> and Zn<sub>4</sub>Sb<sub>3</sub> nanowire powders. Phys Chem Chem Phys [Internet]. 2013 May 7 [cited 2021 Jan 11];15(17):6260–7. Available from: [www.rsc.org/pccp](http://www.rsc.org/pccp)
76. Stepanchikov, Chuiko. Excitons into one-axis crystals of zinc phosphide (Zn<sub>3</sub>P<sub>2</sub>). Condens Matter Phys [Internet]. 2009 [cited 2017 Oct 4];12(2):239–48. Available from: <http://www.icmp.lviv.ua/journal/zbirnyk.58/010/abstract.html>
77. Wang FC, Fahrenbruch AL, Bube RH. Transport mechanisms for Mg/Zn<sub>3</sub>P<sub>2</sub> junctions. J Appl Phys [Internet]. 1982 Dec 4 [cited 2021 Jan 12];53(12):8874–9. Available from: <http://aip.scitation.org/doi/10.1063/1.330402>
78. Long JA. Growth of Zn<sub>3</sub>P<sub>2</sub> by metalorganic chemical vapor deposition. In: Proceedings - The Electrochemical Society [Internet]. Electrochemical Soc; 1982 [cited 2021 Jan 12]. p. 405–10. Available from: <https://ui.adsabs.harvard.edu/abs/1983JELS..130..725L/abstract>
79. Sierański K, Szatkowski J, Misiewicz J. Semiempirical tight-binding band structure of II<sub>3</sub>V<sub>2</sub> semiconductors: Cd<sub>3</sub>P<sub>2</sub>, Zn<sub>3</sub>P<sub>2</sub>, Cd<sub>3</sub>As<sub>2</sub>, and Zn<sub>3</sub>As<sub>2</sub>. Phys Rev B [Internet]. 1994 Sep 15 [cited 2020 Jul 27];50(11):7331–7. Available from: <https://journals.aps.org/prb/abstract/10.1103/PhysRevB.50.7331>
80. Loureno SA, Dias IFL, Duarte JL, Laureto E, Poças LC, Toginho Filho DO, et al. Thermal expansion contribution to the temperature dependence of excitonic transitions in GaAs and AlGaAs. Brazilian J Phys [Internet]. 2004 Jun [cited 2017 Oct 4];34(2a):517–25. Available from: [http://www.scielo.br/scielo.php?script=sci\\_arttext&pid=S0103-97332004000300031&lng=en&nrm=iso&tlng=en](http://www.scielo.br/scielo.php?script=sci_arttext&pid=S0103-97332004000300031&lng=en&nrm=iso&tlng=en)
81. Middelmann T, Walkov A, Bartl G, Schödel R. Thermal expansion coefficient of single-crystal silicon from 7 K to 293 K. Phys Rev B [Internet]. 2015 Nov 19 [cited 2017 Oct 4];92(17):174113. Available from: <https://link.aps.org/doi/10.1103/PhysRevB.92.174113>
82. Demers S, van de Walle A. Intrinsic defects and dopability of zinc phosphide. Phys Rev B [Internet]. 2012 May 22 [cited 2017 Oct 4];85(19):195208. Available from: <https://link.aps.org/doi/10.1103/PhysRevB.85.195208>
83. PhD thesis by Jeffrey Paul Bosco, under supervision of Prof. Harry Atwater CI of T. Rational design of zinc phosphide heterojunction photovoltaics [Internet]. 2014. Available from: [chrome-extension://oemmnecbldboiebfnladdacbfmadadm/http://citeseerx.ist.psu.edu/viewdoc/download?doi=10.1.1.422.9618&rep=rep1&type=pdf](http://citeseerx.ist.psu.edu/viewdoc/download?doi=10.1.1.422.9618&rep=rep1&type=pdf)
84. Laks DB, Van de Walle CG. Self-Compensation and Doping Problems in ZnSe. MRS Proc [Internet]. 1992 [cited 2021 Jan 12];242. Available from: <https://www.cambridge.org/core/journals/mrs-online-proceedings-library-archive/article/abs/selfcompensation-and-doping-problems-in-znse/5FCFD00A7A9BDA92548E92EAD2682979>
85. Bhushan M. Mg diffused zinc phosphide *n* / *p* junctions. J Appl Phys [Internet]. 1982 Jan 13 [cited 2017 Oct 12];53(1):514–9. Available from: <http://aip.scitation.org/doi/10.1063/1.329956>

86. Catalano A, Bhushan M. Evidence of  $p/n$  homojunction formation in  $\text{Zn}_3\text{P}_2$ . Appl Phys Lett [Internet]. 1980 Sep 15 [cited 2017 Oct 12];37(6):567–9. Available from: <http://aip.scitation.org/doi/10.1063/1.91786>
87. Drobyshev E, Kybarskaya L, Dagaev S, Solovyev N. New insight in beryllium toxicity excluding exposure to beryllium-containing dust: Accumulation patterns, target organs, and elimination. Arch Toxicol [Internet]. 2019 [cited 2021 Jan 12];93(4):859–69. Available from: <https://pubmed.ncbi.nlm.nih.gov/30891623/>
88. Pawlikowski JM. Band structure and properties of  $\text{Zn}_3\text{P}_2$ - promising new infrared material\*. Infrared Phys. 1981 May 1;21(3):181–7.
89. Briones F, Wang FC, Bube RH. Pair transitions in  $\text{Zn}_3\text{P}_2$ . Appl Phys Lett. 1981 Nov 15;39(10):805–7.
90. Robert S, Steinvall E. Growth and characterisation of earth-abundant semiconductor nanostructures for solar energy harvesting [Internet]. EPFL; 2020 [cited 2021 Jan 6]. Available from: <http://infoscience.epfl.ch/record/282133>
91. Dzade NY. First-Principles Insights into the Interface Chemistry between 4-Aminothiophenol and Zinc Phosphide ( $\text{Zn}_3\text{P}_2$ ) Nanoparticles. ACS Omega [Internet]. 2020 Jan 21 [cited 2021 Jan 6];5(2):1025–32. Available from: <https://pubs.acs.org/sharingguidelines>
92. Mirowska N, Misiewicz J. Defect-related transitions in  $\text{Zn}_3\text{P}_2$  studied by means of photovoltaic effect spectroscopy. Semicond Sci Technol [Internet]. 1992 Nov 1 [cited 2021 Jan 11];7(11):1332–6. Available from: <https://iopscience.iop.org/article/10.1088/0268-1242/7/11/007>
93. Stutz EZ, Escobar Steinvall S, Litvinchuk AP, Leran J-B, Zamani M, Paul R, et al. Raman spectroscopy and lattice dynamics calculations of tetragonally-structured single crystal zinc phosphide ( $\text{Zn}_3\text{P}_2$ ) nanowires. Nanotechnology [Internet]. 2021 Feb 19 [cited 2020 Dec 7];32(8):085704. Available from: <https://iopscience.iop.org/article/10.1088/1361-6528/abc91b>
94. Nayak A, Rao DR. Photoluminescence spectra of  $\text{Zn}_3\text{P}_2$ -Cd  $3\text{P}_2$  thin films. Appl Phys Lett [Internet]. 1993 Aug 2 [cited 2020 Dec 3];63(5):592–3. Available from: <http://aip.scitation.org/doi/10.1063/1.110779>
95. Escobar Steinvall S, Tappy N, Ghasemi M, Zamani RR, Lagrange T, Stutz EZ, et al. Multiple morphologies and functionality of nanowires made from earth-abundant zinc phosphide. Nanoscale Horizons. 2020 Feb 1;5(2):274–82.
96. Pawlikowski JM.  $\text{Zn}_3\text{P}_2$  as infrared-to-ultraviolet photoconverter. Infrared Phys. 1988 May 1;28(3):177–82.
97. Rao VJ, Salvi M V., Samuel V, Sinha APB. Structural and optical properties of  $\text{Zn}_3\text{P}_2$  thin films. J Mater Sci [Internet]. 1985 Sep 1 [cited 2021 Jan 12];20(9):3277–82. Available from: <https://link.springer.com/article/10.1007/BF00545195>
98. Munoz V, Decroix D, Chevy A, Besson JM. Optical properties of zinc phosphide. J Appl Phys [Internet]. 1986 Nov 4 [cited 2021 Jan 12];60(9):3282–8. Available from: <http://aip.scitation.org/doi/10.1063/1.337719>
99. Schubert F. Room temperature properties of Si, Ge, and GaAs.
100. Kayes BM, Nie H, Twist R, Spruytte SG, Reinhardt F, Kizilyalli IC, et al. 27.6% Conversion efficiency, a new record for single-junction solar cells under 1 sun illumination. In: Conference Record of the IEEE Photovoltaic Specialists Conference. 2011. p. 000004–8.

101. Giudicelli E, Martaj N, Bennacer R, Dollet A, Perona A, Pincemin S, et al. Solar cells based on GaAs: Thermal behavior study. In: 11th International Conference on Concentrator Photovoltaic Systems [Internet]. 2015 [cited 2021 Jan 13]. p. 20002. Available from: <https://doi.org/10.1063/1.4931502>
102. Kim IH. Effects of emitter structure variation on the RF characteristics of AlGaAs/GaAs HBTs. *Mater Lett*. 2001 Jun 1;49(3–4):219–23.
103. Marko -Igor P, Sweeney SJ, Ustinov VM, Zhukov AE. GaAs-based long-wavelength lasers. *Semicond Sci Technol*. 2000;15.
104. Escobar Steinvall S, Ghisalberti L, Zamani RR, Tappy N, Hage FS, Stutz EZ, et al. Heterotwin Zn 3 P 2 superlattice nanowires: the role of indium insertion in the superlattice formation mechanism and their optical properties. *Nanoscale*. 2020 Nov 20;12(44):22534.
105. Not just for outer space: NREL has a path to cheaper GaAs solar cells – pv magazine USA [Internet]. [cited 2021 Jan 13]. Available from: <https://pv-magazine-usa.com/2020/01/13/solar-cells-from-space-are-on-the-way/>
106. Nothing can bring down the price of III-V solar cells – just add germanium – pv magazine International [Internet]. [cited 2021 Jan 13]. Available from: <https://www.pv-magazine.com/2019/06/10/nothing-can-bring-down-the-price-of-iii-v-solar-cells-just-add-germanium/>
107. Horowitz KAW, Remo T, Smith B, Ptak A. A Techno-Economic Analysis and Cost Reduction Roadmap for III-V Solar Cells [Internet]. 1960 [cited 2021 Jan 13]. Available from: <https://www.nrel.gov/docs/fy19osti/72103.pdf>.
108. Akiyama M, Kawarada Y, Ueda T, Nishi S, Kaminishi K. Growth of high quality GaAs layers on Si substrates by MOCVD. *J Cryst Growth*. 1986 Sep 1;77(1–3):490–7.
109. Krogstrup P, Jørgensen HI, Heiss M, Demichel O, Holm J V., Aagesen M, et al. Single-nanowire solar cells beyond the Shockley-Queisser limit. *Nat Photonics* [Internet]. 2013 Apr 24 [cited 2021 Jan 13];7(4):306–10. Available from: [www.nature.com/naturephotonics](http://www.nature.com/naturephotonics)
110. Podolskiy VA, Sarychev AK, Narimanov EE, Shalaev VM. Resonant light interaction with plasmonic nanowire systems. *J Opt A Pure Appl Opt* [Internet]. 2005 Feb 20 [cited 2021 Jan 13];7(2):S32. Available from: <https://iopscience.iop.org/article/10.1088/1464-4258/7/2/004>
111. Seo K, Wober M, Steinvurzel P, Schonbrun E, Dan Y, Ellenbogen T, et al. Multicolored vertical silicon nanowires. *Nano Lett* [Internet]. 2011 Apr 13 [cited 2021 Feb 8];11(4):1851–6. Available from: <https://pubs.acs.org/sharingguidelines>
112. Biermanns A, Breuer S, Trampert A, Davydok A, Geelhaar L, Pietsch U. Strain accommodation in Ga-assisted GaAs nanowires grown on silicon (111). *Nanotechnology* [Internet]. 2012 Aug 3;23(30):305703. Available from: <https://iopscience.iop.org/article/10.1088/0957-4484/23/30/305703>
113. Björk MT, Ohlsson BJ, Sass T, Persson AI, Thelander C, Magnusson MH, et al. One-dimensional heterostructures in semiconductor nanowhiskers. *Appl Phys Lett* [Internet]. 2002 Feb 11 [cited 2021 Jan 13];80(6):1058–60. Available from: <http://aip.scitation.org/doi/10.1063/1.1447312>
114. Gibson SJ, Boulanger JP, Lapierre RR. Opportunities and pitfalls in patterned self-catalyzed GaAs nanowire growth on silicon. *Semicond Sci Technol* [Internet]. 2013 Oct 10 [cited 2021 Jan 13];28(10):105025. Available from: <https://iopscience.iop.org/article/10.1088/0268-1242/28/10/105025>



115. Cirlin GE, Dubrovskii VG, Soshnikov IP, Sibirev N V., Samsonenko YB, Bouravleuv AD, et al. Critical diameters and temperature domains for MBE growth of III-V nanowires on lattice mismatched substrates. *Phys Status Solidi - Rapid Res Lett* [Internet]. 2009 May 1 [cited 2021 Jan 13];3(4):112–4. Available from: <https://onlinelibrary.wiley.com/doi/full/10.1002/pssr.200903057>
116. Glas F, Harmand JC, Patriarche G. Why does wurtzite form in nanowires of III-V zinc blende semiconductors? *Phys Rev Lett*. 2007 Oct 5;99(14).
117. Zamani M, Tütüncüoğlu G, Martí-Sánchez S, Francaviglia L, Güniat L, Ghisalberti L, et al. Optimizing the yield of A-polar GaAs nanowires to achieve defect-free zinc blende structure and enhanced optical functionality. *Nanoscale*. 2018 Sep 28;10(36):17080–91.
118. Arbiol J, Fontcuberta i Morral A, Estradé S, Peiró F, Kalache B, Roca i Cabarrocas P, et al. Influence of the (111) twinning on the formation of diamond cubic/diamond hexagonal heterostructures in Cu-catalyzed Si nanowires. *J Appl Phys* [Internet]. 2008 Sep 15 [cited 2018 Jan 29];104(6):064312. Available from: <http://aip.scitation.org/doi/10.1063/1.2976338>
119. Spirkoska D, Arbiol J, Gustafsson A, Conesa-Boj S, Glas F, Zardo I, et al. Structural and optical properties of high quality zinc-blende/wurtzite GaAs nanowire heterostructures. *Phys Rev B* [Internet]. 2009 Dec 31 [cited 2018 Jan 4];80(24):245325. Available from: <https://link.aps.org/doi/10.1103/PhysRevB.80.245325>
120. Zamani RR, Ghalamestani SG, Niu J, Sköld N, Dick KA, Zamani RR, et al. Control of Polarity, Structure and Growth Direction in Sn-Seeded GaSb Nanowires. In: *European Microscopy Congress 2016: Proceedings* [Internet]. Weinheim, Germany: Wiley-VCH Verlag GmbH & Co. KGaA; 2016 [cited 2017 Jul 7]. p. 662–3. Available from: <http://doi.wiley.com/10.1002/9783527808465.EMC2016.6741>
121. Kuech TF. III-V compound semiconductors: Growth and structures. Vol. 62, *Progress in Crystal Growth and Characterization of Materials*. Elsevier Ltd; 2016. p. 352–70.
122. Jacobsson D. *Crystal Structures in GaAs Nanowires Growth and Characterization*.
123. Bernal S, Botana FJ, Calvino JJ, López-Cartes C, Pérez-Omil JA, Rodríguez-Izquierdo JM. The interpretation of HREM images of supported metal catalysts using image simulation: Profile view images. *Ultramicroscopy*. 1998 May 1;72(3–4):135–64.
124. De La Mata M, Magen C, Gazquez J, Utama MIB, Heiss M, Lopatin S, et al. Polarity assignment in ZnTe, GaAs, ZnO, and GaN-AlN nanowires from direct dumbbell analysis. *Nano Lett*. 2012 May 9;12(5):2579–86.
125. Utama MIB, de la Mata M, Magen C, Arbiol J, Xiong Q. Twinning-, Polytypism-, and Polarity-Induced Morphological Modulation in Nonplanar Nanostructures with van der Waals Epitaxy. *Adv Funct Mater* [Internet]. 2013 Apr 5 [cited 2018 Jan 29];23(13):1636–46. Available from: <http://doi.wiley.com/10.1002/adfm.201202027>
126. Yuan X, Caroff P, Wong-Leung J, Fu L, Tan HH, Jagadish C. Tunable Polarity in a III-V Nanowire by Droplet Wetting and Surface Energy Engineering. *Adv Mater* [Internet]. 2015 Oct [cited 2019 Nov 20];27(40):6096–103. Available from: <http://doi.wiley.com/10.1002/adma.201503540>
127. Berding MA, Sher A, Chen A-B. Polarity in semiconductor compounds. *Phys Rev B* [Internet]. 1987 Nov 15 [cited 2018 Jan 16];36(14):7433–6. Available from: <https://link.aps.org/doi/10.1103/PhysRevB.36.7433>
128. Zamani RR, Gorji Ghalamestani S, Niu J, Sköld N, Dick KA. Polarity and growth directions in

- Sn-seeded GaSb nanowires. *Nanoscale*. 2017 Mar 7;9(9):3159–68.
129. Plissard S, Dick KA, Larrieu G, Godey S, Addad A, Wallart X, et al. Gold-free growth of GaAs nanowires on silicon: Arrays and polytypism. *Nanotechnology* [Internet]. 2010 Sep 24 [cited 2021 Jan 14];21(38):385602. Available from: <https://iopscience.iop.org/article/10.1088/0957-4484/21/38/385602>
  130. Potts H, Friedl M, Amaduzzi F, Tang K, Tütüncüoğlu G, Matteini F, et al. From Twinning to Pure Zincblende Catalyst-Free InAs(Sb) Nanowires. *Nano Lett* [Internet]. 2016 Jan 13 [cited 2019 Nov 28];16(1):637–43. Available from: <https://pubs.acs.org/doi/10.1021/acs.nanolett.5b04367>
  131. Zhou C, Zheng K, Chen PP, Matsumura S, Lu W, Zou J. Crystal-phase control of GaAs-GaAsSb core-shell/axial nanowire heterostructures by a two-step growth method. *J Mater Chem C* [Internet]. 2018 Jun 28 [cited 2021 Jan 14];6(25):6726–32. Available from: <https://pubs.rsc.org/en/content/articlehtml/2018/tc/c8tc01529e>
  132. Heiss M, Fontana Y, Gustafsson A, Wüst G, Magen C, O'Regan DD, et al. Self-assembled quantum dots in a nanowire system for quantum photonics. *Nat Mater* [Internet]. 2013 Feb 3 [cited 2021 Jan 14];12(5):439–44. Available from: [www.nature.com/naturematerials](http://www.nature.com/naturematerials)
  133. Mancini L, Fontana Y, Conesa-Boj S, Blum I, Vurpillot F, Francaviglia L, et al. Three-dimensional nanoscale study of Al segregation and quantum dot formation in GaAs/AlGaAs core-shell nanowires. *Appl Phys Lett* [Internet]. 2014 Dec 15 [cited 2021 Jan 14];105(24):243106. Available from: <http://aip.scitation.org/doi/10.1063/1.4904952>
  134. Francaviglia L, Fontana Y, Conesa-Boj S, Tütüncüoğlu G, Duchêne L, Tanasescu MB, et al. Quantum dots in the GaAs/AlGaAs core-shell nanowires: Statistical occurrence as a function of the shell thickness. *Appl Phys Lett* [Internet]. 2015 Jul 20 [cited 2017 Apr 18];107(3):033106. Available from: <http://aip.scitation.org/doi/10.1063/1.4927315>
  135. McIntyre PC, Fontcuberta i Morral A. Semiconductor nanowires: to grow or not to grow? Vol. 9, *Materials Today Nano*. Elsevier Ltd; 2020. p. 100058.
  136. Güniat L, Caroff P, Fontcuberta i Morral A. Vapor Phase Growth of Semiconductor Nanowires: Key Developments and Open Questions. Vol. 119, *Chemical Reviews*. American Chemical Society; 2019. p. 8958–71.
  137. Wagner RS, Ellis WC. Vapor-liquid-solid mechanism of single crystal growth. *Appl Phys Lett* [Internet]. 1964 Mar 23 [cited 2017 Jul 6];4(5):89–90. Available from: <http://aip.scitation.org/doi/10.1063/1.1753975>
  138. Colombo C, Spirkoska D, Frimmer M, Abstreiter G, Fontcuberta i Morral A. Ga-assisted catalyst-free growth mechanism of GaAs nanowires by molecular beam epitaxy. *Phys Rev B* [Internet]. 2008 Apr 28 [cited 2018 Jan 22];77(15):155326. Available from: <https://link.aps.org/doi/10.1103/PhysRevB.77.155326>
  139. Semiconductor contamination: Not your usual suspects - EDN [Internet]. [cited 2021 Jan 19]. Available from: <https://www.edn.com/semiconductor-contamination-not-your-usual-suspects/>
  140. Kim W, Dubrovskii VG, Vukajlovic-Plestina J, Tütüncüoğlu G, Francaviglia L, Güniat L, et al. Bistability of Contact Angle and Its Role in Achieving Quantum-Thin Self-Assisted GaAs nanowires. *Nano Lett*. 2018 Jan 10;18(1):49–57.
  141. Jacobsson D, Panciera F, Tersoff J, Reuter MC, Lehmann S, Hofmann S, et al. Interface dynamics and crystal phase switching in GaAs nanowires. *Nature*. 2016 Mar 16;531(7594):317–22.

142. Vukajlovic-Plestina J, Kim W, Ghisalberti L, Varnavides G, Tütüncüoglu G, Potts H, et al. Fundamental aspects to localize self-catalyzed III-V nanowires on silicon. *Nat Commun*. 2019 Dec 1;10(1).
143. Gandman M, Kauffmann Y, Kaplan WD. Quantification of ordering at a solid-liquid interface using plasmon electron energy loss spectroscopy. *Appl Phys Lett*. 2015 Feb 2;106(5).
144. Kaplan WD, Kauffmann Y. STRUCTURAL ORDER IN LIQUIDS INDUCED BY INTERFACES WITH CRYSTALS. *Annu Rev Mater Res* [Internet]. 2006 Aug 28 [cited 2017 Jul 7];36(1):1–48. Available from: <http://www.annualreviews.org/doi/10.1146/annurev.matsci.36.020105.104035>
145. Hashibon A, Adler J, Finnis MW, Kaplan WD. Atomistic study of structural correlations at a liquid–solid interface. *Comput Mater Sci* [Internet]. 2002 Jul 1 [cited 2018 Jul 10];24(4):443–52. Available from: <https://www.sciencedirect.com/science/article/pii/S0927025601002658>
146. Kaplan WD, Chatain D, Wynblatt P, Carter WC. A review of wetting versus adsorption, complexions, and related phenomena: the rosetta stone of wetting. *J Mater Sci* [Internet]. 2013 Sep 27 [cited 2019 Dec 17];48(17):5681–717. Available from: <http://link.springer.com/10.1007/s10853-013-7462-y>
147. Gandman M, Kauffmann Y, Koch CT, Kaplan WD. Direct Quantification of Ordering at a Solid-Liquid Interface Using Aberration Corrected Transmission Electron Microscopy. *Phys Rev Lett* [Internet]. 2013 Feb 20 [cited 2017 Jul 7];110(8):086106. Available from: <http://www.ncbi.nlm.nih.gov/pubmed/23473172>
148. Oh SH, Kauffmann Y, Scheu C, Kaplan WD, Rühle M. Ordered liquid aluminum at the interface with sapphire. *Science* [Internet]. 2005 Oct 28 [cited 2017 Oct 28];310(5748):661–3. Available from: <http://www.ncbi.nlm.nih.gov/pubmed/16210498>
149. Gandman M, Kauffmann Y, Kaplan WD. Quantification of ordering at a solid-liquid interface using plasmon electron energy loss spectroscopy. *Appl Phys Lett* [Internet]. 2015 Feb 2 [cited 2017 Jul 7];106(5):051603. Available from: <http://aip.scitation.org/doi/10.1063/1.4907617>
150. Oh SH, Chisholm MF, Kauffmann Y, Kaplan WD, Luo W, Rühle M, et al. Oscillatory mass transport in vapor-liquid-solid growth of sapphire nanowires. *Science* [Internet]. 2010 Oct 22 [cited 2018 May 19];330(6003):489–93. Available from: <http://www.ncbi.nlm.nih.gov/pubmed/20966248>
151. Abe E. Atomic-Scale Characterization of Nanostructured Metallic Materials by HAADF/Z-contrast STEM.
152. QCM [Internet]. [cited 2021 Feb 9]. Available from: <https://www.nottingham.ac.uk/isac/facilities/qcm.aspx>
153. Joyce BA. Materials fundamentals of molecular beam epitaxy. By Jeffrey Y. Tsao, Academic Press, London 1992, softcover, 301 pp., £ 49,94, ISBN 0-12-701625-2. *Adv Mater* [Internet]. 1993 Oct 1 [cited 2021 Feb 9];5(10):773–773. Available from: <http://doi.wiley.com/10.1002/adma.19930051028>
154. RHEED: Reflection High Energy Electron Diffraction | SPECS [Internet]. [cited 2021 Feb 9]. Available from: <https://www.specs-group.com/nc/specsgroup/knowledge/methods/detail/rheed/>
155. Hasegawa S. Reflection High Energy Electron Diffraction. In 2012. p. 307–18.
156. Federation of American Scientists :: White Phosphorus Fact Sheet [Internet]. [cited 2021 Feb 10]. Available from: <https://fas.org/programs/bio/factsheets/whitephosphorus.html>

157. The Jus in Bello of White Phosphorus: Getting the Law Correct - Lawfare [Internet]. [cited 2021 Feb 10]. Available from: <https://www.lawfareblog.com/jus-bello-white-phosphorus-getting-law-correct>
158. ATSDR - Medical Management Guidelines (MMGs): Phosphine [Internet]. [cited 2021 Feb 10]. Available from: <https://www.atsdr.cdc.gov/mmg/mmg.asp?id=1013&tid=214>
159. Urone PP, Hinrichs R. Limits of Resolution: The Rayleigh Criterion. OpenStax; 2012.
160. Rose H, Wan W, Berkeley L. ABERRATION CORRECTION IN ELECTRON MICROSCOPY\*.
161. Egerton RF. Electron Energy-Loss Spectroscopy in the Electron Microscope. Electron Energy-Loss Spectroscopy in the Electron Microscope. Springer US; 2011.
162. Leakage x rays from electron microscopes [Internet]. [cited 2021 Feb 11]. Available from: <https://hps.org/publicinformation/ate/q12299.html>
163. Tanaka N, Tanaka N. Structure and Imaging of a Transmission Electron Microscope (TEM). In: Electron Nano-Imaging [Internet]. Springer Japan; 2017 [cited 2021 Feb 11]. p. 17–28. Available from: [https://link.springer.com/chapter/10.1007/978-4-431-56502-4\\_2](https://link.springer.com/chapter/10.1007/978-4-431-56502-4_2)
164. Scanning Electron Microscopy (SEM) [Internet]. [cited 2021 Feb 11]. Available from: [https://serc.carleton.edu/research\\_education/geochemsheets/techniques/SEM.html](https://serc.carleton.edu/research_education/geochemsheets/techniques/SEM.html)
165. Egerton RF. Physical principles of electron microscopy: An introduction to TEM, SEM, and AEM, second edition. Physical Principles of Electron Microscopy: An Introduction to TEM, SEM, and AEM, Second Edition. Springer International Publishing; 2016. 1–196 p.
166. Anatomy of a Microscope - Optical Aberrations | Olympus LS [Internet]. [cited 2021 Feb 11]. Available from: <https://www.olympus-lifescience.com/en/microscope-resource/primer/anatomy/aberrations/>
167. Keywords “aperture” | Keywords | Glossary of TEM Terms | JEOL [Internet]. [cited 2021 Feb 17]. Available from: [https://www.jeol.co.jp/en/words/emterms/search\\_result.html?keyword=aperture](https://www.jeol.co.jp/en/words/emterms/search_result.html?keyword=aperture)
168. Imaging (an overview by GATAN) [Internet]. [cited 2021 Feb 11]. Available from: <https://www.gatan.com/techniques/imaging>
169. Hetherington C. Aberration correction for TEM. Mater Today. 2004 Dec 1;7(12):50–5.
170. Leary R, Brydson R. Chromatic aberration correction: The next step in electron microscopy. In: Advances in Imaging and Electron Physics. Academic Press Inc.; 2011. p. 73–130.
171. Aberration | optics | Britannica [Internet]. [cited 2021 Feb 25]. Available from: <https://www.britannica.com/technology/aberration#ref61610>
172. Hawkes PW. Aberration Correction Past and Present. Philos Trans Math Phys Eng Sci [Internet]. 2009 [cited 2021 Feb 25];367:3637–64. Available from: <https://www.jstor.org/stable/40485686>
173. Scherzer O. The theoretical resolution limit of the electron microscope. J Appl Phys [Internet]. 1949 Jan 28 [cited 2021 Feb 25];20(1):20–9. Available from: <http://aip.scitation.org/doi/10.1063/1.1698233>
174. Pennycook SJ, Varela M, Hetherington CJD, Kirkland AI. Materials advances through aberration-corrected electron microscopy. MRS Bull [Internet]. 2006 [cited 2021 Mar 14];31(1):36–42. Available from: <https://doi.org/10.1557/mrs2006.4>

175. Bachmatiuk A, Zhao J, Gorantla SM, Martinez IGG, Wiedermann J, Lee C, et al. Low voltage transmission electron microscopy of Graphene [Internet]. Vol. 11, Small. Wiley-VCH Verlag; 2015 [cited 2021 Feb 17]. p. 515–42. Available from: <https://pubmed.ncbi.nlm.nih.gov/25408379/>
176. Raman Spectroscopy | Instrumentation, Introduction & Principle [Internet]. [cited 2021 Feb 18]. Available from: [https://www.mt.com/ch/en/home/applications/L1\\_AutoChem\\_Applications/Raman-Spectroscopy.html](https://www.mt.com/ch/en/home/applications/L1_AutoChem_Applications/Raman-Spectroscopy.html)
177. Principles of Instrumental Analysis - Douglas A. Skoog, F. James Holler, Stanley R. Crouch - Google Books [Internet]. [cited 2021 Feb 18]. Available from: [https://books.google.ch/books?hl=en&lr=&id=D13EDQAAQBAJ&oi=fnd&pg=PP1&ots=DL DhEyOz8q&sig=tDoXC2rU7qQ113QEJdJKkIoJw3I&redir\\_esc=y#v=onepage&q&f=false](https://books.google.ch/books?hl=en&lr=&id=D13EDQAAQBAJ&oi=fnd&pg=PP1&ots=DL DhEyOz8q&sig=tDoXC2rU7qQ113QEJdJKkIoJw3I&redir_esc=y#v=onepage&q&f=false)
178. Bumbrah GS, Sharma RM. Raman spectroscopy – Basic principle, instrumentation and selected applications for the characterization of drugs of abuse [Internet]. Vol. 6, Egyptian Journal of Forensic Sciences. Egyptian Forensic Medicine Authority; 2016 [cited 2021 Feb 18]. p. 209–15. Available from: <http://dx.doi.org/10.1016/j.ejfs.2015.06.001>
179. The Nobel Prize in Physics 1930 - NobelPrize.org [Internet]. [cited 2021 Feb 18]. Available from: <https://www.nobelprize.org/prizes/physics/1930/summary/>
180. BraggsLaw [Internet]. [cited 2021 Feb 18]. Available from: [https://serc.carleton.edu/research\\_education/geochemsheets/BraggsLaw.html](https://serc.carleton.edu/research_education/geochemsheets/BraggsLaw.html)
181. Introduction to Crystallography and Data Acquisition: Basic XRD Course by PANanalytical [Internet]. [cited 2021 Feb 18]. Available from: <http://jiam.utk.edu/facilities/diffraction/Basic Principles of Data Acquisition.pdf>
182. Paul R, Humblot N, Humblot N, Steinvall SE, Stutz EZ, Joglekar SS, et al. Van der Waals Epitaxy of Earth-Abundant Zn<sub>3</sub>P<sub>2</sub> on Graphene for Photovoltaics. Cryst Growth Des [Internet]. 2020 Jun 3 [cited 2020 Aug 3];20(6):3816–25. Available from: <https://dx.doi.org/10.1021/acs.cgd.0c00125>
183. First Solar wins reprieve in EU toxic substance ban | Reuters [Internet]. [cited 2021 Feb 8]. Available from: <https://www.reuters.com/article/us-firstsolar-eu/first-solar-wins-reprive-in-eu-toxic-substance-ban-idUSTRE6AN5Q820101124>





# Curriculum Vitae

## Mahdi Zamani

### Doctoral Assistant

Highly Flexible, with a history of collaborative work, strong background in engineering, quantitative reasoning and data science/ machine learning

Email: [mahdi.zamani171@gmail.com](mailto:mahdi.zamani171@gmail.com)

Address: Chavannes-pres-Renens, Switzerland

Phone: 0041786862361

Date of Birth: 05-08-1990



### Professional Experiences:

11/2016- 05/2021

#### Doctoral Assistant in Materials Science and Engineering

Laboratory of Semiconductor Materials (LMSC),  
École polytechnique fédérale de Lausanne (EPFL), Lausanne, Switzerland

- Leading a multi-disciplinary collaboration between several teams working on cutting edge research in materials science
- Development and characterization of defect-free, high quality earth-abundant semiconductor thin films for scalable photovoltaics applications
- Defect elimination in semiconductor nanowires
- Lab assistance for Bachelor's studies
- Semester Project supervision for Bachelor's and Master's students

10/2015- 06/2016

#### Intern

Laboratory of Semiconductor Materials (LMSC)  
École polytechnique fédérale de Lausanne (EPFL), Lausanne, Switzerland

### Education:

11/2016- 05/2021

#### PhD in Materials Science and Engineering

Laboratory of Semiconductor Materials (LMSC),  
École polytechnique fédérale de Lausanne (EPFL), Lausanne, Switzerland

03/2014-09/2016

#### Masters of Science in Materials Engineering and Nanotechnology

The Polytechnic University of Milan, Milan, Italy  
GPA: 110 with honors / 110

09/2008-07/2013

#### Bachelor of Science in Mechanical Engineering

Amirkabir University of Technology, Tehran, Iran  
GPA: 79%

### Skills and Experiences:

- Crystal growth and epitaxy of thin films and nanowires
- Ultra high vacuum systems
- Electron microscopy (SEM, TEM), Focused Ion Beam (FIB)
- Characterization : Raman Spectroscopy, X-ray Diffraction (XRD)
- Cleanroom work
- Physics of semiconductors
- Programming languages: Python, R, MATLAB, Mathematica
- Data Science and Machine Learning
- Scientific plotting and demonstration
- Finite element analysis (ANSYS, Comsol)
- Other software: Microsoft Office, Adobe Illustrator, Origin

### Publications:

Here are a few examples of my publications :

- **Mahdi Zamani\***, Giulio Imbalzano\*, et al , "3D Ordering at the LiquidSolid Polar Interface of Nanowires", Advanced Materials- August 2020
- **Mahdi Zamani\***, Gözde Tütüncüoğlu, et al, "Optimizing the yield of A-polar GaAs nanowires to achieve defect-free zinc blende structure and enhanced optical functionality" Nanoscale, August 2018
- **Mahdi Zamani**, et al, "Free vibration analysis of moderately thick trapezoidal symmetrically laminated plates with various combinations of boundary conditions" European Journal of Mechanics-A/Solids, November 2012
- Equal contributions